Enhancing Materials for Fuel Cells and Organic Solar Cells through Molecular Design

By

Lionel C. H. Moh

B.S. Materials Science and Engineering
University of Illinois, Urbana-Champaign, 2010

Submitted to the Department of Materials Science and Engineering in Partial Fulfillment of the Requirements for the Degree of

Doctor of Philosophy in Materials Science and Engineering

AT THE

MASSACHUSETTS INSTITUTE OF TECHNOLOGY

June 2017

Signature of Author: _____
Department of Materials Science and Engineering
Date: 04 May 2017

Certified by: _____
Timothy M. Swager
John D. MacArthur Professor of Chemistry
Thesis Supervisor

Accepted by: _____
Donald Sadoway
John F. Elliott Professor of Materials Chemistry
Chair, Departmental Committee on Graduate Student

Enhancing Materials for Organic Solar Cells and Fuel Cells through Molecular Design

By

Lionel C. H. Moh

Submitted to the Department of Materials Science and Engineering on 04 May 2017 in Partial Fulfillment of the Requirements for the Degree of Doctor of Philosophy in Materials Science and Engineering

Abstract

In an effort to make alternative energy competitive to fossil fuels, research in improving efficiencies of solar cells and fuel cells have grown rapidly over the last few decades. One prominent strategy to improving the efficiencies in these devices focuses on engineering materials with customized molecular structure for enhancements in specific properties. Herein, new organic materials are designed and synthesized to enhance selected properties for applications in fuel cells and solar cells.

In chapter 1, triptycene poly(aryl ethers) are synthesized and characterized for enhancing ion conductivity of ion exchange membranes in fuel cells. Triptycene motif is incorporated to increase charge density and fractional free volume in the membranes. In Chapter 1.2, sulfonated triptycene poly(ether ether ketone) (S-tripPEEK) is synthesized and studied for proton exchange membranes (PEM). Increasing fractional free volume in the membrane results in high water uptake at relative humidity (RH) from 10 %RH to 90 %RH and higher proton mobility in the membranes. S-tripPEEK membranes show proton conductivities of 334 mS/cm at 85 °C at 90 %RH and 0.37 mS/cm at 85 °C at 20 %RH as compared to 18.9 mS/cm and 0.0014 mS/cm observed in commercially available Nafion117^{TM} membranes.

In Chapter 1.3, methylimidazolium triptycene poly(ether sulfone)s (MeIm-tripPES) are made for alkaline anion exchange membranes (AAEM) and are found to have ion conductivities of 104 mS/cm at 80 °C in water. Controlled nanophase separation with increased domain size contributed by the triptycene moiety lead to the high observed conductivities. However, the methylimidazolium functional groups on the membranes are not stable to alkaline conditions in the operation of a fuel cell.

In Chapter 2, dithiolodithiole (C_4S_4) heterocycle was synthesized and studied as a new building block for organic photovoltaic materials. As an electron-rich fused-ring motif, C_4S_4 is expected to be a more effective electron donor. Comparison with analogous thiophene derivatives shows that C_4S_4 moiety raises the highest occupied molecular orbital (HOMO) by 0.7 – 1.0 eV, suggesting a stronger electron donating character than thiophene. Furthermore, crystal structures of C_4S_4 molecules show planarity in the molecule which further reduces the bandgap.

Thesis Supervisor: Timothy M. Swager
Title: John D. MacArthur Professor of Chemistry

Dedicated to my dearest family

&

my beloved girlfriend, Mandy

Acknowledgements

I would like to take this opportunity to express my deepest gratitude to everyone who have supported me throughout my time as a graduate student.

First and foremost, I would like to thank my advisor Prof. Timothy Swager. Listening to his ideas and thought processes taught me how to explore science as an independent researcher and stay focused on understanding the fundamentals behind our observations. This widened my vision on projects and improved my analytical abilities as a scientist. Together with his constant support and encouragement, I was empowered with the courage to explore new areas under his guidance and successfully complete all the projects that I was part of.

Next, I would like to thank my committee members, Professor Michael Rubner and Professor Jeffrey Grossman, who have given me valuable experimental advice during our meetings and collaborations that allowed me to venture and learn more about research in other areas beyond my thesis.

I would also like to thank all my collaborators who have made this work possible: Agency for Science, Technology and Research in Singapore for all their funding support throughout my studies; Professor Derek Schipper who brought me into the world of chemistry when I started in the Swager lab and for all his contribution to our work in solar cell materials; Dr. John Goods for his contributions to our work in proton exchange membranes; Dr. Yoonseob Kim for his contributions to our work in alkaline anion exchange membranes; Sarah Park in the Dinca Lab and Seyed Mirvakili in the Hunter Lab for the specialized equipment that allowed me to complete my work; Staff at the Institute of Soldier Nanotechnology (ISN), especially Dr. Steven Kooi and William DiNatale for all their equipment support; and of course, my great group members especially Brian Pretti, Kathy Sweeney, Joseph Walish and my office mates at ISN for all their heartfelt support throughout my time at MIT.

Finally, I would like to give my deepest thanks to my family and my girlfriend, Mandy. They have always been the shining light that is cheering me on throughout this journey.

Contents

List of Figures

Figure 1.2-3. ^{1}H NMR of tripPEEK(1,0) and S-tripPEEK(1,0). S-tripPEEK was sulfonated with concentrated sulfuric acid at 65 °C for 1 hour, resulting in successful sulfonation of 2 out of the 3 phenyl rings on the triptycene group.

Figure 1.2-4. TGA of S-tripPEEKs and S-PEEK from 50 °C to 900 °C at a heating rate of 20 °C/min. TGAs are normalized such that 100% is weight percent after the mass loss associated to water.

Figure 1.2-5. Proton conductivity of membranes 85 °C over different levels of relative humidity.

Figure 1.2-6. (a) Proton conductivity in water and (b) hydration number of membranes in water. Hydration number is defined as the number of water molecules for every sulfonate group in the membrane.

Figure 1.2-7. DSC thermograms of hydrated S-tripPEEK films from -70 C to 25 C at a heating and cooling rate of 10 C/min. The loop observed in the cooling cycle of S-tripPEEK(1,0) is due to the supercooling of the water phase that resulted in rapid crystallization of ice that raised the temperature of the sample.

Figure 1.2-8. Plot of activation energy observed in each membrane from 20 %RH to 90 %RH.

Figure 1.3-1. (a) Degradation mechanisms of quaternary ammonium salts in AAEMs. (b) Stability of quaternary ammonium functional groups with respect to the base polymer structure.[64]

Figure 1.3-2. Functional groups that are found to be stable under alkaline conditions.

Figure 1.3-3. ^{1}H NMR model compound and model compound with one nitro group (400MHz, DMF-d7, RT). z* is the proton on the carbon beside nitro group.

Figure 1.3-4. ^{1}H NMR of the model compound with two nitro groups. Insert within the figure is the zoomed in of the peaks associated to the bridgehead protons.

Figure 1.3-5. Proton NMR of the model compound with 3 nitro groups. Insert within the figure is the zoomed in of the peaks associated to the bridgehead protons.

Figure 1.3-6. Overlay of NMR of nitrated tripPEEK and the NMR of the model compounds.

Figure 1.3-7. ATR-FTIR spectra of tripPEEK, NO2-tripPEEK and product after reduction.

Figure 1.3-8. Equivalent circuit model used to fit the Nyquist plots

Figure 1.3-9. DSC thermograms of (a) tripPES(1,0), (b) tripPES(1,1) and (c) tripPES(1,9). Heat flows are measured from 25 °C to 350 °C at a heating and cooling rate of 10 °C/min.

Figure 1.3-10. ^{1}H NMR of Cl-tripPES(1,0). Spectrum is taken at 400 MHz with $CDCl_3$ as solvent. TCE is tetrachloroethane that was used as the solvent in the chloromethylation step.

Figure 1.3-11. ^{1}H NMR of Cl-MeIm-trpPES(1,0) and Cl-tripPES(1,0). Spectrum is taken at 400 MHz with DMSO-d6 as solvent.

Figure 1.3-12. Thermogravimetric analysis of tripPES and functionalized tripPES. Samples were heated from 50 °C to 900 °C at a heating rate of 10 °C/min.

Figure 1.3-13. Alkaline anion conductivity of OH-MeIm-tripPES(1,1) membranes with 10 wt% binder. Degree of functionalization is defined as the percentage of the active phenyl rings on in the polymer that were functionalized. (Table 6) Straight line in this plots represents an Arrhenius behavior in conductivity and serve as a guide to show deviation caused due to swelling.

List of Schematics

List of Tables

Chapter 1. Functionalized Triptycene Poly(aryl ether)s for Ion Exchange Membranes in Fuel Cells

1.1. Introduction

Sir William Grove discovered the first fuel cell in 1839[1] and demonstrated the expansion into a fuel cell stack for more power in 1842.[2] Since the discovery, many different types of fuel cells were developed and can be generally group into the following types based on the material used as the separator: solid-oxide fuel cells (SOFCs) and molten-carbonate fuel cells (MCFCs) that operate above 500 °C, and proton exchange membrane fuel cells (PEMFCs) and anion exchange membrane fuel cells (AEMFCs) that operate below 200 °C.[3,4] Each of these fuel cells has its pros and cons mainly due to the operating temperatures. Compared to SOFCs and MCFCs, which operate at high temperatures, low temperature fuel cells like PEMFCs and AEMFCs are less efficient and less tolerant to impurities in the fuel but their low operating temperature allows for a faster start-up and better dimension stability which are crucial for portable fuel cells that are used for electric vehicles that starts and stops frequently.[4–6] Thus, in order to utilize fuel cells as a clean source of energy in transportation, efforts in improving the efficiencies of low temperature fuel cells such as PEMFCs and AEMFCs are crucial.

In the process of improving efficiencies of low temperature fuel cells, it is important to first understand the operation of fuel cells and the associated technological challenges. In PEMFCs, at the heart of a typical fuel cell is the membrane electrode assembly (MEA) comprising a proton exchange membrane (PEM) sandwiched between the anode and the cathode (Figure 1.1-1). During operation, fuel, such as hydrogen or alcohols, is supplied to the anode where the fuel is oxidized by an active catalyst to generate (i) electrons that go through the external circuit and into the cathode, and (ii) protons that goes through the proton exchange membrane to the cathode. At the cathode where air is supplied, oxygen in the air is reduced to form water and heat to complete the cycle.

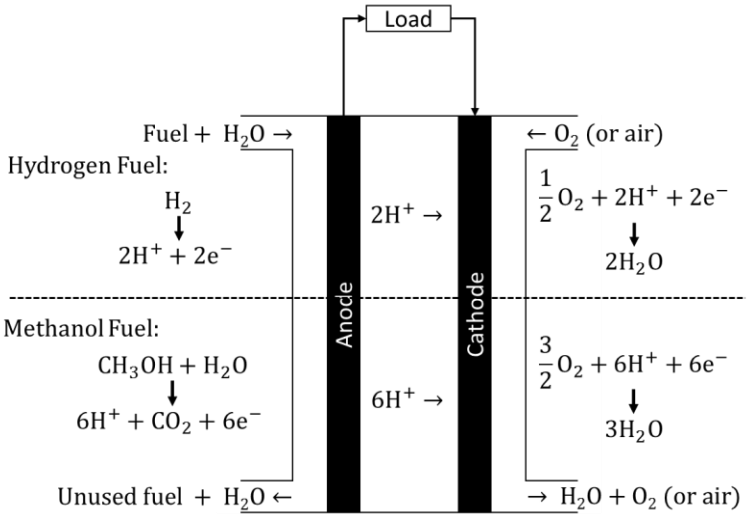

Figure 1.1-1. Schematic of a membrane electrode assembly in a PEMFC with the relevant half equations of all electrochemical reaction at the anode and the cathode

Similarly, in an AEMFC (Figure 1.1-2), the fuel is oxidized at the anode to produce electrons that go around the external circuit to the cathode to reduce oxygen in air. However, unlike PEMFCs where protons are generated at the anode, hydroxide ions are generated from the reduction of oxygen and transported to the anode in an AEMFC to complete the electrochemical cycle. The electrochemical reactions in AEMFCs are typically more efficient and can be catalyzed by inexpensive earth abundant metal catalysts.[3,4,7,8] These two benefits give AEMFCs an advantage over PEMFCs in terms of cost and efficiency.

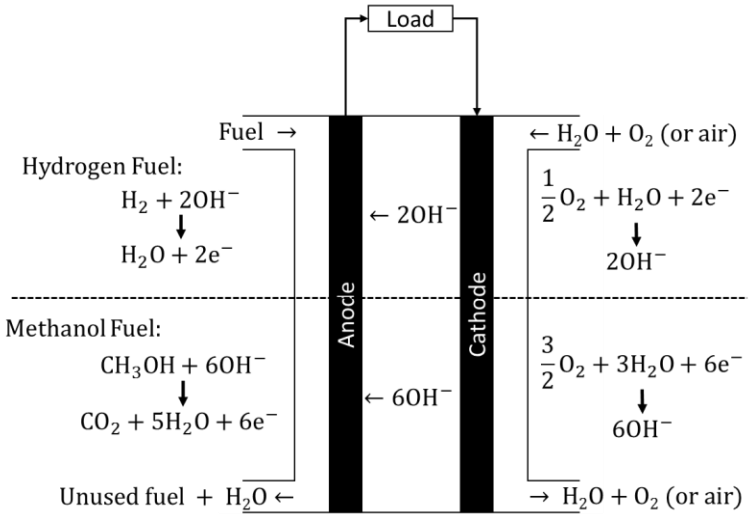

Figure 1.1-2. Schematic of a membrane electrode assembly in an AEMFC with the relevant half equations of all electrochemical reaction at the anode and the cathode.

The reactions shown by the electrochemical half equations at the anode in the AEMFC and the cathode at the PEMFC only occur at the interface where the reactant and ions from the membrane, meets the active catalyst in the electrode. Since the reactant and the catalyst can be loaded in excess, the limiting reagent in the fuel cell is ions that are transported through the membrane. Thus, in order to significantly improve the efficiency of the fuel cell, developing ion exchange membranes that has high ion conductivity of above 0.1 S/cm throughout the operation of the fuel cell will be crucial.[7,9]

In this project, the focus is on designing new ion exchange membranes for PEMFCs and AEMFCs. There are many approaches that have been reported in literature and they can generally be grouped into the following approaches: (i) new polymer designs, (ii) polymer composites with inorganic materials, and (iii) polymer membranes doped with small molecule carriers.[3,7,8,10–16] While mixing in inorganic materials or small molecule carriers can improve the conductivity of the membrane, further enhancements may be possible if they are applied to new base polymer designs that have intrinsic advantages. To advance fuel cell membranes, this thesis focuses on new polymer designs for ion exchange membranes for PEMFCs and

AEMFCs that are not composites with inorganic materials or doped with any other small molecule ion carriers, such as phosphoric acid[17,18] or ionic liquids.[19]

1.1.1. Factors Affecting Ion Conductivity

In order to improve the ion conductivity of membranes, it is important to understand the transport mechanisms for protons and hydroxide ions in the membranes. Ion exchange membranes are made up of ionic polymers that have charged functional groups, such as sulfonic acid in PEMs and quaternary ammonium in AEMs. Mobile ions dissociate from these functional groups and are transported within the membrane. The total charge that mobile ions carry through a given volume of the membrane per unit time is defined as the ion conductivity of the membrane.[20] Thus, conductivity can be improved in two ways: (i) increasing the number of ions within the membrane that can move and/or (ii) increasing the speed in which the ions can move.

The number of dissociated ions that move within the membrane is defined as the ion exchange capacity (IEC) of the membrane. IEC is the number of dissociated ions that is typically normalized to the mass of the membrane. This property can be directly controlled by designing the chemical structure to increase the number of charged functional groups per unit mass within the polymer. However, increasing the number of ionic groups also increases the hydrophilicity of the polymer and the solubility in methanol and water. This effect can lead to a loss in mechanical stability of the membrane which is detrimental for both PEMFCs and AEMFCs. Thus, balancing the increased IEC with structural integrity of the membrane remains a necessary challenge.

Improving the mobility of ions through the membrane requires an understanding of the transport mechanism. After dissociating from the stationary charge on the polymer, protons and hydroxide ions have profound interaction with water molecules around them due to the strong hydrogen bonds. At the rest state in water, protons exist as hydronium ions (H_3O^+) with their closest hydration shells containing three water

molecules through hydrogen bonding, forming the complex of $H_3O^+(H_2O)_3$.[21] On the other hand, hydroxide ions (OH^-) exist in the rest state with four water molecules, forming a complex of $OH^-(H_2O)_4$.[22] This hyper-coordination complex was found to be stable as a result of the delocalization of the three lone pairs in the oxygen atom.[22] Nonetheless, compared to other ions in water, both protons and hydroxide ions are known to have much faster ion conductivities[7,23] as the formation of these complexes creates an alternative path for ion transport through mass transfer between the ions and its first solvation shell.

For both protons and hydroxide ions, the higher conductivity is the result of the involvement of water as a medium of transport. It is generally accepted that the transport of protons and hydroxide ions in membranes are achieve through two different mechanisms, translational diffusion of the ions in a vehicular mechanism[24] and hopping between different host molecule through structural diffusion[21,22,25,26] (also known as the Grotthuss mechanism in proton conduction[25] which Grotthuss proposed in 1806 and his paper was translated into English in 2006[27]). The prevalence of one or the other depends on the water content in the membrane and the amount of free space within the membrane.[16,28]

In vehicular transport mechanism, the transport of ionic groups is based on a translational movement of the ions driven by the concentration and the electrostatic gradients in the membrane.[24,29] For example, in a PEMFC, the hydronium ions are generated at the anodic interfaces and consumed at the cathodic interfaces. This effect gives rise to the concentration and the electrostatic gradients within the membrane. In this mechanism, increasing free volume for diffusion of the whole vehicle will enhance ion transports.

In a structural diffusion mechanism, protons hop from one water molecule to another, resulting in the movement of ions to the water molecule in its first solvation shell. This process is different for protons as opposed to alkaline ions. For protons, the process is initiated by thermal fluctuations that break a hydrogen bond between water molecules in the first solvent shell (H_2O^a in Figure 1.1-3) and second

solvation shell (H_2O^b) of the hydronium ion.[21] With one less hydrogen bond, the water molecule in the first solvation shell pulls the proton from H_3O^+ closer, forming a $H_2O_5^+$ intermediate. The original H_3O^+ ion forms a new hydrogen bond with the initial water molecule (H_2O^b) that was disrupted, releasing the proton to the new water molecule.

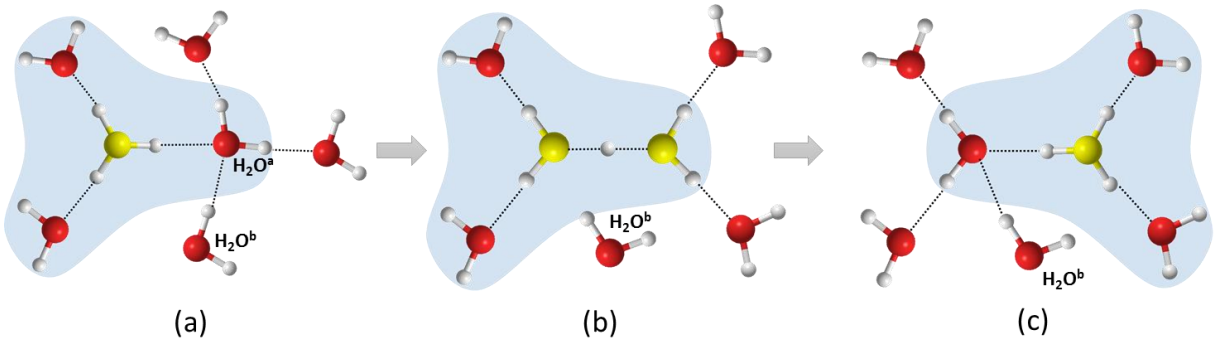

Figure 1.1-3. Schematic of the movement of a H_3O^+ ion through structural diffusion. Hydrogen is transferred from H_3O^+ to another water molecule after thermal fluctuations break a hydrogen bond in the second solvation shell. Blue area denotes the location of the first solvation shell of the proton.

For alkaline ions, the process is initiated by thermal fluctuations that break a hydrogen bond within the first solvation shell (Figure 1.1-4).[22,23] This main difference results in a stronger pull from the OH^- ion on another water molecule in the first solvation shell and another unbounded water molecule. A hydrogen is then transferred from the water molecule in the first solvation shell, resulting in the migration of the OH^- ion. In summary, for fast structural diffusion of protons and hydroxide ions, the membrane requires a continuous network of water molecules.

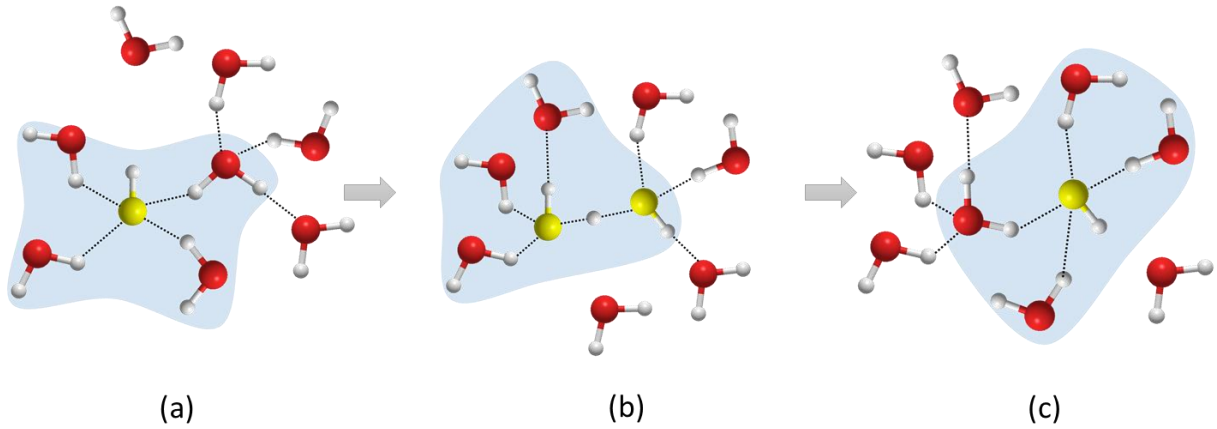

Figure 1.1-4. Schematic of the movement of a hydroxide ion through structural diffusion. Hydrogen is transferred from one water molecule to the hydroxide ion after thermal fluctuations break a hydrogen bond within the first solvation shell. Blue area denotes the location of the first solvation shell of the proton.

In summary, to facilitate transport of protons and hydroxides in both vehicular and structural diffusion mechanisms, it is important to retain water as a continuous network in the polymer membranes. Nafion™, the most widely used proton exchange membrane in industry, creates such network when swollen through controlled phase separation between the hydrophobic fluorous polymer structure and the hydroscopic sulfonic acid side group. However, due to the performance limitations in Nafion™ (chapter 1.2.1) and the lack of a similar analogue in anion exchange membranes, alternative polymer systems such as poly(aryl ether)s have been developed.

1.1.2. Poly(aryl ethers) as Base Polymers for Ion Exchange Membrane

The polymer designs in this thesis are based on improving the current functionalized poly(aryl ether)s (PAEs). PAEs are known to be a great substitute for the current membranes because of their synthetic simplicity, processability, and thermal and chemical stability under oxidative and reductive conditions within the operating temperatures (up to 200 °C) required for fuel cells.[7,11,30–32] PAEs are aromatic polymers with monomers that are linked with an ether group (Figure 1.1-5). They are generally synthesized through step growth polymerizations with nucleophilic aromatic substitution reactions, first used in polymerization in 1967.[33] In order for the polymerization to work well, one of the monomers needs

to have aromatic halides that are 'activated' by an electron withdrawing constituent, such as sulfone or ketone.

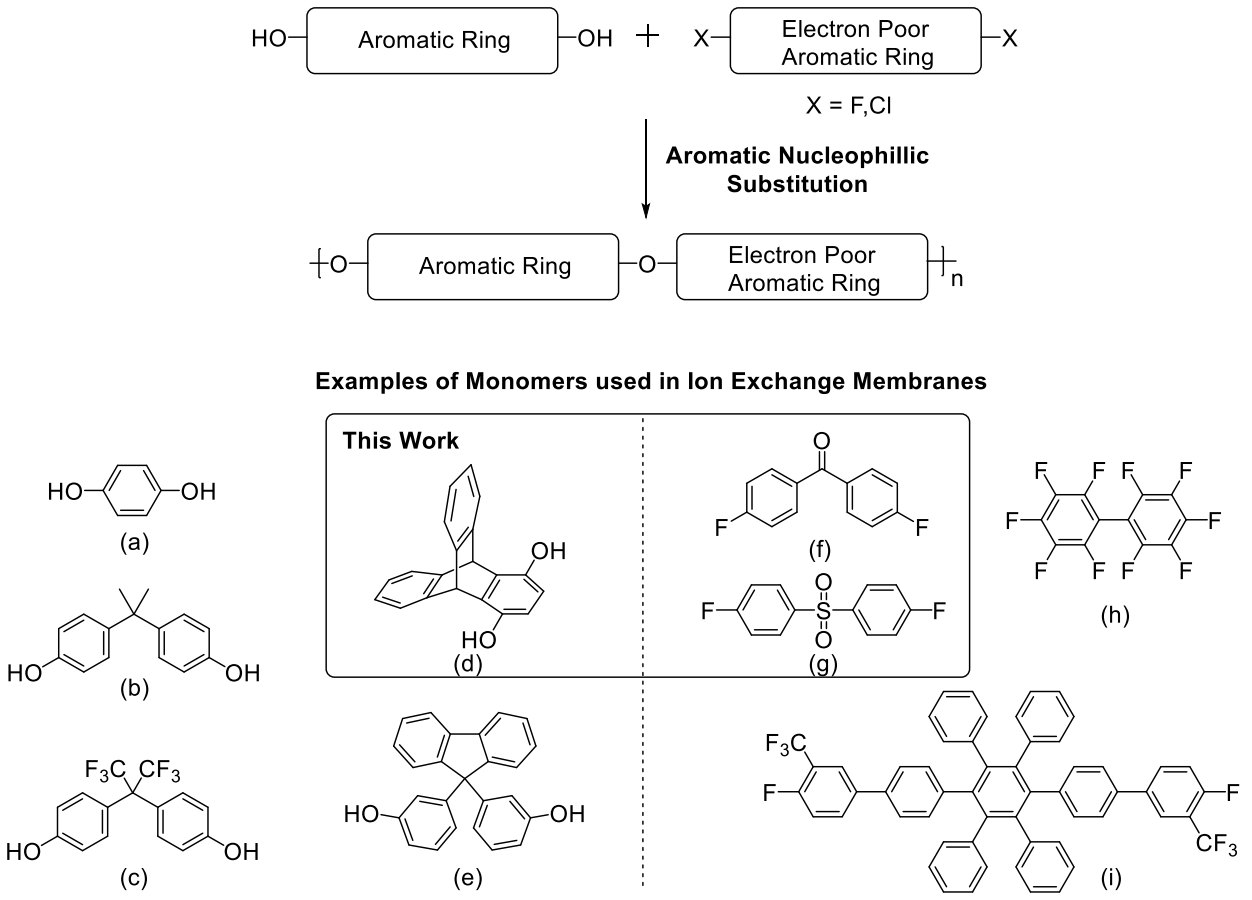

Figure 1.1-5. General chemical structures of poly(aryl ether)s with some examples of possible monomers that are used for ion exchange membranes

Many different variants and polymers of different compositions can be made by changing the composition of the monomers, allowing the possibility of fine-tuning the physical properties of the polymers. For example, the isopropyl group in bisphenol A (Figure 1.1-5b) imparts flexibility in the polymer backbone, which lowers the glass transition temperature and makes the resultant polymer more pliable. On the other hand, the sulfone group in bis(4-fluorophenyl)sulfone (Figure 1.1-5g) imparts rigidity in the polymer backbone, leading to the opposite effect and can make the resultant polymer more brittle.

Among the PAEs, poly(ether ether ketone) (PEEK) and poly(ether sulfone) (PES) are widely used as base polymers for ion exchange membranes as a result of synthetic simplicity possible for post polymerization functionalization and the ease of forming free standing membranes.[10,11,31,32] PEEK is made from hydroquinone (Figure 1.1-5a) and 4-4'-bifluorobenzophenone (Figure 1.1-5f), while PES is made from bisphenol A (Figure 1.1-5b) and bis(4-fluorophenyl)sulfone (Figure 1.1-5g). The electron rich aromatic rings with ether linkages one or both ends can be functionalized through electrophilic substitution reactions such as sulfonation and chloromethylation. To make proton exchange membranes, PEEK and PES can be treated with sulfonating agents, such as concentrated sulfuric acid. In this process, sulfur trioxide is the activated group that attacks the electron rich aromatic ring to produce a sulfonic acid functionalized polymer. On the other hand, anion exchange membranes require the synthesis of polycations which can be easily accessed through quaternization of chloromethyl functionalized PEEK or PES with amines or phosphines. Chloromethyl PES are typically synthesized with chloromethyl ethers in the presence of zinc (II) chloride.

Many strategies used to modify the base polymers to improve ion conductivities have been pursued and reviewed extensively over the years.[10–12,30,34] These strategies can be generally classified into two categories: improving mobile ion concentration or improving ion mobility. For example, adding fluorous groups in the monomers such as 4,4'-(Hexafluoroisopropylidene)diphenol (Figure 1.1-5c) or decafluorobiphenyl (Figure 1.1-5h) increases the hydrophobicity in the base polymer and improves the phase separation away from hydroscopic ionic groups in the membrane. This addition results in more defined water domains which improves the ion mobility. Another example is to introduce bulky groups with more sites for functionalization such as fluorene (Figure 1.1-5e) or hexaphenyl benzene (Figure 1.1-5i) into the polymer structure. More ionic groups can be introduced to the polymer to increase the ion concentration in the membrane while adding intrinsic free volume to improve water adsorption in the membrane.[35–37]

In this project, triptycene-based poly (ether ether ketone) and poly (ether sulfone) were developed to improve ion conductivities in PEMFCs and AEMFCs. The three dimensional non-compliant triptycene group,[38–40] increases the intrinsic free volume in the membranes and the phenyl rings associated with the triptycene structure provide multiple sites for post polymerization functionalization to yield ionic polymers for PEMFCs and AEMFCs. Studies of sulfonated triptycene PEEK for PEMFC and functionalized triptycene PES for AEMFCs will be covered in Chapter 1.2 and 1.3 respectively.

1.1.3. Methods to Probe and Understand Ion Conductivity in Membranes

To quantify the improvement of our synthetic designs, there is a need to probe the ion conductivity of the membrane and the associated properties such as the ion concentration and water content that affects ion conductivity in these membranes. In this section, we discussed the general methods that are used to probe the ion concentration, water content, and ion conductivity.

1.1.3.1. Ion Exchange Capacity through Titrations

Ion exchange capacity (IEC) of the membrane is defined to be the number of mobile ions per unit mass of the membrane which contributes to ion conductivity in the membrane as discussed in section 1.1.1. The method used to quantify IEC is the titration of the protons or hydroxide ions within the membrane. In proton exchange membranes, the membranes are soaked in a neutral salt solution such as sodium chloride solution, to exchange the protons with the sodium ions. The solution is then titrated with a dilute base of a known concentration. The amount of protons in the membrane can then be calculated and normalized by the mass of the membrane to obtain the IEC.

However, in anion exchange membranes, hydroxide ions can react with carbon dioxide in air to form carbonates. The release of the hydroxide ions in neutral solutions under normal atmosphere would result in the loss of hydroxide, leading to inaccuracy of the titration. Instead, these membranes are soaked in a known volume of a dilute acidic solution such as dilute hydrochloric acid with a known concentration,

releasing hydroxide ions from the membrane to neutralize the acid in the soaking solution. The resultant soaking solution was then back titrated with a dilute base of a known concentration to figure out the amount of protons that were neutralize, which is also the amount of hydroxide ions in the membrane. The value obtained was then normalized by the mass of the membrane to obtain the IEC.

1.1.3.2. Water Content in Membranes through Thermal Analysis

As the key medium of ion transport in membranes, the water content of the membrane needs to be characterized accurately. The membrane property that quantifies this water content is the hydration number (λ), which is defined as the number of water molecules per mobile ion in the membrane. To obtain λ, the amount of water in the membranes is first calculated by measuring the gain in mass of the membrane after equilibrating in the conditions at which ion conductivity is measured. The gain in mass would be the mass of water in the membrane, which can be used to determine the number of water molecules in the membrane which can then be normalized by the number of mobile ions in the membrane derived from the IEC.

1.1.3.3. Measuring Ion Conductivity with Electrochemical Impedance Spectroscopy

In order to experimentally determine the conductivity of ions in membranes, the method of choice is known as Electrochemical Impedance Spectroscopy (EIS).[41–43] Impedance is the effective resistance of the sample to an alternating current and it can be composed of resistive, capacitive, and inductive effects. Alternating voltages or currents at various frequencies are applied to the sample and the corresponding changes in amplitude and frequency of the recorded signal are used to determine the impedance in the sample. The data obtained are typically plotted as Nyquist plots, wherein the real (in phase) and imaginary (out of phase) components of the impedance are plotted against each other. The amplitude of the impedance is the distance between the data point and the origin and the change in frequency is described by the angle from the x axis (Figure 1.1-6a). By fitting the data obtained with the calculated equivalent circuit models (example in Figure 1.1-6b) of resistors, capacitors and inductors, the components and their values would provide insights into the sample.

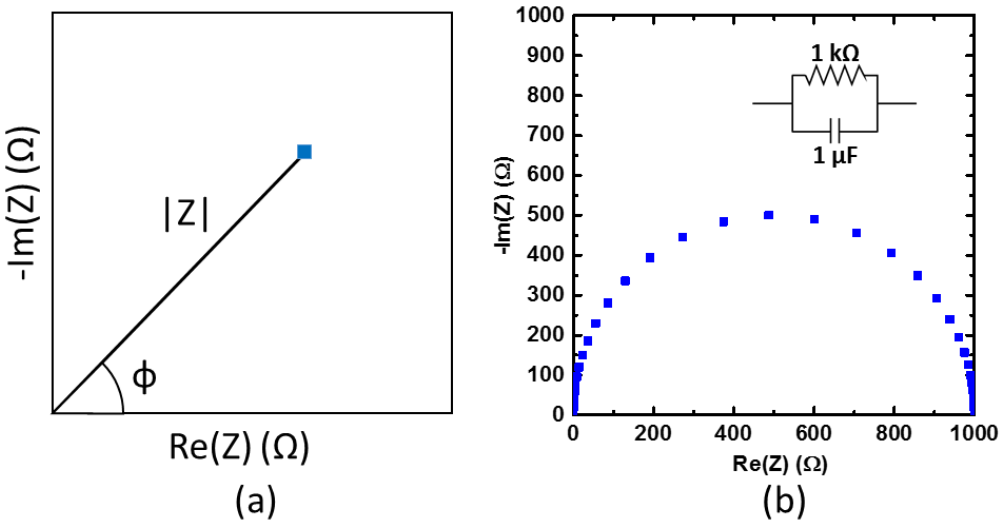

Figure 1.1-6. (a) Schematic of a single data point on a Nyquist plot. (b) Nyquist plot of a resistor and capacitor in parallel

When applied to an electrochemical interface at frequencies relevant to ion movements, EIS provides great insights into interfacial processes. For example, when used on an electrochemical interface between an electrode and electrolyte, kinetics of electrochemical reactions at the electrode can be determined through modeling the impedance spectrum obtained with an equivalent circuit (Figure 1.1-7). The components of the equivalent circuit are attributed to internal resistance of the electrode (R_{el}), capacitance of an electrical double layer at the electrode (C_d), and resistance of charge transfer from electrode to electrolyte (R_{ct}). However, it is important to note that EIS is a modelling technique and known physical phenomena need to be used to justify the circuit elements that are employed. In this example, the physical phenomenon can be captured through visualization of the path of the mobile charge. The charge first passes through the electrode wherein it encounters the internal resistance of the electrode. At the interface, the charge can either be part of the electrode that induces an electrical double layer or be transferred to an electrochemically active species in the electrolyte which is analogous to the part of the model where C_d is parallel to R_{ct}.

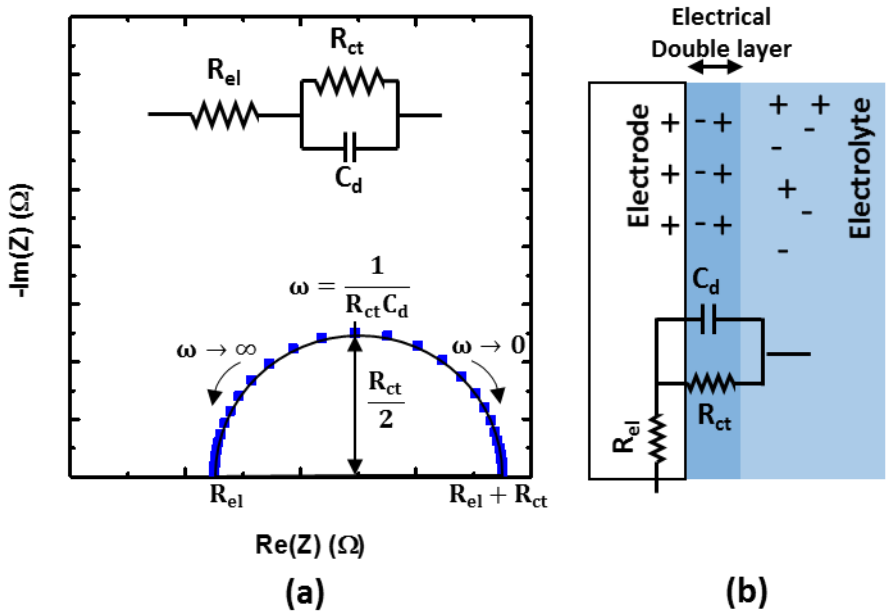

Figure 1.1-7. (a) Equivalent circuit model fitting in a Nyquist plot for an ideal electrode/electrolyte interface. (b) Physical interpretation of the equivalent circuit model

In actual experiments, most systems are non-ideal systems and thus cannot be accurately described by simple circuits. On this front, researchers have used composite components such as a Constant Phase Element (CPE) in order to describe the non-ideality before identifying the circuit elements and the physical phenomena described. To describe this consider the previous example, wherein in the ideal case scenario charge transfer will always occur at the interface and hence a resistor is used as the equivalent element. However, when the diffusion of the electroactive group is limiting the charge transfer at the interface, a Warburg impedance element is needed to be used to describe the interface. A Warburg impedance element is a CPE that is derived by Warburg in 1899 by using the diffusion equation of the mobile ions as a contribution to the current when solving for the double layer capacitance of the electrode.[44] The resultant Warburg element has a constant phase angle of 45 °, suggesting that this element consistently slows the applied voltage by a quarter of the period of the frequency. Once added to the circuit in Figure 1.1-7 as an extra resistor in series to charge transfer, the new model describes electrochemical reactions occurring at the electrode that can be limited by mass diffusion and not reaction kinetics. Thus, in this example, by

looking at the shape of the Nyquist plot, one can determine whether the electrochemistry at the interface is reaction rate limited or diffusion limited (Figure 1.1-8). Many more insights can be obtained based through EIS that can help diagnose many problems in fuel cells which are made up of many electrochemical interfaces.

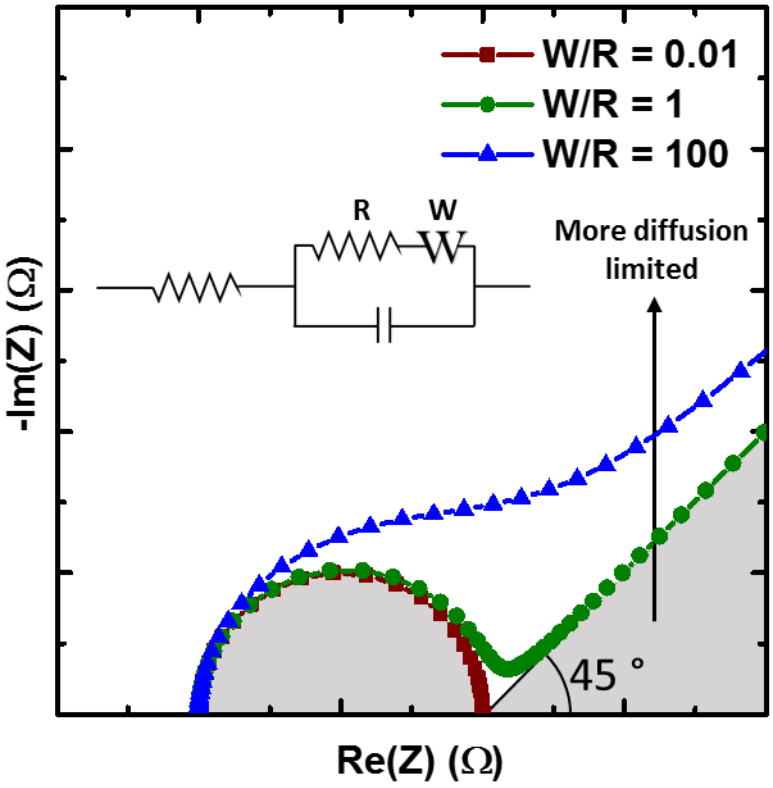

Figure 1.1-8. Simulated data with increasing Warburg impedance that reflects Nyquist plots on electrochemical reactions that are diffusion limited.

EIS can also be employed to characterize individual components of a fuel cell. In this project, EIS is used to evaluate ion conductivity in ion exchange membranes. Ion exchange membranes are placed across electrodes in a two or four probe configuration (Figure 1.1-9). In the two-probe mode, there are three components, the contact impedance of the platinum wires with the membrane and the impedance of membrane itself. By using a four-probe setup we can remove the contact impedance as the two voltage probes in the middle does not allow any current flow between them. Nonetheless, it has been found that as

long as the impedance of the membrane is much larger than the contact impedance, both measurements converge to the same result.[43,45] By increasing the electrode distance to beyond 3 cm, which ensures that the membrane impedance is higher, both methods would result in the same values.

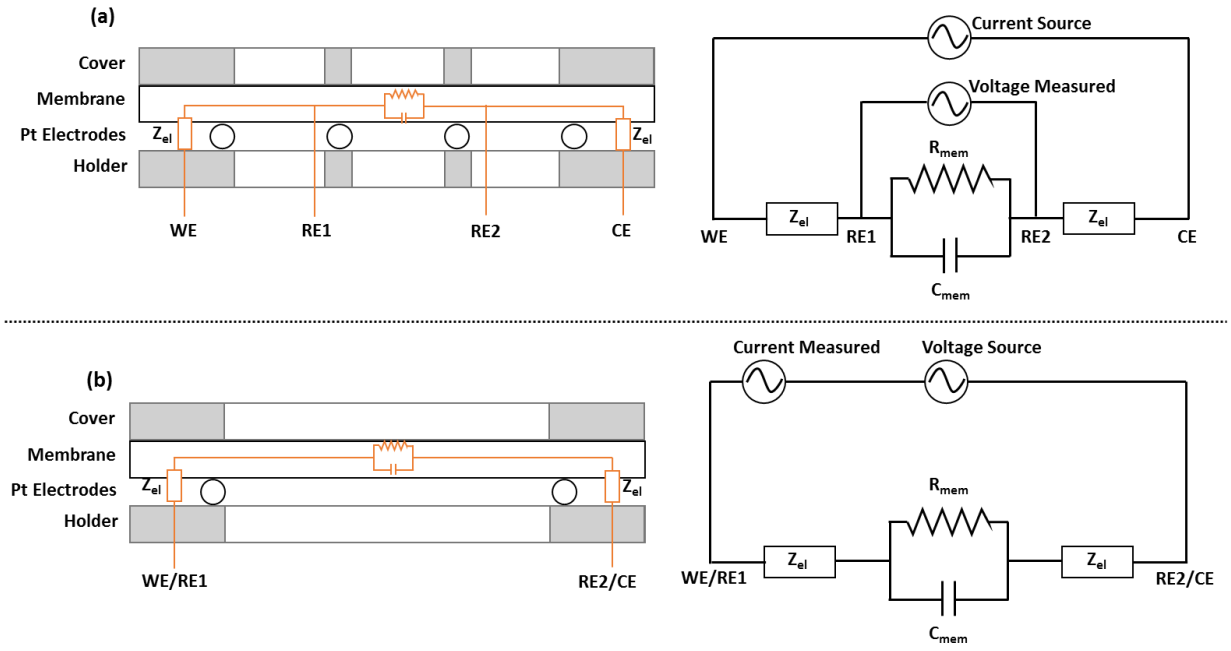

Figure 1.1-9. (a) Measurement setup in a four-probe configuration and the equivalent circuit. (b) Measurement setup in a four-probe configuration and the equivalent circuit. In both figures, WE, RE1, RE2 and CE are the electrode configuration for electrochemical interface (Solartron 1287) with an impedance analyzer (Solartron 1260).

With the four-probe setup, the impedance of the membrane can be independently modeled. The simplest ideal equivalent circuit of a resistor (R_{mem}) and capacitor (C_{mem}) in parallel is used to describe the ion exchange membrane (Figure 1.1-10). Once again, following the path of a mobile charge, the mobile charge in the membrane can either move through the membrane between the electrode or accumulate near the electrode to create capacitance (not to be confused with the double layer capacitance that would be accounted for in Z_{el}) and thus the parallel arrangement of R_{mem} and C_{mem}. The resultant Nyquist plot is a semicircle that is described by the equations in Figure 1.1-10.

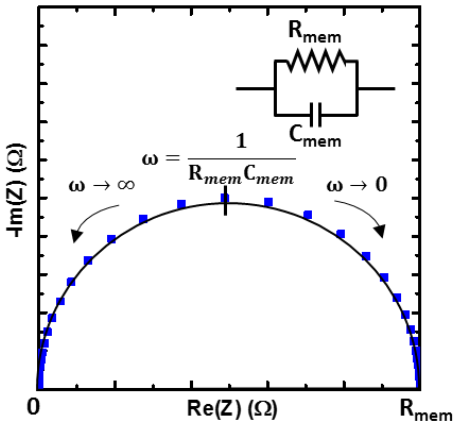

$$\frac{1}{Z_{mem}} = \frac{1}{R_{mem}} + i\omega C_{mem}$$

$$Z_{mem} = \frac{R_{mem}}{1 + (\omega R_{mem} C_{mem})^2} - \frac{i\omega R_{mem}}{1 + (\omega R_{mem} C_{mem})^2}$$

$$\omega \to 0, Z_{mem,Re} = R_{mem}$$

$$\omega \to \infty, Z_{mem,Re} = 0$$

Figure 1.1-10. Simulated Nyquist plot of an equivalent circuit model that is analogous to ion movement in an ion exchange membrane.

When measuring with a two-electrode setup, the impedance at the electrode/membrane interface contributes to the Nyquist plots. At low frequencies, charges accumulate at the electrodes because of increased capacitance from ion migration, resulting in a barrier for ion movement. Thus a diffusion limited response to the applied voltage which manifests in a 45 ° line on the Nyquist plot would be observed. However, the angle of the response at low frequency is found to increase with the size of the electrode[45] and may thus result in poor fit and error in the recorded bulk resistance of the membrane. (Figure 1.1-11)

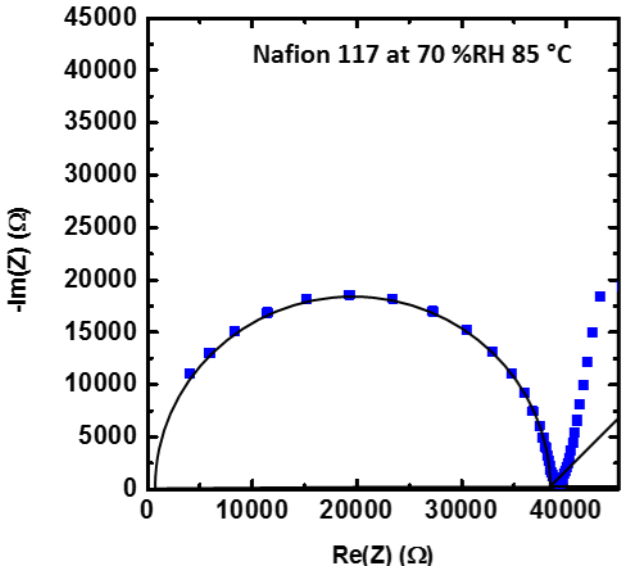

Figure 1.1-11. Nyquist plot of Nafion 117 taken at 70 %RH 85 °C. This plot represents a typical plot obtained throughout this project. Semicircle and 45° line is drawn in to show the high angle at low frequencies due to the usage of wide platinum strips to reduce contact resistance.

Other non-idealities such as inconsistent thicknesses or sample porosity can result in a tilt in the semicircle on the Nyquist plot.[5] In this case (Figure 1.1-12), the inconsistent thickness resulted in an inhomogeneous charge build up at the electrode/membrane interface. This behavior needs to be treated by replacing the capacitor with a constant phase element in order to correct the tilt.

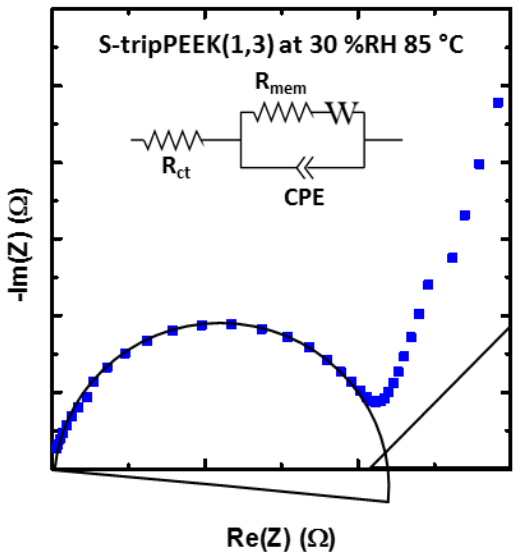

Figure 1.1-12. Experimental Nyquist plot of sample with uneven thickness. W in the equivalent circuit is the Warburg impedance expected at low frequency in a two electrode measurement. Tilted semicircle is specifically as a visual guide on how the CPE would cause a depression in the Nyquist plot.

In summary, when employed with care, EIS is a great technique that can be used to probe the individual components of a fuel cell and can be further employed to understand fuel cell performances. In the next two chapters, we will describe the approach in designing new polymers for ion exchange membranes in PEMFCs and AEMFCs and the evaluation of these new designs on improving ionic conductivity in these membranes using EIS. Chapter 1.2 will describe the work on using the triptycene functional group to enhance free volume in proton exchange membranes for higher conductivities at low relative humidity. Chapter 1.3 will describe the work on designing triptycene poly aryl ethers for AEMFCs.

1.2. Sulfonated Triptycene Poly Ether Ether Ketone as Free Volume Enhanced Proton Exchange Membranes in Fuel Cells

1.2.1. Introduction

Currently in PEMFCs, the most widely used PEMs are composed of perfluorinated poly(sulfonic acids), such as Nafion™. In these membranes, protons transported via proton transfer between sulfonic acid groups and water molecules in channels are generated by the directed assembly of the hydrophobic fluorous polymer structure. Nafion's chemical stability and excellent ionic transport properties are well known, but there are several important limitations to this material: (i) high cost of production; (ii) toxic intermediates from its synthesis; (iii) decomposition products release fluorocarbons into the environment; (iv) high permeability to gases and (v) limited chemical stability; and (vi) low proton conductivities above 90 °C which limits its commercially useful operational temperature window.[11,12,16,30,32,37,46,47]

Nafion's proton conductivity drops drastically at temperatures above 100 °C, wherein most of water in the membrane is lost to evaporation. Mechanistic and empirical studies on proton conductivity in Nafion suggest that proton conductivity is correlated to the degree of hydration within the material.[12,28,29,47–53] In sulfonic acid based membranes, it is the hydration of sulfonate groups which determine the amount of water in the membrane, and therefore the proton conductivity of the material. Hydrophilic sulfonate groups in the polymer coalesce, creating nanopores with high affinity for hydration, which form a percolated water network for proton conduction. At high temperatures and low relative humidity, water is lost to the environment and the nanopores collapse, resulting in a drastic decrease in proton conductivity.

One way to address the loss of water at low humidity and high temperature is to increase intrinsic free volume (defined at a molecular level) within the membrane. Intrinsic free volume can be introduced by adding bulky groups to sulfonic acid based membranes through rigid side chains,[37,54] chain branching,[55]

or by introducing bulky groups into the polymer backbone.[36,46,56,57] When the polymer membrane is completely dried, these rigid bulky groups prevent packing and produce nanovoids. However, this design is accompanied by the increased stress to the material that results in distorted bond angles and an increase in internal energy.[37] This internal energy is relieved when the membrane is exposed to small molecule solvents that can fill the voids and plasticize the polymer. Since water molecules are plasticizers for sulfonate polymers that are hydrophilic, it is energetically favorable for polymers with bulky groups to retain more water molecules at low humidity to prevent the energetic penalty from drying the membrane and thus retain a higher proton conductivity.

Although proton conductivity enhancements have been seen in the aforementioned earlier work, studies are lacking to best understand the factors that affect proton conductivity, including the ion exchange capacity (IEC), with a systematic control of free volume in the membranes. In this chapter, we report the use of the triptycene moiety to systematically control the intrinsic free volume in a PEEK-based PEM. The triptycene group increases the free volume in the polymer as a result of the three dimensional non-compliant triptycene group[38–40] and the phenyl rings associated with this structure allow for simple post polymerization sulfonation wherein the degree of sulfonation can be easily controlled. By synthesizing random copolymers with different numbers of triptycene groups and controlling the degree of sulfonation, membranes with similar IEC but different amounts of free volume were directly compared to elucidate the effect of free volume on proton conductivity. These results serve as a guide to new designs for PEMs that can be used at low humidity and high temperature.

1.2.2. Synthesis of Sulfonated Triptycene Poly(Ether Ether Ketone) Membranes

1.2.2.1. Synthesis of triptycene hydroquinone:

Triptycene hydroquinone was synthesized according to literature (Scheme 1.2-1).[57,58] Anthracene (35.65g, 200 mmol) and 1,4-benzoquinone (21.62g, 200 mmol) in 200 ml of toluene were heated under reflux for 6 h and cooled to room temperature. The precipitated triptycene benzoquinone was filtered and

washed with toluene and dried in a vacuum oven at 75 °C overnight. Triptycene benzoquinone was then added to 300 ml of glacial acetic acid and was heated under reflux. 1 ml of 40% hydrobromic acid was slowly added to the reaction and the reaction was left to stir under reflux condition for 3 h and left to cool to room temperature, precipitating triptycene hydroquinone that is filtered and dried in the vacuum oven at 75 °C overnight. Triptycene hydroquinone was obtained in 65% yield over two steps. ^{1}H NMR (400MHz, DMF-d7, 293K): 9.02 (2H, s), 7.44 (4H, m), 7.00 (4H, m), 6.42 (2H, s), 5.96 (2H, s); ^{13}C NMR (100MHz, DMF-d7, 293K): 147.38, 146.52, 133.48, 125.82, 124.64, 114.08, 48.43.

Scheme 1.2-1. Synthesis of triptycene hydroquinone

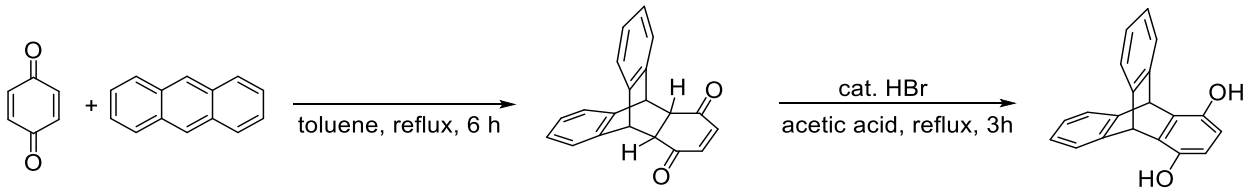

1.2.2.2. Synthesis of Triptycene Poly(Ether Ether Ketone) (tripPEEK(x,y)):

TripPEEK and its copolymers, designated tripPEEK(x,y) (Table 1.2-1), were synthesized through aromatic nucleophilic substitution (S_NAr) reaction between x equivalents of triptycene hydroquinone, y equivalents of hydroquinone and (x+y) equivalents of 4,4'-difluorobenzophenone (Scheme 1.2-2). The general procedure of polymerization, illustrated using tripPEEK(1,3), is as follows: in a flamed dried two-necked round bottom flask under nitrogen atmosphere with a Dean-Stark apparatus, triptycene hydroquinone (2.863 g, 10.0 mmol), hydroquinone (3.303 g, 30.0 mmol) and 4,4'-difluorobenzophenone (8.728 g, 40.0 mmol) was dissolved in anhydrous DMAc (80 ml) and anhydrous toluene (10 ml). Potassium carbonate (12.715 g, 92.0 mmol) was added and the reaction was heated to 140 °C for azeotropic distillation to remove water that was generated in the reaction. Once all the toluene was collected the reaction was heated under reflux conditions (165 °C) for 18 hours. The reaction was then precipitated in boiling water and filtered. The resulting polymer was purified by dispersing in boiling DMAc and precipitating twice in boiling water and twice in methanol. The resultant polymer was further purified with a Soxhlet extraction

with acetone for two days, yielding an off-white polymer powder that was dried in the vacuum oven for two days at 75 °C.

Scheme 1.2-2. Polymerization of TripPEEK(x,y) through SNAr reaction

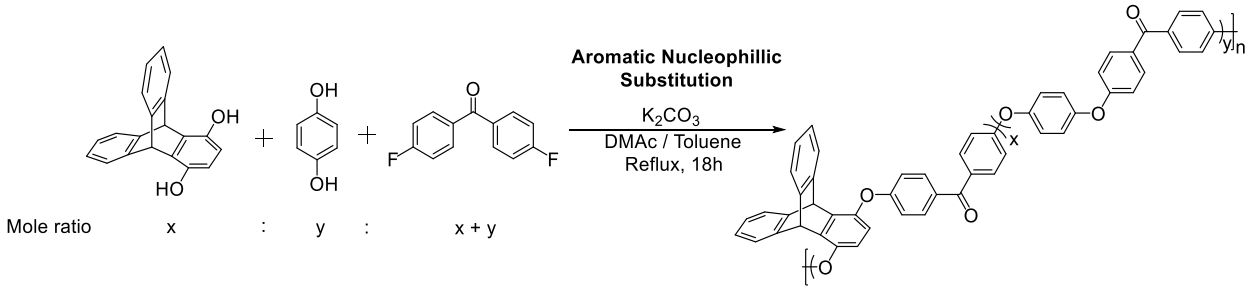

Table 1.2-1. Mole ratio of monomers of polymers. Average molecular weight per repeat unit is calculated in equation below

	Mole ratio			
Designation	triptycene hydroquinone (x)	hydroquinone (y)	4,4'-difluorobenzophenone (x+y)	Average molecular weight per repeat unit (g/mol)
tripPEEK(1,0)	1	0	1	464.5
tripPEEK(1,1)	1	1	2	376.4
tripPEEK(1,3)	1	3	4	332.4
PEEK	0	1	1	288.3

$$\text{Ave. Molecular Weight per repeat unit} = \frac{x(464.5) + y(288.3)}{x + y}$$

1.2.2.3. Synthesis of sulfonated tripPEEKs (S-tripPEEK) and sulfonated PEEK (S-PEEK):

TripPEEK and PEEK were sulfonated with concentrated sulfuric acid. 0.5g of polymer was stirred in 10 ml of concentrated sulfuric acid for 4 hours to dissolve the polymer before the solution was heated to 65 °C and left to stir for 1 hour. The degree of sulfonation can be increased with a longer reaction time at 65 °C. Sulfonated polymers were precipitated in ice water, filtered and rinsed with deionized water and transferred into dialysis tubing (Molecular weight cut off of 10000 Da) for extraction with deionized water until pH neutral.

1.2.2.4. Formation of proton exchange membranes:

S-trpPEEKs were dissolved to form 10 wt% solutions in dimethylformamide. 2.0 ml of the polymer solution was dispensed on a 75 mm × 25 mm glass slide and heated to 75 °C for 2 hours before drying overnight under vacuum at 75 °C. Free standing membranes with thicknesses between 100-150 µm were peeled off the glass slides and cut to sizes needed for further experiments. Prior to any characterization, the membranes were soaked in 2.0 M sulfuric acid for 24 hours to protonate the membranes. Thereafter, the membranes were transferred into deionized water and soaked for 24 hours, replacing the deionized water every 8 hours to remove residual acid.

1.2.2.5. Pretreatment of Nafion117

Nafion 117 membranes were pretreated as reported in literature to remove organic impurities and reprotonate all sulfonic acid groups before all measurements.[53] Nafion 117 membranes were boiled in a 3% H_2O_2 aqueous solution for 1 hour, rinsed with deionized water and boiled in a 0.5 M sulfuric acid solution for 1 hour. The protonated membranes were then soaked in deionized water for 24 hours, switching the deionized water every 8 hours, to remove residual sulfuric acid. The pretreated membrane were then kept in deionized water before testing.

1.2.3. Characterization of Membranes

1.2.3.1. Ion exchange capacity:

Ion exchange capacity (IEC) is the measure of the number of acid groups that contributes to the dissociation of protons in the membrane which has been found to directly affect proton conductivity. IEC was determined by titration with 0.01 M sodium hydroxide solution. Membranes were soaked in 2.0 M HCl overnight to protonate all sulfonate groups. Protonated membranes were rinsed with deionized water 3 times and soaked in 2.0 M NaCl solution overnight for ion exchange. The solution was then titrated with 0.01 M (M_{NaOH}) sodium hydroxide solution (standardized with 0.010 M potassium hydrogen phthalate) until pH 7.0 using a pH meter and the volume of base (V_{NaOH}) was used to calculate IEC with equation below, where m_{dry} is the mass of dried membrane.

$$\mathrm{IEC} = \frac{(\mathrm{V_{NaOH}})(\mathrm{M_{NaOH}})}{\mathrm{m_{dry}}}$$

1.2.3.2. Water uptake and hydration number:

Water uptake (WU) and hydration number (λ) at 20 %RH were obtained through thermogravimetric analysis (TA instruments TGA Q5000). All measurements were done in triplicate and averaged.

Small pieces of S-tripPEEK membranes were first dried in a vacuum oven at 100 °C for 18 hours and removed to equilibrate at 20 %RH at room temperature over 48 hours. The equilibrated film was heated in the TGA from 25 °C to 150 °C at a heating rate of 10 °C/min and held at 150 °C for 2 hours. The mass loss below 150 °C was attributed to the loss of water and was used to calculate water uptake (WU) using equation below where $m_{25\,°C}$ is the mass at 25 °C, $m_{150\,°C}$ is the mass after holding at 150 °C for 2 hours.

$$\text{Water uptake (WU)}(\%) = \frac{\mathrm{m_{25\,°C}} - \mathrm{m_{150\,°C}}}{\mathrm{m_{150\,°C}}} \times 100\%$$

Hydration number, λ, which is defined as the number of water molecules for every sulfonate group can be calculated using the equation below, where MW_{H2O} is the molecular weight of water and WU is water uptake as reported in percent.[32]

$$\text{Hydration number } (\lambda) = \left(\frac{\mathrm{WU}/100}{\mathrm{MW_{H_2O}}}\right)\left(\frac{1}{\mathrm{IEC}}\right)$$

1.2.3.3. Fractional free volume of PEMs:

Fractional free volume (FFV) is defined as the fraction of volume in PEMs that is not occupied by the polymer and is determined using the equation below where V is specific apparent volume of the PEM and V_0 is specific skeletal volume of the polymer.

$$\mathrm{FFV} = \frac{\mathrm{V} - \mathrm{V_0}}{\mathrm{V}}$$

To obtain the specific volumes needed, before any measurements, all PEMs were dried in a vacuum oven at 85 °C for over 20 hours and quickly placed into a dessicator after drying to cool to room temperature to prevent adsorption of atmospheric water. Polymers were then weighed quickly with a microbalance (Mettler Toledo) to obtain the dry mass (m_{dry}).

Specific apparent volume (V) per mass of the PEMs were calculated based on mass and dimensions of the dry PEM using the equation below. Thicknesses (t) were measured using a Mitutoyo micrometer and averaged over 9 locations on the membrane. Lengths (l) and widths (w) were measured using a Mitutoyo digital calipers and averaged over 3 locations on the membrane. Both the micrometer and digital calipers have been calibrated by the manufacturer and comes with a NIST traceability certificate.

$$V = \frac{(t)(l)(w)}{m_{dry}}$$

Specific skeletal volume (V_0) of polymers were obtained via helium pycnometry (Micromeritics AccuPyc II 1340). The dried membranes were quickly loaded into the pycnometer to obtain the corresponding skeletal volume (V_{dry}). Helium pycnometry was done at 19.5 psi helium with 4 purge cycles and averaged over 5 measurements. V_0 was then calculated using the equation below.

$$V_0 = \frac{V_{dry}}{m_{dry}}$$

1.2.3.4. Proton conductivity measurements:

Proton conductivity (σ) at various humidity and temperature was obtained through electrochemical impedance spectroscopy (EIS) using a Biologic SP 200. Films were placed across 2 platinum electrodes spaced 1 cm apart. The spacing of 3cm was chosen as proton conductivity measured from two-probe

measurements at electrode distances above 2.7cm are similar to four-probe measurements, minimizing the variance between the two configurations.[45]

For proton conductivity in water, the setup is placed in a water bath at 20 °C. For proton conductivity at different relative humidities, the setup is placed in a humidity chamber (Espec BTL433). All membranes were tested with the same heating and cooling profile where membranes were measured at the highest relative humidity (90 %RH) first, starting from 85 °C and cooling down to 25 °C in 10 °C step and equilibrating for 1 hour before each measurement. For relative humidity below 30 %RH, the membranes were tested from 85 °C to 60 °C in 5 °C steps due to limitations in the dehumidifier of the humidity chamber.

Measurements were done in Potentio Electochemical Impedance Spectroscopy (PEIS) mode with a mean AC voltage 0 V and an amplitude of 0.1 V over a frequency range of 1MHz to 0.1 MHz. The high frequency intersect between the curve and the real axis of the Nyquist plot was recorded as bulk resistance of the membrane (R). Proton conductivity (σ) was then calculated using equation below where *l* is the length between the electrodes, *w* is the width of the membrane and *t* is the thickness of the membrane. All dimensions were measured at 20% RH. Activation energy was calculated based on an Arrhenius relation.

$$\sigma = \frac{l}{(\mathrm{R})(t)(w)}$$

$$\sigma = \mathrm{A}e^{-\left(\frac{\mathrm{E_a}}{\mathrm{RT}}\right)}$$

1.2.4. Results and Discussion

1.2.4.1. Physical properties of tripPEEKs

Comparing tripPEEKs with PEEK showed that the inclusion of the triptycene moiety added steric bulk which prevented π-stacking and inhibited crystallization, as observed in PEEK (Figure 1.2-1. DSC thermograms of (a) tripPEEK(1,0), (b) tripPEEK(1,1), (c) tripPEEK(1,3) and (d) PEEK. Heat flows are measured from 25 °C to 350 °C at a heating and cooling rate of 10 °C/min.). DSC thermograms of all tripPEEKs showed only a single glass transition and no melting transition, suggesting that (i) tripPEEK(1,1)

and tripPEEK(1,3) are random copolymers and (ii) tripPEEKs do not crystallize. The absence of a crystalline phase makes tripPEEKs more soluble than PEEK and allows for solubility in common organic solvents, such as chloroform, dichloromethane and boiling polar solvents, such as dimethylacetamide and dimethylformamide. A benefit of the relative solubility of tripPEEKs is that ^{1}H NMR spectra can be obtained. With enhanced solubility, tripPEEKs polymerization also proceeds to higher degrees of completion to provide a high molecular weight with soluble fractions have a number average molecular weight of more than 100 kDa with respect to polystyrene standards. High molecular weights in tripPEEKs allow for the formation of smooth and homogenous free-standing membranes.

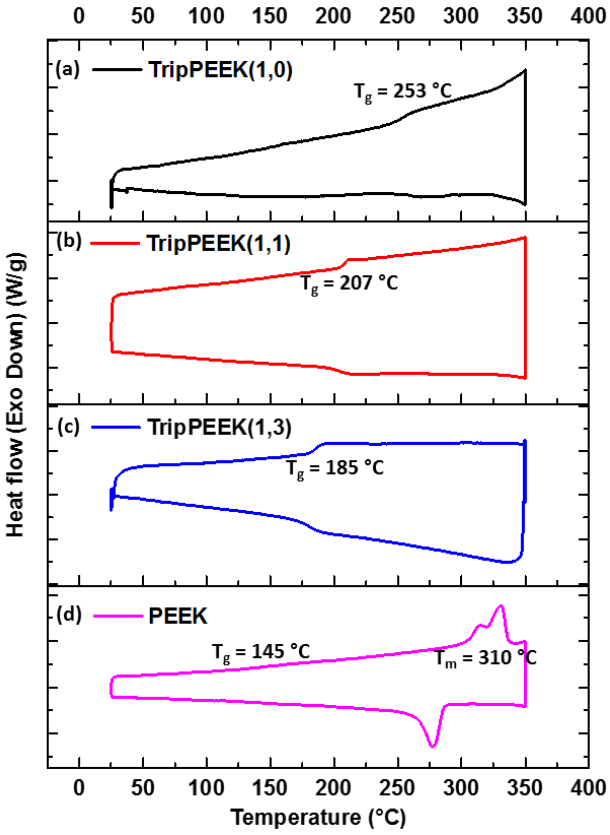

Figure 1.2-1. DSC thermograms of (a) tripPEEK(1,0), (b) tripPEEK(1,1), (c) tripPEEK(1,3) and (d) PEEK. Heat flows are measured from 25 °C to 350 °C at a heating and cooling rate of 10 °C/min.

In addition to enhanced solubility, triptycene moieties also affect the density of the tripPEEK polymers. (Table 1.2-2) Since the triptycenes increase the free volume in the material, it was expected that

with more of the triptycene moiety present, the density will be lower. However, since adding triptycene moieties also increases the mass of repeating unit, the net effect resulted in the density of tripPEEK(1,0) being higher than tripPEEK(1,1). By normalizing the densities with the average molecular weight of a repeating unit, the volume per mole of repeating unit shows that with more triptycene in the polymer the higher the volume per repeat unit is obtained, suggesting that triptycene can contribute to additional volume in each repeat unit.

Table 1.2-2. Densities and volume per repeat unit of tripPEEKs.

	Average MW per repeat unit (g/mol)	Skeletal density (g/cm^3)	Volume/repeat unit (cm^3/mol)
TripPEEK(1,0)	464.5	1.299	357.6
TripPEEK(1,1)	376.4	1.276	295.0
TripPEEK(1,3)	332.4	1.327	250.5
PEEK	288.3	1.321	218.2

1.2.4.2. Properties of sulfonated tripPEEKs (S-tripPEEK):

The sulfonation of tripPEEKs using concentrated sulfuric acid was successful as indicated by the new peaks in the IR spectra (Figure 1.2-2). The peaks at 1180 cm^{-1} are assigned to the S=O stretch and 1050 cm^{-1} from symmetric sulfonate group stretch.

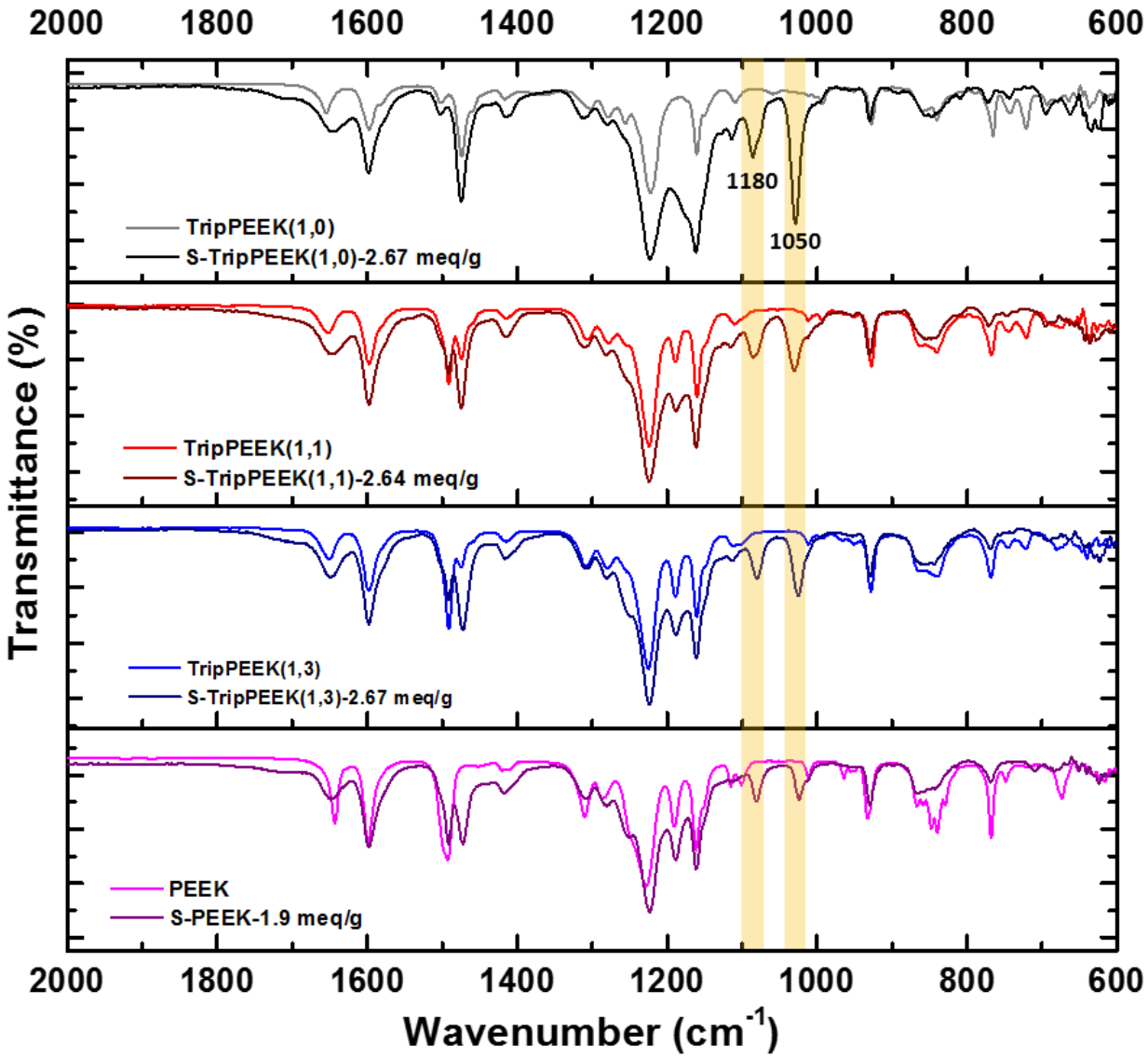

Figure 1.2-2. FTIR spectra for tripPEEKs and S-tripPEEKs. Peaks at 1180 cm^{-1} and 1050 cm^{-1} are vibrational peaks from the sulfonate group.

^{1}H NMR analysis of tripPEEK(1,0) and S-tripPEEK(1,0) (Figure 1.2-3) suggests that some of the sulfonate groups were added to the extended 'wings' of the triptycene group. Addition restricted to the phenyl ring with the ether linkage would result in a lone H on this ring that is assigned an integration of 1H. The total aromatic triptycene peaks integrates to 16 relative to the distinctive bridgehead protons, indicating that sulfonate groups are also added to the extended rings of the triptycene group. Sulfonation should preferentially occur on the more electron rich ring with 1,4-diether linkages. However, since concentrated

sulfuric acid is both a sulfonating reagent and solvent, this provides for aggressive sulfonation conditions that can add SO_3H groups to the other two phenyl rings of the triptycene. The ketone bearing phenyl rings are deactivated and the integration relative to the bridgehead protons indicates that under the conditions used no sulfonation occurs on these rings. It is known that electrophilic substitution of triptycene occurs in a sequential fashion when adding electrophilic groups,[38] and hence, should follow the same trend with sulfonation. The reduction in rate of addition with each sequential addition resulting in a slower rate is a result of homo-conjugation. As a result, the signal at approximately 7.05 ppm suggests that on average we have selectively sulfonated the electron rich ring and one additional ring of the triptycene.

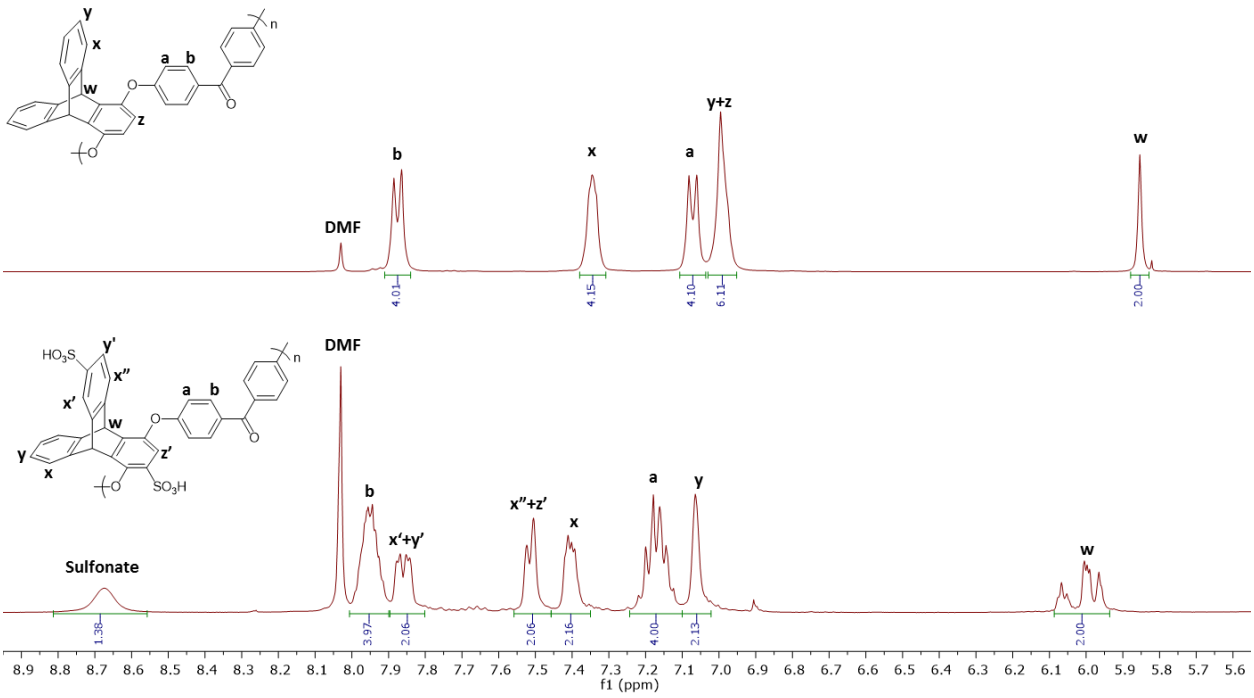

Figure 1.2-3. ^{1}H NMR of tripPEEK(1,0) and S-tripPEEK(1,0). S-tripPEEK was sulfonated with concentrated sulfuric acid at 65 °C for 1 hour, resulting in successful sulfonation of 2 out of the 3 phenyl rings on the triptycene group.

Thermogravimetric analyses of S-tripPEEKs and S-PEEK (Figure 1.2-4) showed an initial mass loss that is associated with the loss of water that is attached to the hygroscopic sulfonate groups. The mass loss at 350 °C was attributed to the decomposition of sulfonate groups. Hence, S-tripPEEKs are stable to 350 °C, which is well above the operating temperature of up to 200 °C in PEMFCs[17,59].

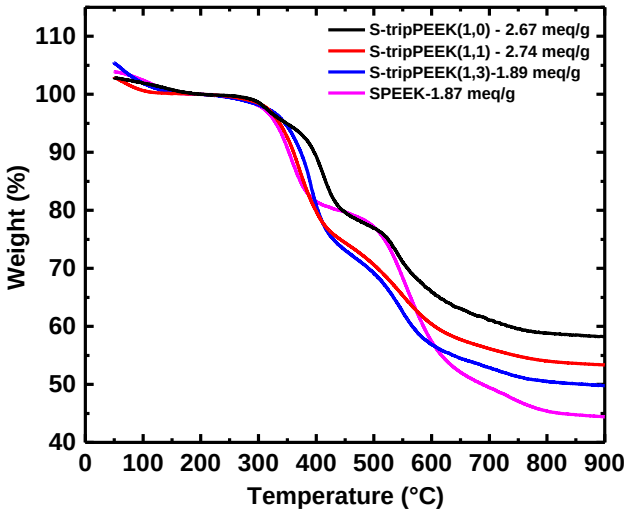

Figure 1.2-4. TGA of S-tripPEEKs and S-PEEK from 50 °C to 900 °C at a heating rate of 20 °C/min. TGAs are normalized such that 100% is weight percent after the mass loss associated to water.

As there are more sites available for functionalization with sulfonate groups in tripPEEKs compared to PEEK, S-tripPEEKs with a larger range of degrees of functionalization and thus different IECs were prepared for evaluation (Table 1.2-3). The table shows the corresponding molecular weights of the membranes with different IEC are listed. Aggressive sulfonation results in some degradation of the polymer, as for each of S-tripPEEK(1,0), S-tripPEEK(1,1) and S-tripPEEK(1,3), higher degree of sulfonation resulted in a molecular weight reduction. Nonetheless, S-tripPEEKs maintain absolute molecular weight of the polymers in the range of 33-100 kDa and still produced robust free standing membrane for further testing.

Table 1.2-3. Range of molecular weight, IEC and degree of sulfonation of all S-tripPEEKs and SPEEKs made. Limits of IECs are listed with respect to the molecular weight of the corresponding polymer. High IEC, with high degree of sulfonation results in lower molecular weight of the polymer. Degree of sulfonation is defined as ratio of sulfonate groups to reactive phenyl ring.

	Mn (kg/mol)	Mw (kg/mol)	IEC (meq/g)	Degree of Sulfonation
StripPEEK(1,0)	60.5 – 85.2	103 – 146	3.35 – 2.67	0.67 – 0.53
StripPEEK(1,1)	35.5 – 77.0	50.3 – 136	2.79 – 2.64	0.66 – 0.63
StripPEEK(1,3)	33.9 – 61.8	64.8 – 91.5	2.67 – 1.89	0.75 – 0.52
SPEEK	40.5	62.3	1.87	0.63

1.2.4.3. Free volume enhanced proton conductivity:

In an effort to deconvolute the effect of free volume and IEC on proton conductivity at various levels of relative humidity, S-tripPEEK(1,0), (1,1) and (1,3) membranes of similar IEC were chosen for a comparative study (Table 1.2-4). Similar to the corresponding tripPEEKs, the skeletal densities of S-tripPEEKs also do not necessarily decrease with increasing number of triptycene groups. Calculations for the volume per repeat unit again show increases with increasing ratios of triptycene moiety in the polymer, suggesting that the fluctuations in skeletal density are the result of the increase in mass contributed from the bulky triptycene groups. More importantly, the fractional free volume (FFV) was observed to increase with the number of triptycene moiety in the polymer. Since the dimensions used to calculate FFV are the same ones used for the calculation in proton conductivity, FFV is directly related to the amount of space water molecules can occupy within the membrane, which in turn affects the proton conductivity of the membrane.

Table 1.2-4. Properties of chosen S-tripPEEK membranes

	IEC (meq/g)	MW / repeat unit (g/mol)	Skeletal Density (g/cm^3)	Vol per repeat unit (cm^3/mol)	V_0 (cm^3/g)	V (cm^3/g)	FFV (cm^3/cm^3)
S-tripPEEK (1,0)-2.67	2.67	590.7	1.405	420	0.712	0.874	0.19
S-tripPEEK (1,1)-2.64	2.64	477.2	1.380	346	0.724	0.855	0.15
S-tripPEEK (1,3)-2.67	2.67	422.6	1.422	293	0.703	0.793	0.11

Proton conductivities of these membranes, as compared to SPEEK at 85 °C over the full range of relative humidity (Figure 1.2-5), show the enhancement in proton conductivity in S-tripPEEKs. At 20 %RH, S-tripPEEKs have proton conductivities of 0.02 – 0.4 mS/cm compared to Nafion 117 at 0.0014 mS/cm and SPEEK at 0.0015 mS/cm. Similarly at 90 %RH, S-tripPEEK membranes exhibit proton conductivities of 0.11 – 0.33 S/cm, as compared to Nafion 117 at 0.02 S/cm and SPEEK at 0.075 S/cm. Conductivities of

Nafion 117 observed were lower than expected due to the heating profile of the measurement. By measuring the membranes at 85 °C, Nafion 117 membranes were 'heat-treated', resulting in a decline in conductivity similar to Nafion 117 membranes that were heat treated at temperatures above 80 °C as reported.[53] This further suggests that S-tripPEEK membranes are more suitable than Nafion 117 for fuel cell operations above 80 °C.

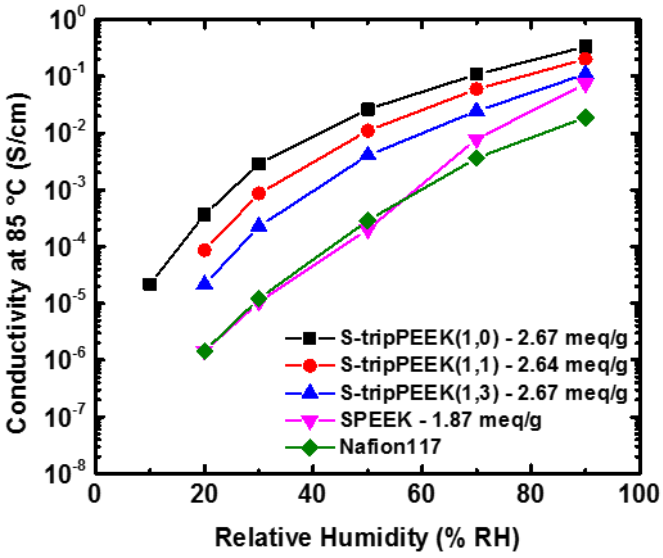

Figure 1.2-5. Proton conductivity of membranes 85 °C over different levels of relative humidity.

More importantly, comparing within the S-tripPEEKs membranes clearly reveals that increases in FFV enhances proton conductivities, especially at low relative humidity. Across the full range of relative humidity, S-tripPEEK(1,0) exhibited the highest proton conductivities followed by S-tripPEEK(1,1) and S-tripPEEK(1,3). The enhancement that correlates with FFV varies at different levels of humidity; S-tripPEEK(1,0) has a conductivity 20 times higher than S-tripPEEK(1,3) at 20 %RH but is only 3 times higher at 90 %RH. At low humidity, when the water within the membrane is reduced, the increased free volume in the membrane allowed around 50% more water uptake within the S-tripPEEK(1,0) membrane as compared to S-tripPEEK(1,3) (Table 1.2-5) which helps to maintain the hydration number at lower humidity, and hence the enhancement.

Table 1.2-5. Water uptake of S-tripPEEK membranes at 20 %RH

	IEC (meq/g)	FFV (cm^3/cm^3)	Water Uptake (%)	Hydration number, λ
S-tripPEEK (1,0)-2.67	2.67	0.19	9.7	2.02
S-tripPEEK (1,1)-2.64	2.64	0.15	6.6	1.41
S-tripPEEK (1,3)-2.67	2.67	0.11	6.4	1.33

However, at higher humidity the FFV enhanced water uptake can lead to polymer swelling, which can isolate sulfonates and the conductivity enhancement from FFV is reduced. This effect has amplified consequences when the membranes were measured in water at 20 °C. Here S-tripPEEK(1,0) membranes adsorbed water and swelled to such an extent that the sulfonate groups were diluted to the point that the proton conductivity is reduced (Figure 1.2-6). Proton conductivities of S-tripPEEK(1,1) were higher than both S-tripPEEK(1,3) and S-tripPEEK(1,0) and is attributed to the larger hydration number observed in S-tripPEEK(1,0). As a side note, S-tripPEEK(1,0) membranes swell by more than 200% in water and are soluble in water at temperatures above 50 °C.

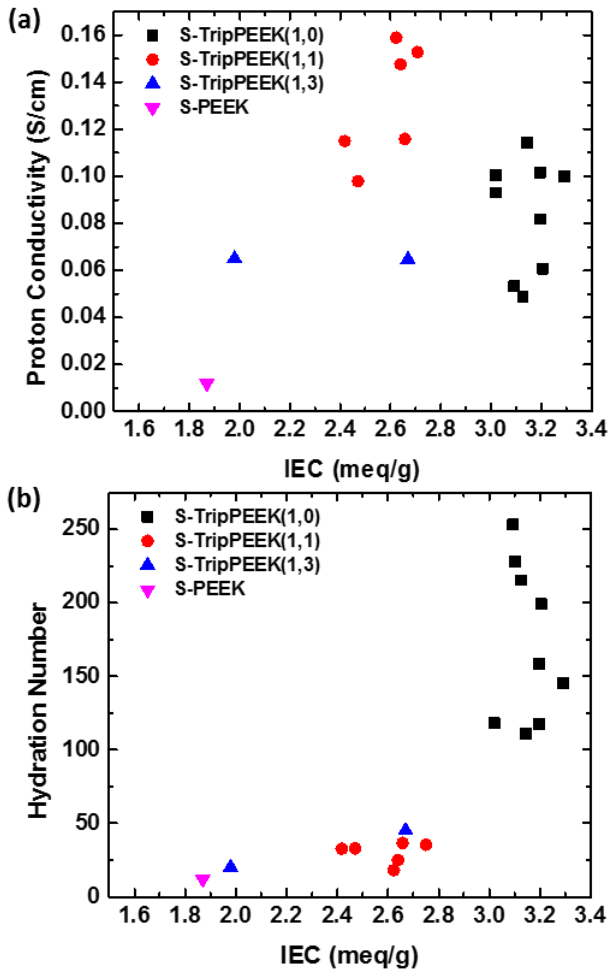

Figure 1.2-6. (a) Proton conductivity in water and (b) hydration number of membranes in water. Hydration number is defined as the number of water molecules for every sulfonate group in the membrane.

The dilution of the sulfonates in hydrated S-tripPEEK(1,0) is also consistent with the measured water melting point depressions (Figure 1.2-7). Within the membrane, water aggregates around the hydrophilic sulfonate groups, solvating them to release protons. Thus, we can consider the sulfonate groups in the membrane as impurity in the water phase. At a smaller hydration number, there are more sulfonate groups with respect to water molecules in the membrane, resulting in a larger melting point depression of water in the membrane. Hence, with lower hydration numbers, S-tripPEEK(1,3) and (1,1) shows melting point depressions of -25 to -30 °C while no melting point depression was observed in hydrated S-tripPEEK(1,0) membranes.

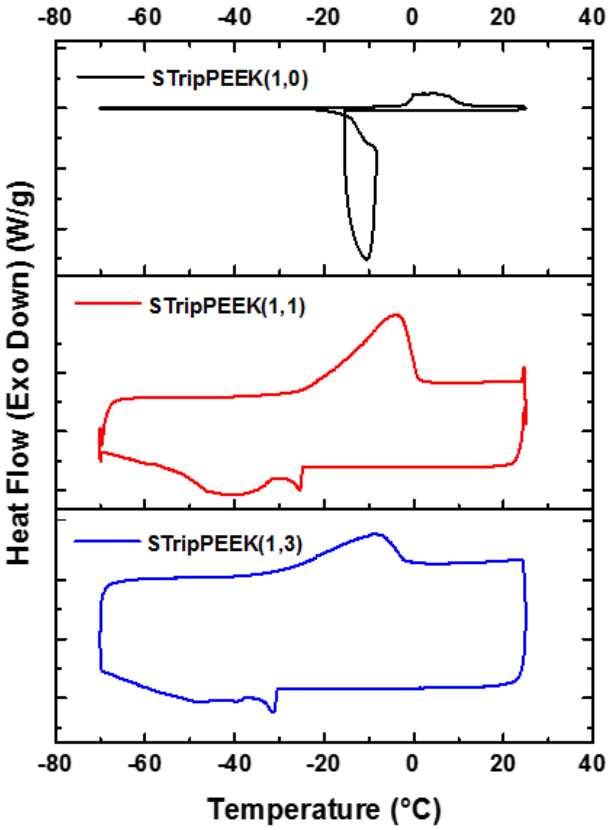

Figure 1.2-7. DSC thermograms of hydrated S-tripPEEK films from -70 C to 25 C at a heating and cooling rate of 10 C/min. The loop observed in the cooling cycle of S-tripPEEK(1,0) is due to the supercooling of the water phase that resulted in rapid crystallization of ice that raised the temperature of the sample.

To further illustrate the dependence on hydration number and improvements resulting from increasing intrinsic free volume in the membrane, activation energies at different levels of humidity were compared (Figure 1.2-8). Activation energies are a measure of the ease of proton transport in the membrane and are highly dependent on water uptake in the membrane. Proton exchange membranes loses water as the relative humidity decreases, resulting in reduced proton conductivity and increased activation energy.[47,51,60,61] Figure 1.2-8 reveals that S-tripPEEKs has a much wider window of relative humidity wherein the activation energies for proton transport were low. More importantly, as the intrinsic free volume increases from S-tripPEEK(1,3) to (1,1) to (1,0), the activation energies decreased across the whole range of humidity. This result suggests that intrinsic free volume enhances the ease of proton transport.

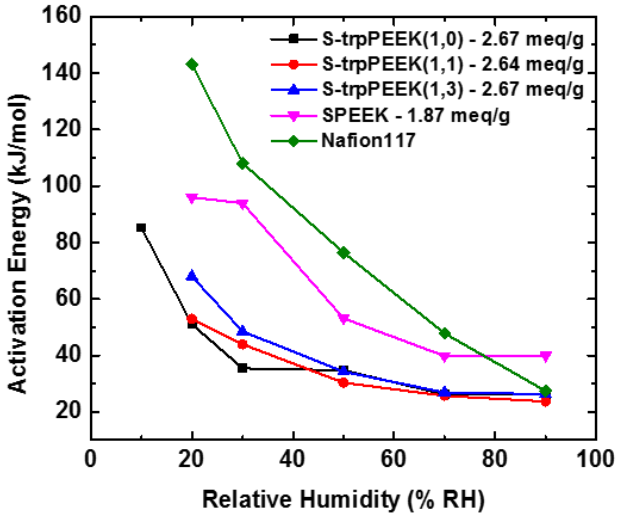

Figure 1.2-8. Plot of activation energy observed in each membrane from 20 %RH to 90 %RH.

1.2.5. Conclusion

In summary, a series of proton exchange membranes based on S-tripPEEK with high IEC values and varying levels of intrinsic free volume were synthesized. The membranes exhibit high proton conductivity of 334 mS/cm at 90 %RH and 0.37 mS/cm at 20 %RH at 85 °C. Studies of membranes with similar IECs, but increasing intrinsic free volume, at low humidity allowed for successful deconvolution of the effect of free volume from IEC. With increased free volume, water uptake at low humidity increased, resulting in higher conductivities and a reduction in activation energies for proton conductivity. Considering that PEMFCs should ideally operate at temperatures above the boiling point of water, wherein the humidity is low, intrinsic free volume of PEMFCs should be a major design element.

1.3. Anion Exchange Membrane using Triptycene Poly Aryl Ethers

1.3.1. Introduction

Anion Exchange Membrane Fuel Cells (AEMFCs) are highly sought after in the field as a result of several advantages over PEMFCs.[3,10,62,63] First, they have more efficient catalytic reactions at the electrode that requires less expensive metal systems such as copper. Second, the catalyst systems used are less prone to poisoning and are more tolerant to fuel impurities. However, current anion exchange membranes are less ion conductive than their proton exchange counterparts. Among the AEMFCs, alkaline anion exchange membrane fuel cells (AAEMFCs) have the greatest potential to improve ion conductivity, given that hydroxide ions are the fastest conducting anion.[62] However, AAEMFCs are currently limited by the scarcity of alkaline anion exchange membranes that have a high hydroxide ion conductivity and high stability at operating conditions of AEMFCs.

The main reason of the instability is due to the reactivity of hydroxide ion that is transported in the membrane at operating temperatures ranging from 20 °C to 200 °C. In this temperature range, hydroxide ions can degrade cationic groups in the polymer structures. In quaternary ammonium ion based AEMs, degradation of the ammonium group can occur through (i) through the β-hydrogen by Hofmann elimination, (ii) nucleophilic substitution, and (iii) ylide formation (Figure 1.3-1a).[3,10,62] Furthermore, Hickner et al. have also shown that electron withdrawing heteroatoms on the polymer backbone can also affect the stability of the quaternary ammonium group through inductive effects (Figure 1.3-1b).[64]

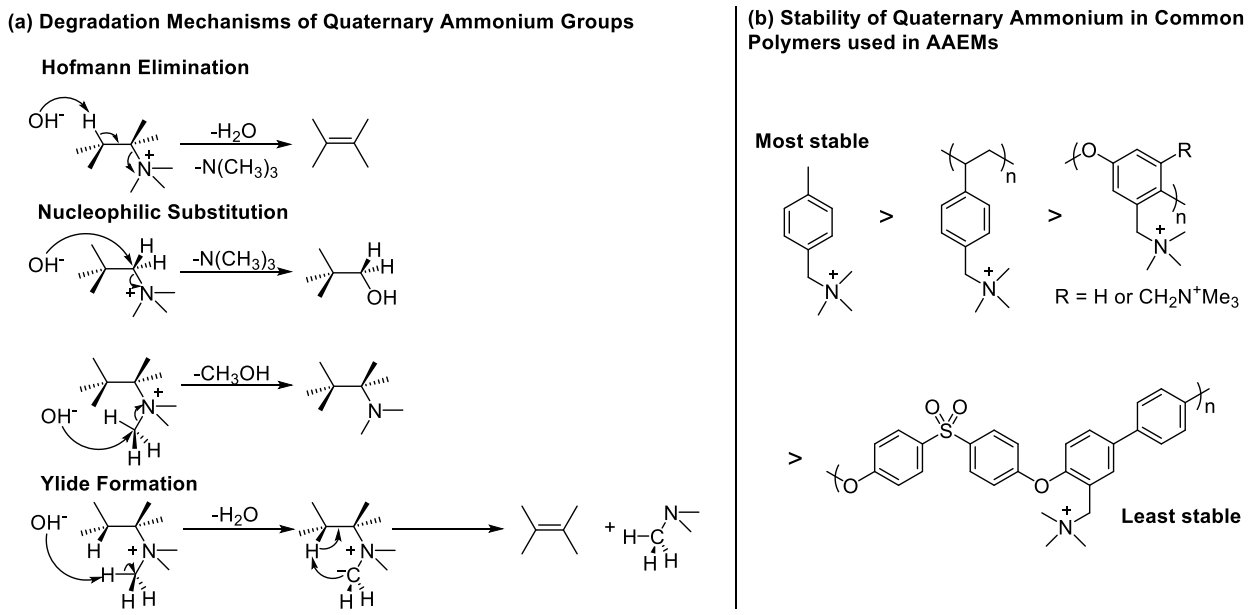

Figure 1.3-1. (a) Degradation mechanisms of quaternary ammonium salts in AAEMs. (b) Stability of quaternary ammonium functional groups with respect to the base polymer structure.[64]

New cationic side groups that are stable under alkaline conditions were developed and extensively reviewed over the years.[7,8,10,65] For example, tertiary amine groups that are stabilized as a result of (i) sterically hindering groups such as 1,4-diazabicyclo[2.2.2]octane (Figure 1.3-2a) and hexamethylenetetramine (Figure 1.3-2b) and (ii) resonance stabilized groups such as substituted guanidines (Figure 1.3-2c), imidazoles (Figure 1.3-2d) and pyridines (Figure 1.3-2e and f). In the case of imidazolium AAEM, further functionalization with a bulky group on the R_2 position can further improve the stability of imidazolium groups.[10,62]

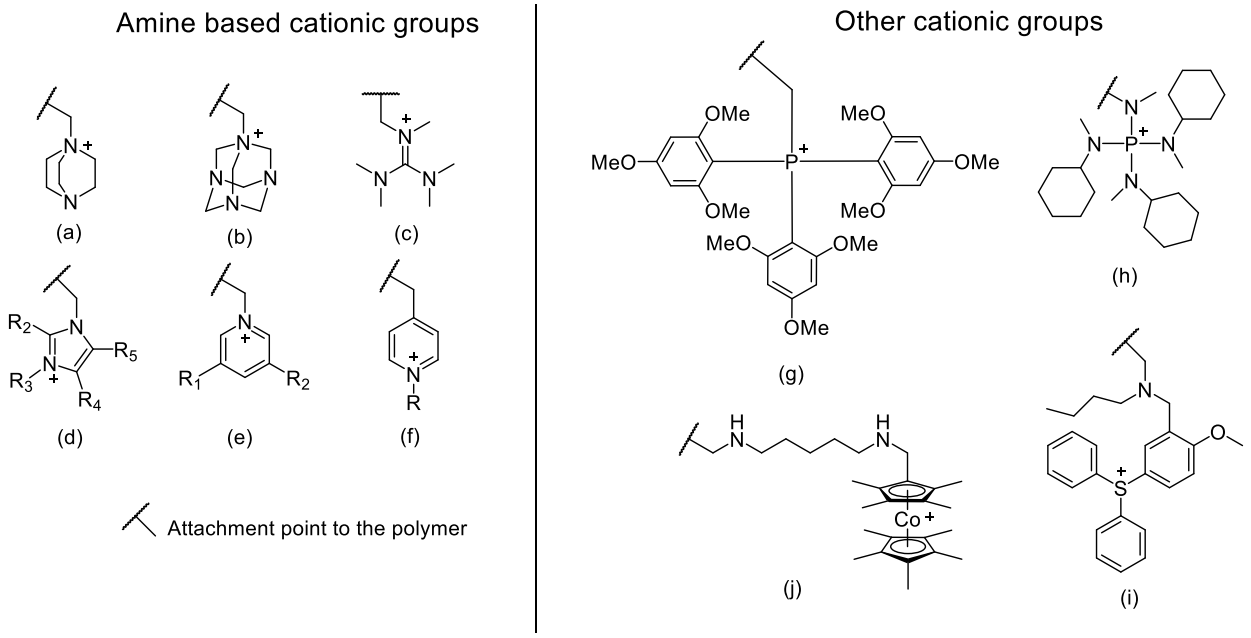

Figure 1.3-2. Functional groups that are found to be stable under alkaline conditions.

Other than nitrogen based cationic groups, sterically bulky phosphoniums[66,67] (Figure 1.3-2g and h) and sulfoniums[68] (Figure 1.3-2i) have also been found to be stable in bases at relevant operating temperatures as a result of steric hinderance around the charged centers. Finally, metallic cations cobaltocenium (Figure 1.3-2j) was reported to be stable for hydroxide exchange membranes after complete methylation of the cyclopentadiene rings as the cobalt center was stabilized by the electron donating methyl groups.[69]

Thus, increasing the stability of these membranes through introduction of stable cationic groups is as crucial as improving the conductivity by increasing the concentration of ions and the mobility of the ions as discussed in 1.1.1. In this project, triptycene is introduced into the poly(ether ether ketone) and poly(ether sulfone) and further functionalized into anion exchange membrane. Although poly(aryl ether)s contain electron withdrawing groups that would affect the stability of the cationic group as found by Hickner et al.[64], poly(aryl ether)s have the thermal stability and mechanical strength that are crucial to the operation of fuel cells. Thus, triptycene moiety is introduced into poly(ether ether ketone) (Section 1.3.2) and poly(ether

sulfone) (Section 1.3.3) for two purpose: (i) adding free volume into the membrane to allow higher mobility of the larger hydroxide ions and (ii) stabilizing the cations by attaching them to the extended wings of the triptycene which would be less affected by the inductive effects from the electron withdrawing sulfone or ketone groups.

1.3.2. Functionalization of Triptycene Poly(Ether Ether Ketone) (tripPEEK) for AEMs

From the success with enhancing conductivity in proton exchange membranes due to the enhancements in free volume, the same strategy may benefit the mobility of the larger hydroxide ion. In order to test this hypothesis, functionalization of tripPEEK for AEMs were pursued. The enhanced dispersibility of tripPEEK in organic chlorinated solvents and high boiling polar solvents allow for more applicable chemistries on tripPEEK than its PEEK counterpart. Thus, two synthetic approaches were taken in the attempt to obtain alkaline anion exchange membrane as discussed in the next two sections.

1.3.2.1. Method 1: Through chloromethylation of tripPEEK

Chloromethylation is the most widely used method to functionalize poly aryl ethers for cationic polymers. This method allows for easy control of the degree of functionalization, and cationic polymers can be easily obtained through quaternization amines and phosphines with quantitative yields. Even though this method did not work for tripPEEK as a result of its limited solubility in the reaction conditions, it is mentioned in this thesis for completeness.

Chloromethylation was attempted via two different routes that were used in other poly(aryl ether) polymers (Scheme 1.3-1) in which chloromethyl methyl ether was used as the source of chloromethyl groups in a chloroalkane solvent with tin (IV) chloride or in methanesulfonic acid as the solvent with sulfuric acid as the catalyst.[70] However, in both reactions, tripPEEK precipitates from the reaction within the first 30 mins even at concentrations less than 2 w/v% of tripPEEK. The resultant product was not soluble in any solvents and it was concluded that although tripPEEK could be dispersed well in the reaction solvents,

its solubility is not high enough. Once aggregates in these reactions conditions the chloromethyl group undergoes an electrophilic addition onto another reactive aromatic ring, leading to heavy crosslinking of the polymer.

Scheme 1.3-1. Chloromethylation attempts on tripPEEK. DCM is dichloromethane which was used as the solvent.

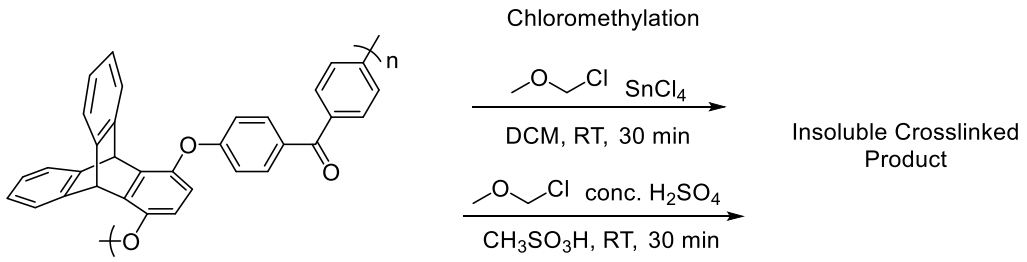

1.3.2.2. Method 2: Through Amine Functionalized tripPEEK

Since guanidinium based AEMs had been found to be stable,[10,62] guanidinium functionalized tripPEEK was targeted via amine functionalized tripPEEK (Scheme 1.3-2). In this scheme, tripPEEK is first nitrated and reduced to form amine functionalized tripPEEK before being converted into guanidinium tripPEEKs.

Scheme 1.3-2. Attempted synthesis of guanidinium tripPEEK AEMs.

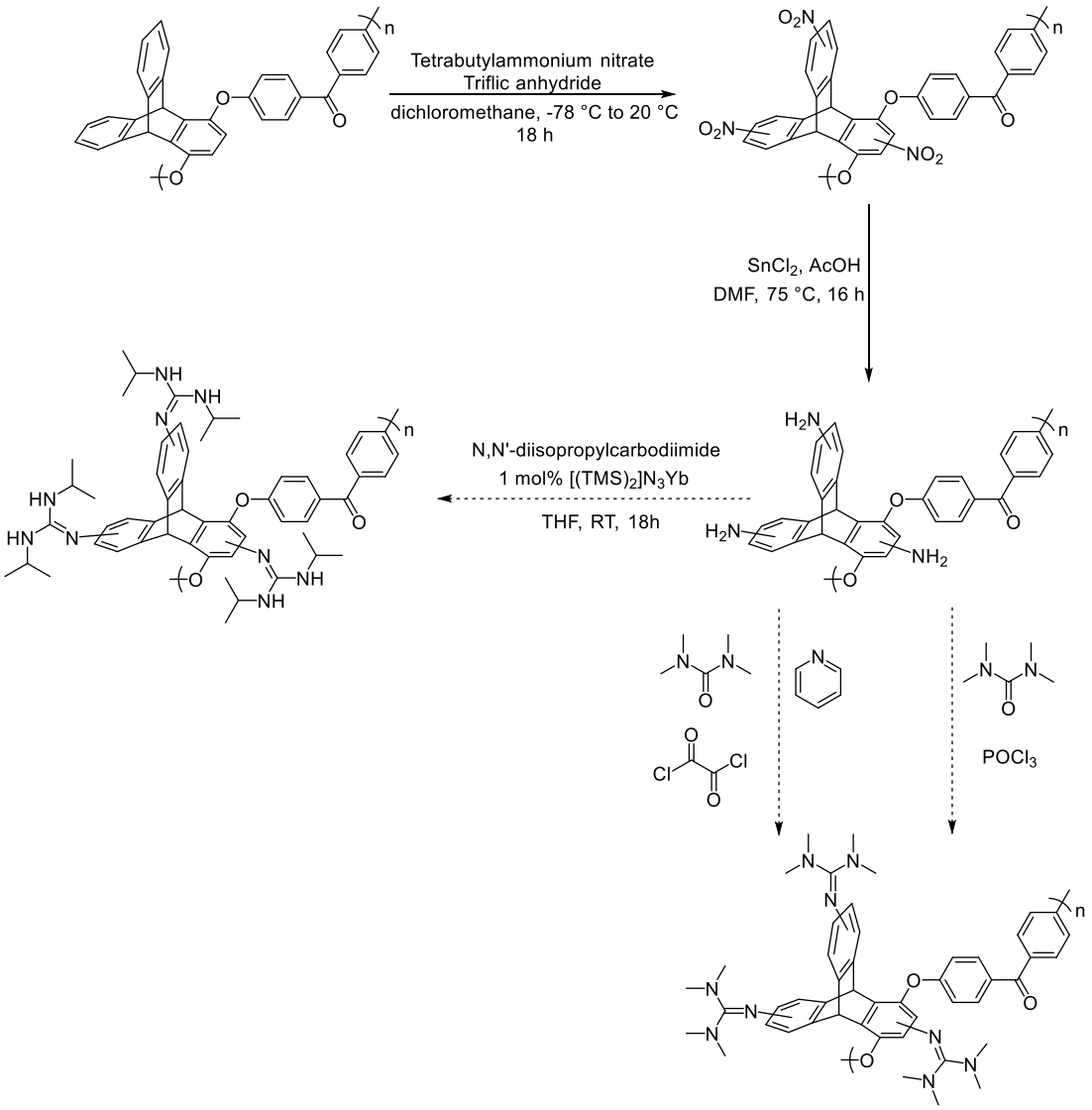

1.3.2.2.1. Nitration reaction

Nitration of PEEK had been achieved using a mixture of concentrated nitric acid and concentrated sulfuric acid as the solvent and reactant.[71] However, it resulted in degradation of the polymer and the final nitrated tripPEEK was only 10 kDa in molecular weight and no longer forms a free standing membrane. As tripPEEK is dispersible in chlorinated solvents, nitration was eventually achieved with an anhydrous condition using triflic anhydride and tetramethylammonium nitrate.[72] The degree of nitration could be easily achieved through controlling the stoichiometry of the reactants.

The addition of nitro-groups to the triptycene moiety is studied using ^{1}H NMR with model compounds (Figure 1.3-3). Since nitration occurs through an electrophilic nitronium cation, the first addition of the nitro group would be on the electron-rich triptycene ring with the ether linkage. Strong electron withdrawing property of the nitro group causes the peak at 5.85 ppm associated to the bridgehead proton to split and shift downfield to 5.89 ppm and 6.06ppm. The bridgehead proton closer to the nitro group would be more deshielded, it is shifted further downfield, causing the split.

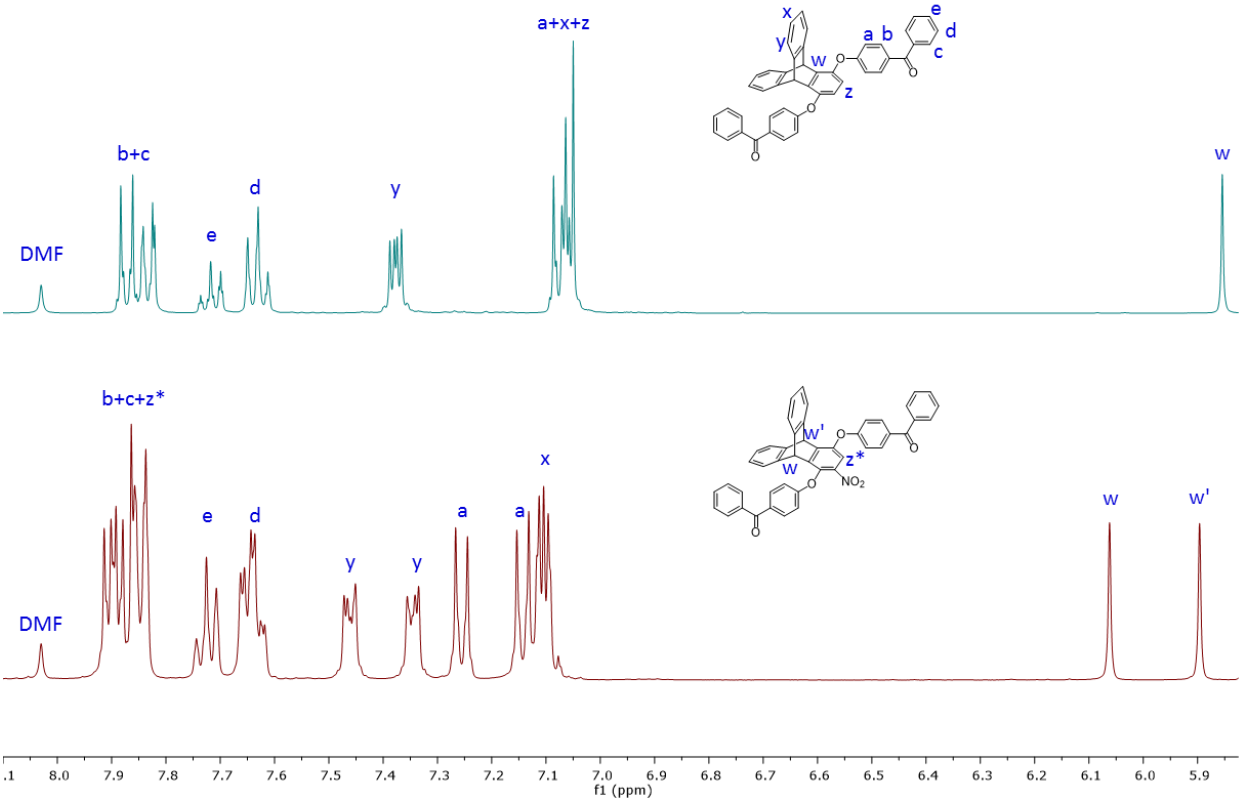

Figure 1.3-3. ^{1}H NMR model compound and model compound with one nitro group (400MHz, DMF-d7, RT). z* is the proton on the carbon beside nitro group.

When the second nitro group was added, the bridgehead proton is now split into four peaks as there are two different resulting configurations (Figure 1.3-4). The nitro groups can be on the same side (Figure 1.3-4(2)) and the collective electron withdrawing effect on one side will result in the larger split of the

bridgehead proton as shown by w_2 and w_2' at 6.39 ppm and 6.17 ppm. On the other hand, when the nitro groups are added on opposite sides (Figure 1.3-4 (1)), the deshielding on the each of the bridgehead proton is less prominent and thus a smaller split as depicted with w_1 and w_1' at 6.34 ppm and 6.23 ppm. The peaks integrate to a total of 2 protons with respect to 24 in the whole molecule. Based on the integration of the peaks, the second addition of the nitro group is slightly favored to be on the opposite side which is a little more electron rich. Thus, the electron withdrawing effect from the first nitro group is directing the second addition which was also observed in other reported nitration of triptycene.[38,73,74]

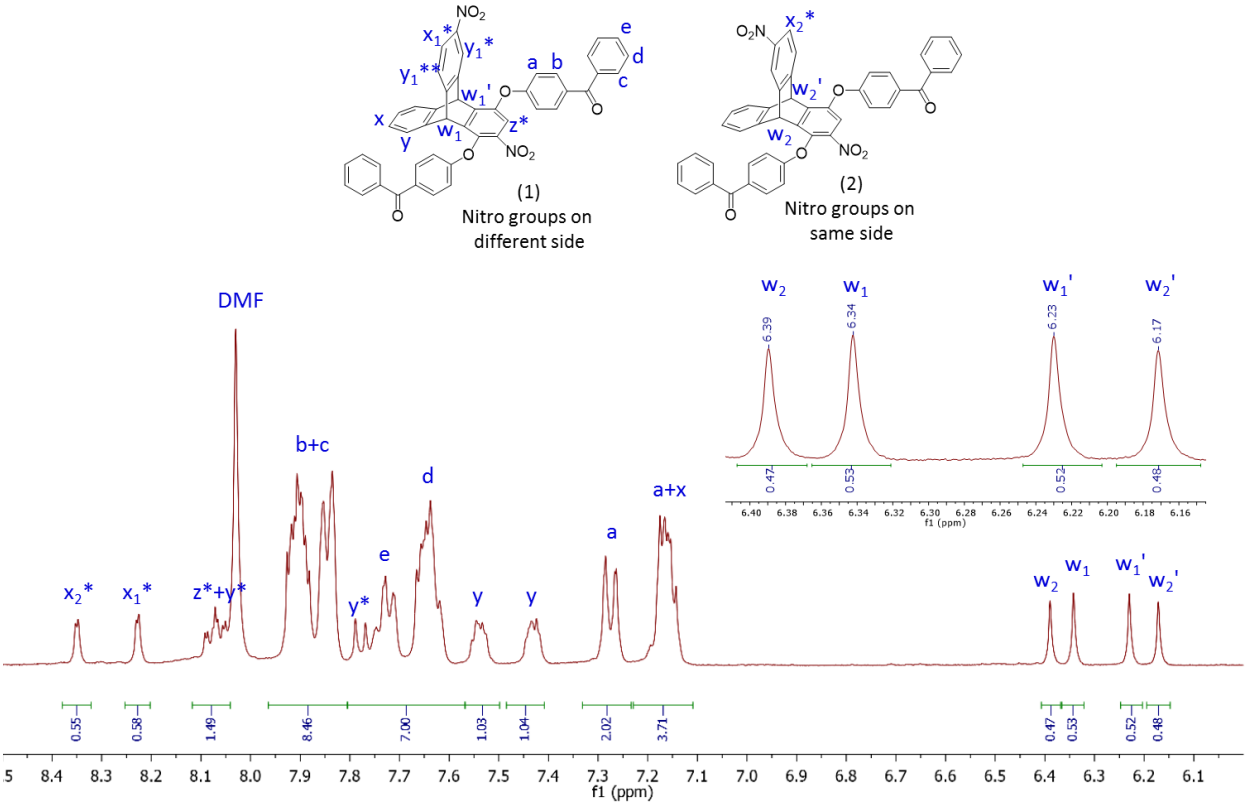

Figure 1.3-4. ^{1}H NMR of the model compound with two nitro groups. Insert within the figure is the zoomed in of the peaks associated to the bridgehead protons.

For the third addition, the total number of resultant configurations would be 8 (3 diastereoisomers, two of which are chiral and racemic). After considering the symmetry of the molecule, the configurations can be grouped into three different groups: (i) opposite sides on the wings and either side on the main chain

(Figure 1.3-5 (1)), (ii) same side on the extended wings and opposite side of the ring on the main chain (Figure 1.3-5 (2)), and (iii) all on the same side on all three wings (Figure 1.3-5 (3)). Thus the bridgehead proton is now split into three sets of two peaks (Figure 1.3-5 insert). Integration of the peaks again shows the directing effect from the electron withdrawing nitro groups. If all additions are equally likely, the split configuration (1), (2) and (3) would be 25%, 50% and 25% respectively. However, the integration of peaks shows that only 20% of the resultant mixture has all three nitro groups on the same side, suggesting once again that the nitro groups are directing the nitration.

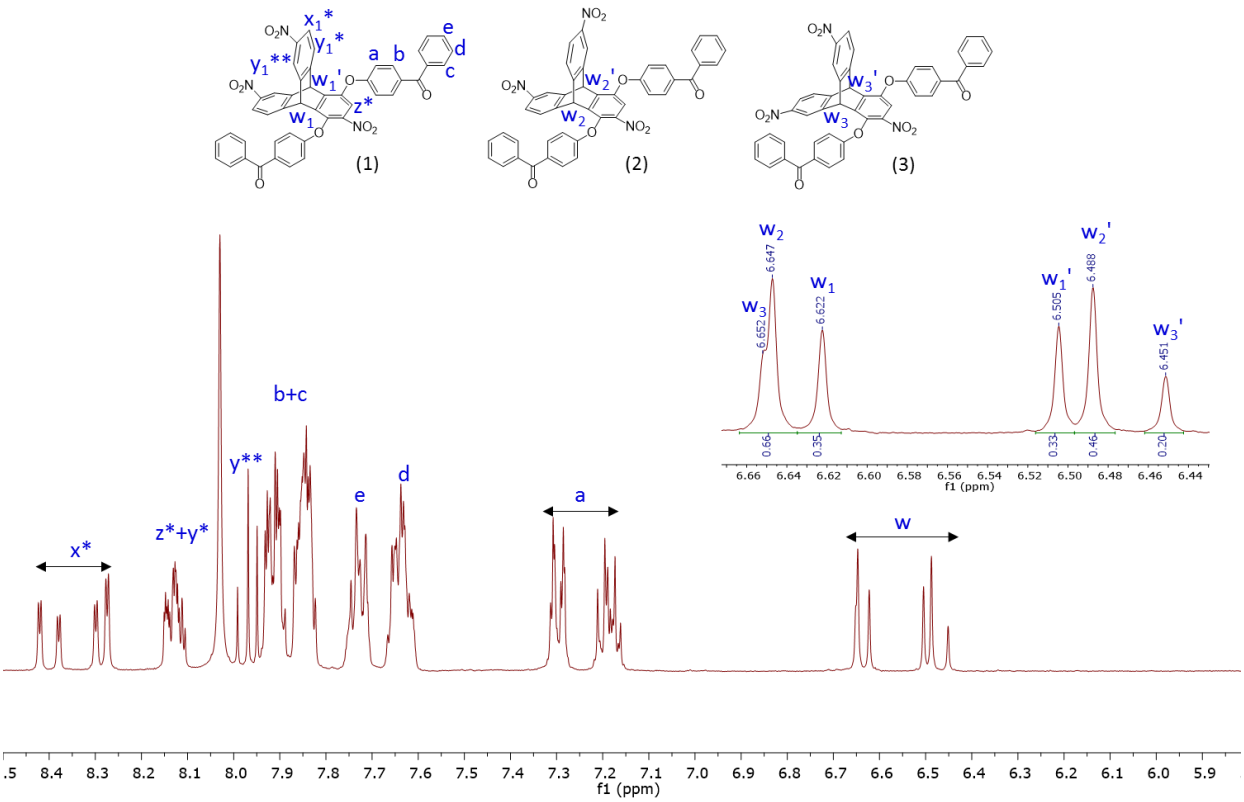

Figure 1.3-5. Proton NMR of the model compound with 3 nitro groups. Insert within the figure is the zoomed in of the peaks associated to the bridgehead protons.

When the nitration conditions were applied to tripPEEK, the NMR can now be compared to estimate the number of nitro groups added to the polymer. (Figure 1.3-6) Even though the polymerization

broadened the NMR peaks, the number of nitro groups added to the polymer can still be estimated from the pattern and position of the bridgehead protons. In this case (Figure 1.3-6), between two and three nitro groups were added to the triptycene moiety in the polymer.

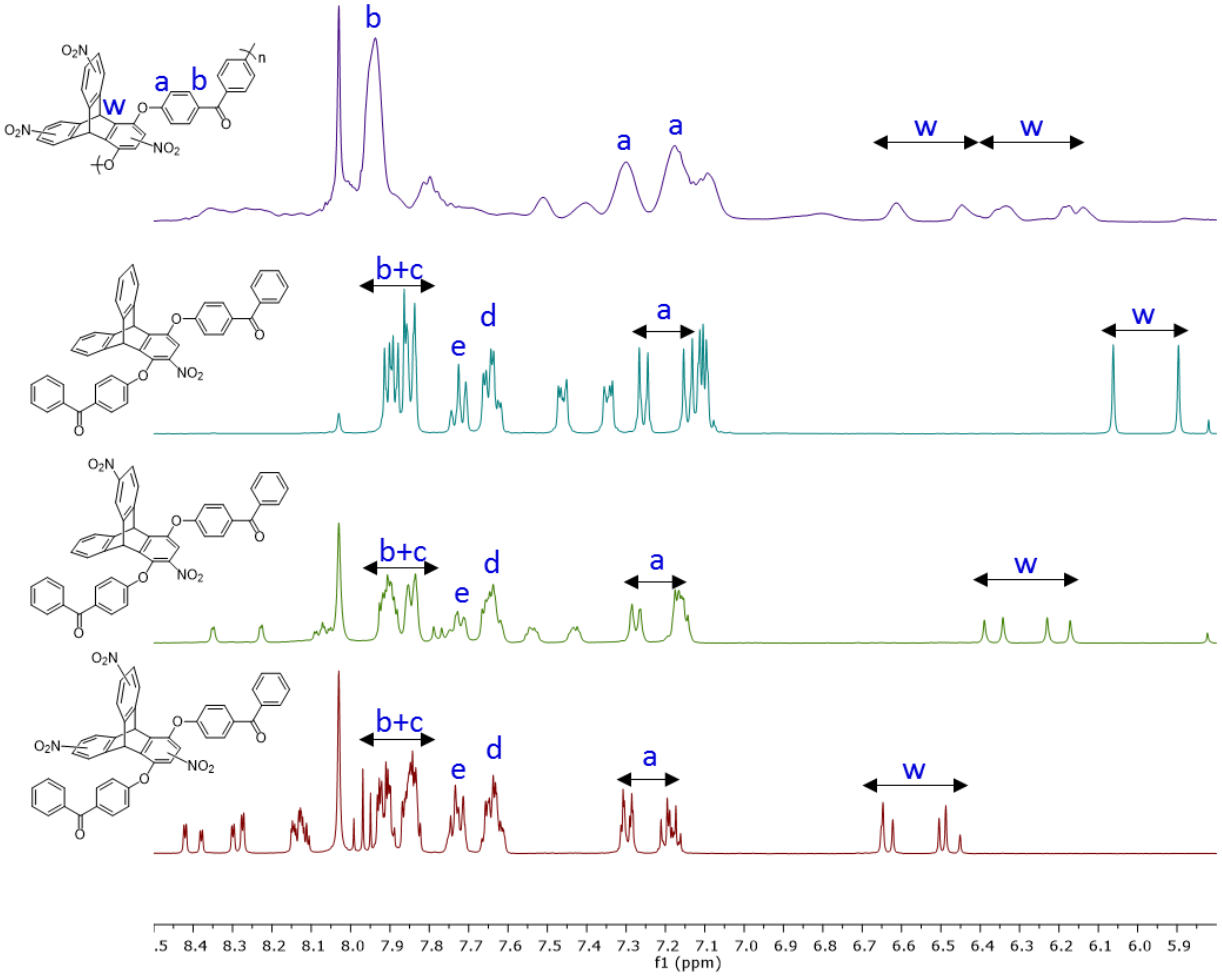

Figure 1.3-6. Overlay of NMR of nitrated tripPEEK and the NMR of the model compounds.

In the attempt to reduce the nitro groups into amines, the polymer was then subjected to reduction conditions such as palladium on carbon with hydrogen or hydrazine, tin (II) chloride with acetic acid or hydrochloric acid. From the IR spectra of the product, (Figure 1.3-7) the nitro groups were successfully reduced as seen in the loss of the 1530 cm^{-1} and 1344 cm^{-1} peaks that are associated to the NO stretch. However, the resultant amine tripPEEK and the model compound are not stable even as the chloride salts;

the compounds and turn black and becomes insoluble after exposure to air for less than 20 mins. The instability of this material is not clear. The amine on the ring containing ether bonds is expected to be most susceptible to oxidation and likely initiates a decomposition sequence.

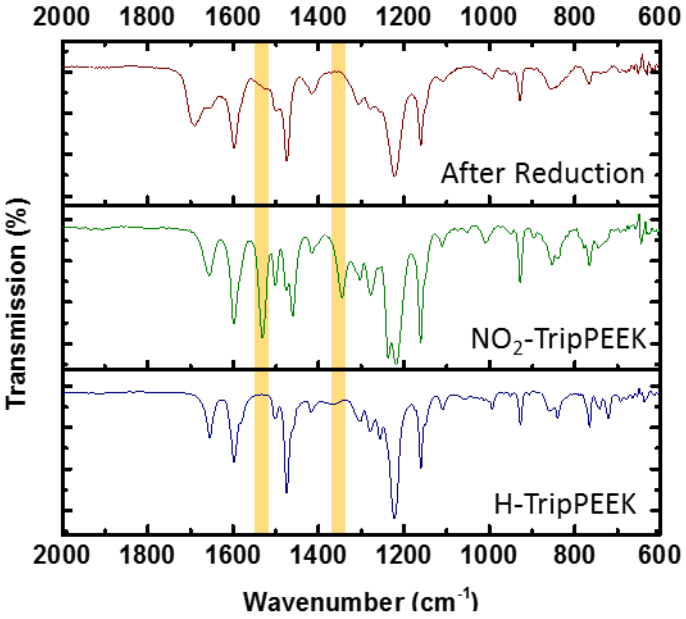

Figure 1.3-7. ATR-FTIR spectra of tripPEEK, NO2-tripPEEK and product after reduction.

1.3.2.3. Conclusion

In the attempts to obtain an alkaline anion exchange membrane with tripPEEK, has been thwarted by a combination of solubility and reactivity issues. Although tripPEEK has been shown to be well dispersed in chlorinated solvents, it appeared insufficient to avoid crosslinking under the chloromethylation reaction conditions. We conducted successful nitration and reduction reactions to produce what is presumed to be a tripPEEK-Polyamine, however the produce proved to be unstable in ambient conditions.

1.3.3. Functionalized Triptycene Poly(Ether Sulfone) as Alkaline Anion Exchange Membrane

In order to get a working alkaline anion exchange membrane (AAEM), functionalized triptycene poly(ether sulfone) was chosen for its good solubility in chlorinated solvents and high boiling polar solvents.

TripPES were functionalized for AAEMs through quaternization of chloromethylated tripPES. (Scheme 1.3-3)

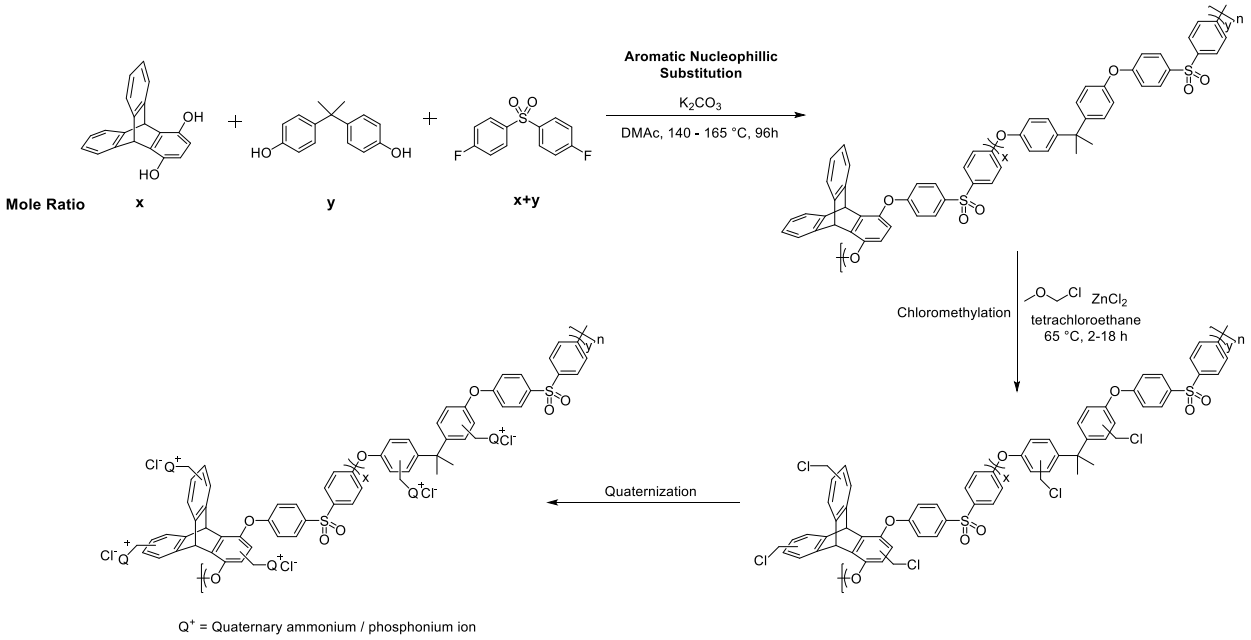

Scheme 1.3-3. Synthesis of quaternary tripPES for anion exchange membrane.

1.3.3.1. Synthesis of Anion Exchange Membranes

1.3.3.1.1. Synthesis of Triptycene Poly(Ether Sulfone) (tripPES(x,y)):

TripPES and its copolymers, designated tripPES(x,y) (Table 1.3-1), were synthesized through aromatic nucleophilic substitution (S_NAr) reaction between x equivalents of triptycene hydroquinone, y equivalents of bisphenol A, and (x+y) equivalents of bis (4-fluorophenyl) sulfone (Scheme 1.3-4). The general procedure of polymerization, illustrated using tripPES(1,1), is as follows: In a flamed dried two-necked round bottom flask under nitrogen atmosphere with a Dean-Stark apparatus, triptycene hydroquinone (2.863 g, 10.0 mmol), bisphenol A (2.283 g, 10.0 mmol) and bis (4-fluorophenyl) sulfone (5.085 g, 20.0 mmol) was dissolved in anhydrous DMAc (60 ml) and anhydrous toluene (10 ml). Potassium carbonate (12.715 g, 23.0 mmol) was added and the reaction was heated to 140 °C for azeotropic distillation to remove water that was generated in the reaction. Once all the toluene was collected the reaction stirred at 140 °C for 48 hours before heated to 165 °C (reflux) for another 18 hours. The reaction was then

precipitated in boiling water and filtered. The resulting polymer was purified by dissolving in DMAc and precipitating twice in boiling water and twice in methanol, yielding an off-white polymer powder that was dried in the vacuum oven for two days at 75 °C.

Scheme 1.3-4. Polymerization of TripPES(x,y) through SNAr reaction

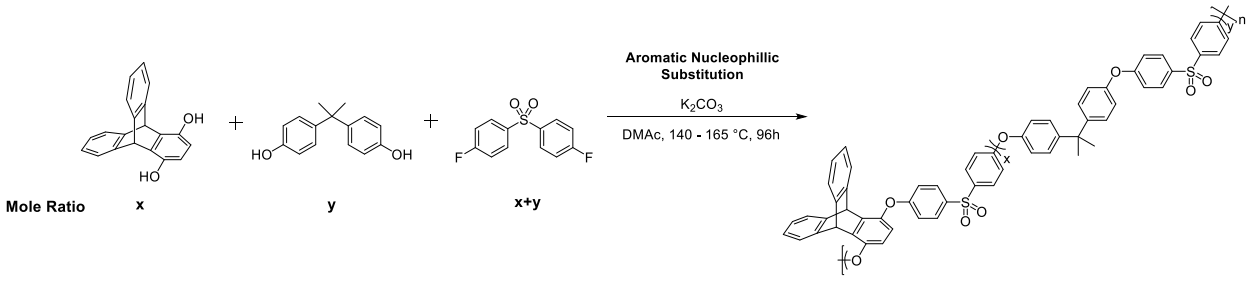

Table 1.3-1. Mole ratio of monomers of polymers. Average molecular weight per repeat unit is calculated in equation below. Sulfone deactivation prevents reaction at the attached rings.

Designation	Mole ratio			Average molecular weight per repeat unit (g/mol)	No. of active phenyl rings for functionalization per repeat unit
	triptycene hydroquinone (x)	bisphenol A (y)	bis (4-fluorophenyl) sulfone (x+y)		
tripPES(1,0)	1	0	1	500.57	3.0
tripPES(1,1)	1	1	2	471.55	2.5
tripPES(1,9)	1	9	10	448.33	2.1
PES	0	1	1	442.53	2.0

$$\text{Ave. Molecular Weight per repeat unit} = \frac{x(500.57) + y(442.53)}{x + y}$$

1.3.3.1.2. Synthesis of chloromethylated tripPES (Cl-tripPES) and chloromethylated PES (Cl-PES):

TripPES and PES were chloromethylated using chloromethyl methyl ether with zinc (II) chloride as reported.[75] (Scheme 1.3-5) The equivalence of reactants were with respect to every active phenyl rings per repeat unit in the polymer (Table 1.3-1). In a flamed dried flask under nitrogen, polymers were dissolved in 1,1,2,2-tetrachloroethane at a concentration of 3 w/v%. Concentration of the polymer needs to be kept low to prevent crosslinking of the polymer. Chloromethyl methyl ether was added to the reaction and mixed homogenously before zinc (II) chloride was added. The reaction was then heated to 60 °C for stirred for 1 hour. The product was precipitated in methanol and filtered, yielding a white polymer that had 95 % of the

active aromatic rings in the polymer functionalized. The degree of chloromethylation can be reduced by reducing the reaction time or temperature.

Scheme 1.3-5. Chloromethylation of tripPES. Equivalence of the reactants are with respect to the each reactive phenyl group in the polymer.

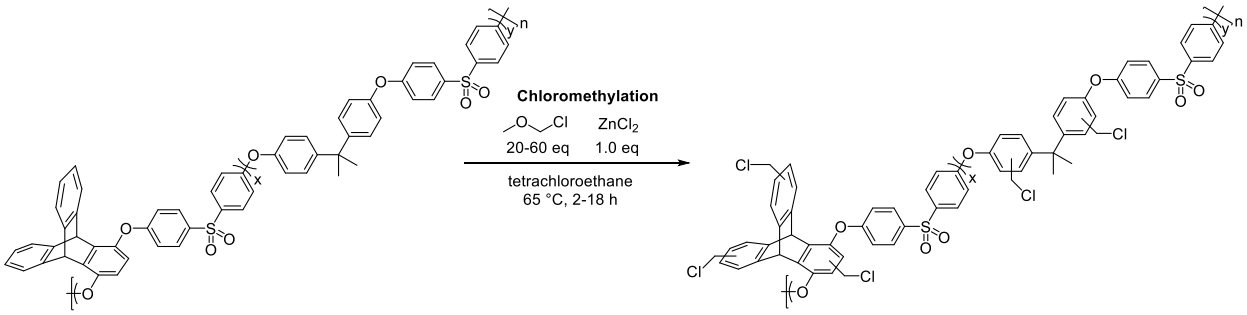

1.3.3.1.3. Synthesis of 1-methylimidazolium tripPES with chloride anion (Cl-MeIm-TripPES)

1-methylimidazolium tripPES with chloride anions (Cl-MeIm-tripPES) was made via quaternization of Cl-tripPES with 1-methylimidazole (Scheme 1.3-6). Cl-tripPES or Cl-PES were dissolved in a 1-methyl-3-pyrrolidinone 10 w/v % solution and 1-methylimidazole was added in excess and left to stir at room temperature for 18 hours. The reaction was then precipitated in acetone, filtered and wash with acetone. The filtrate was dried in a vacuum oven overnight at 70 °C to yield an off white polymer of Cl-MeIm-tripPES.

Scheme 1.3-6. Synthesis of Cl-MeIm-tripPES.

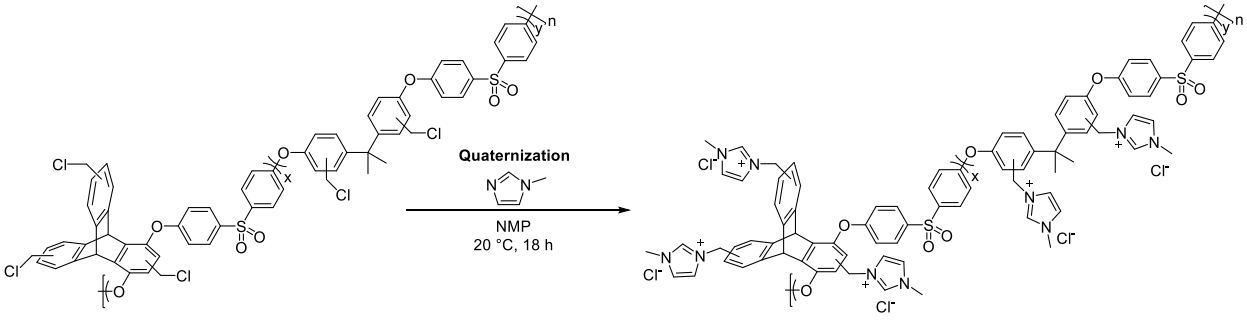

1.3.3.1.4. Formation of Alkaline Anion Exchange Membrane (AAEM)

Cl-MeIm-trpPESs with 10 wt% BPA-PES as binder were dissolved to form 10 wt% solutions in N-methyl-2-pyrrolidone (NMP). 2.0 ml of the polymer solution was dispensed on a 75 mm × 25 mm glass slide in a vacuum oven and placed under vacuum at room temperature for 6 hours to degas the solutions. The vacuum oven was then heated to 70 °C under vacuum for 4 hours to remove the solvent by slow evaporation before heating to 150 °C for 8 hours to completely dry out the membranes. Membranes were soaked in 2.0 M NaOH, changing the soaking solution at least 3 times. This exchanges the chloride ions with hydroxide ions, forming the AAEM with hydroxide loaded MeIm-trpPES (OH-MeIm-trpPES). Free standing membranes with thicknesses between 100-150 µm then cut to sizes needed for further experiments.

1.3.3.2. Characterization of Membranes

1.3.3.2.1. Ion exchange capacity:

IEC was determined by a back titration method with 0.01 M sodium hydroxide solution to prevent errors that can occur from the reaction of free hydroxide ions with carbon dioxide in the air. The membranes were first soaked in 2.0 M sodium hydroxide solution for 24 hours, rinsed with deionized water and soak in deionized water for another 24 hours to ensure that all the mobile ions in the membrane are hydroxide ions. The membranes were then transfer into 20 ml (V_{HCl}) of 0.10 M hydrochloric acid (M_{HCl}) for exchange the hydroxide ions with chloride ions. The acid was then titrated with 0.01 M (M_{NaOH}) sodium hydroxide solution (standardized with 0.010 M potassium hydrogen phthalate) until pH 7.0 using a pH meter and the volume of base (V_{NaOH}) was used to calculate amount of acid that was neutralized by the hydroxide ions (n_{OH^-}) in the membrane which was then used to determine IEC with equation below, where m_{dry} is the mass of dried membrane.

$$\mathrm{IEC} = \frac{n_{OH^-}}{m_{dry}} = \frac{(V_{HCl})(M_{HCl}) - (V_{NaOH})(M_{NaOH})}{m_{dry}}$$

1.3.3.2.2. Water Uptake (WU)

Water uptake is the measure of the amount of water in the membranes when swollen in water. Membranes with hydroxide counter ions were soaked in water for at least 24 hours to equilibrate. They were then taken out of water and quickly dabbed with Kimwipes to remove surface excess water and weighed. The mass of the hydrated membrane (m_{wet}) was then used to calculate water uptake using the equation below.

$$WU = \frac{m_{wet} - m_{dry}}{m_{dry}} \times 100\%$$

1.3.3.2.3. Anion conductivity measurements:

Anion conductivity (σ) at various humidity and temperature was obtained through electrochemical impedance spectroscopy (EIS) using electrochemical interface (Solartron 1287) with an impedance analyzer (Solartron 1260). Films were placed across 2 platinum electrodes spaced 3 cm apart and the setup is placed in a water bath placed in an oven. Measurements were taken over the temperature range of 20 – 90 °C with a mean AC voltage 0 V and an amplitude of 0.1 V over a frequency range of 1MHz to 0.1 MHz. The resultant Nyquist plot was modeled with equivalent circuit model (Figure 1.3-8) where $R_{contact}$ is the contact resistance, R_{mem} is the bulk resistance of the membrane, C_{mem} is the capacitance in the membrane and W is a Warburg element that is attributed to the diffusion limited charge accumulation at the electrode. Anion conductivity (σ) was then calculated using equation below where *l* is the length between the electrodes, *w* is the width of the membrane and *t* is the thickness of the membrane. All dimensions were measured at 20 °C after soaking the membranes in water for 24 hours. Activation energy was calculated based on an Arrhenius relation.

$$\sigma = \frac{l}{(R_{mem})(t)(w)}$$

$$\sigma = Ae^{-\left(\frac{E_a}{RT}\right)}$$

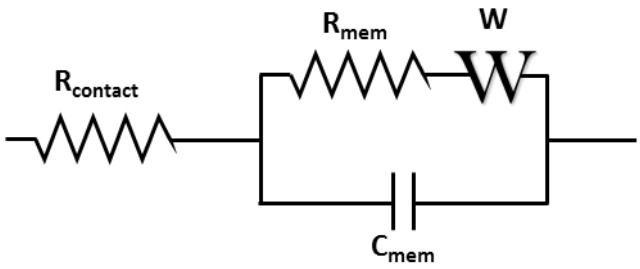

Figure 1.3-8. Equivalent circuit model used to fit the Nyquist plots

1.3.3.3. Results and Discussion

1.3.3.3.1. Brittleness of Functionalized tripPES

Mechanical properties of the functionalized membranes are important as they are the structural part of the membrane electrode assembly in the fuel cell. One of the properties that can be used to determine the mechanical stability of the membrane is its glass transition temperature. Comparing the DSC thermograms of all tripPES (Figure 1.3-9), copolymers of tripPES exhibits a single glass transition temperature suggesting that the copolymers are random copolymers. Glass transition temperatures of tripPES increase from 200 °C to 280 °C with increasing number of triptycene group, as a bulky triptycene unit hinders chain rotation in the polymer. As the glass transition temperatures are high, these polymers are glassy and brittle at room temperature. TripPES(1,0) would crack when dried from solution. Since further functionalization would only increase the steric bulk on the triptycene wings, functionalized membranes all cracked when cast from solution. To circumvent that, unfunctionalized PES was added to functionalized tripPES membranes as a binder at different ratios to form stable membranes for testing.

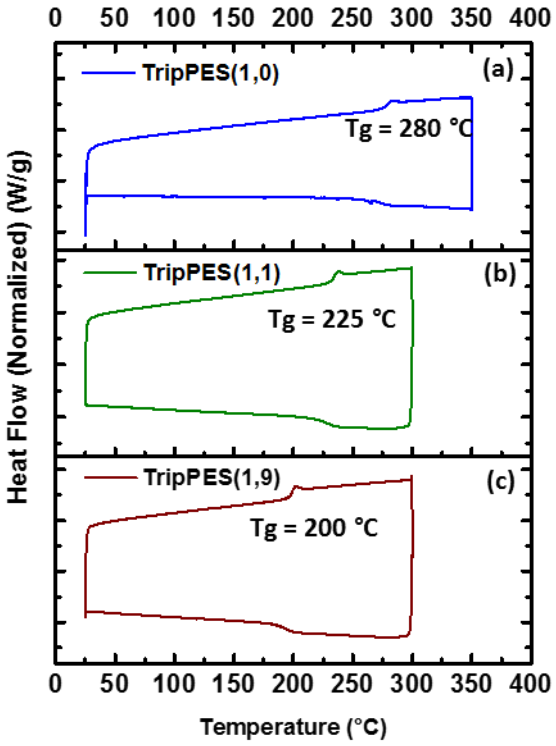

Figure 1.3-9. DSC thermograms of (a) tripPES(1,0), (b) tripPES(1,1) and (c) tripPES(1,9). Heat flows are measured from 25 °C to 350 °C at a heating and cooling rate of 10 °C/min.

1.3.3.3.2. Structure characterization of Cl-MeIm-tripPES

Chloromethylation and quaternization of tripPES was successful as confirmed by that analysis of the ^{1}H NMR data (Figure 1.3-10). Chloromethylation produced new peaks at 4.54 ppm and at 4.40 ppm which correspond to the methylene bridge between the chlorine and the phenyl rings. The peak from the chloromethyl group that is attached on phenyl ring with the ether linkages is shifted upfield to 4.40 ppm as a result of the electron donating ether linkages.

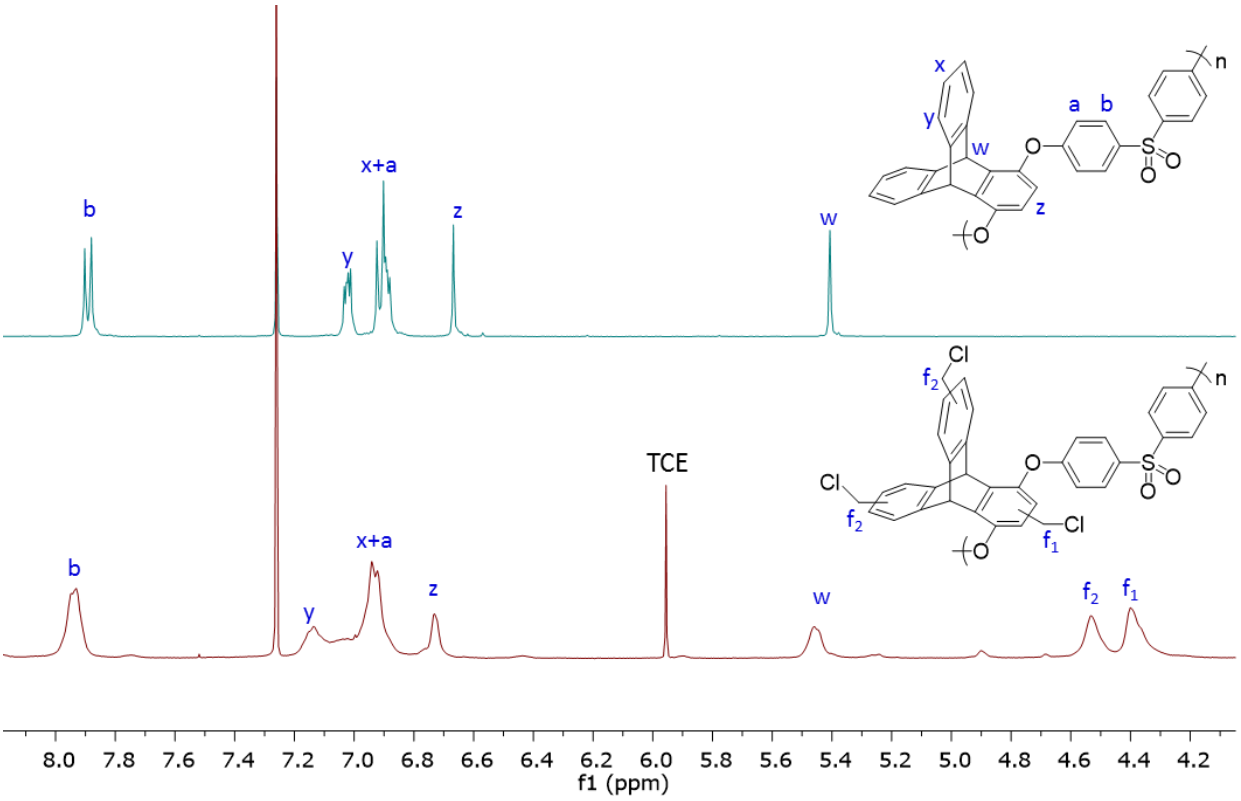

Figure 1.3-10. ^{1}H NMR of Cl-tripPES(1,0). Spectrum is taken at 400 MHz with $CDCl_3$ as solvent. TCE is tetrachloroethane that was used as the solvent in the chloromethylation step.

Upon quaternization with 1-methyl imidazole, the methylene bridge is shifted to 5.39 ppm due to the deshielding from the positively charged imidazolium group. (Figure 1.3-11) A new peak at 9.49 ppm from the proton on C2 position in the imidazolium functional group (g in Figure 1.3-11) is diagnostic of the formation of the quaternized methyl imidazolium ion. The residual peak at 4.63 ppm suggest that there might have been some crosslinking that occurred in the chloromethyl step.

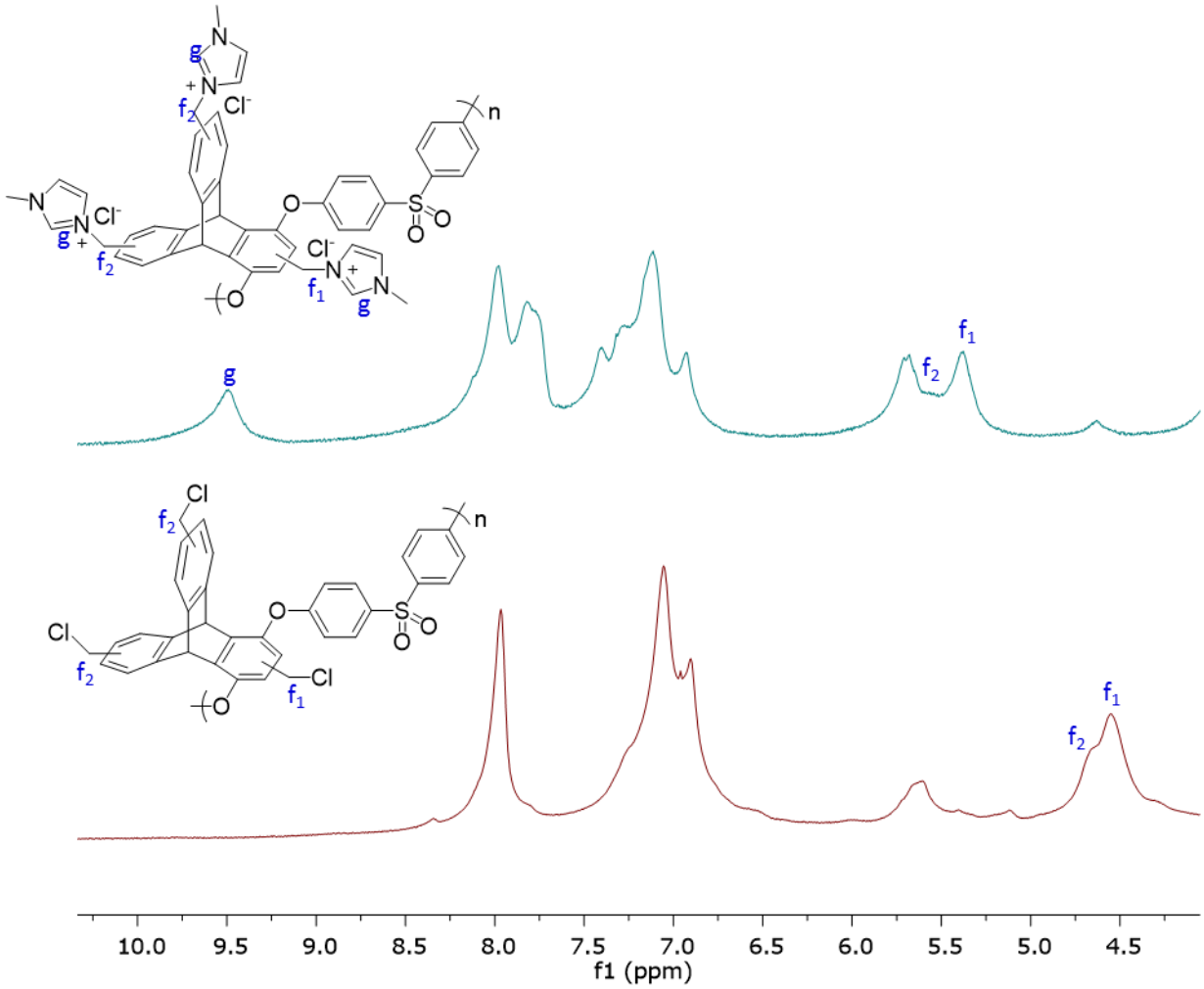

Figure 1.3-11. ^{1}H NMR of Cl-MeIm-trpPES(1,0) and Cl-tripPES(1,0). Spectrum is taken at 400 MHz with DMSO-d6 as solvent.

1.3.3.3.3. Physical Properties of Cl-MeIm-TripPES membranes

Thermogravimetric analysis shows that the decomposition of the polymers at various stage of functionalization (Figure 1.3-12). Initial mass loss observed at 150 °C for Cl-tripPES is due to residual tetrachloroethane from the reaction and initial mass loss observed between 50 and 100 °C with Cl-MeIm-tripPES is the result of water that is adsorbed on the ionic polymer. The unfunctionalized tripPES decomposes at 500 °C, while the chloromethyl and imidazolium functional groups decomposes at 400 °C and 200 °C respectively. These temperatures are within the operating range of AAEMFC of up to 200 °C.

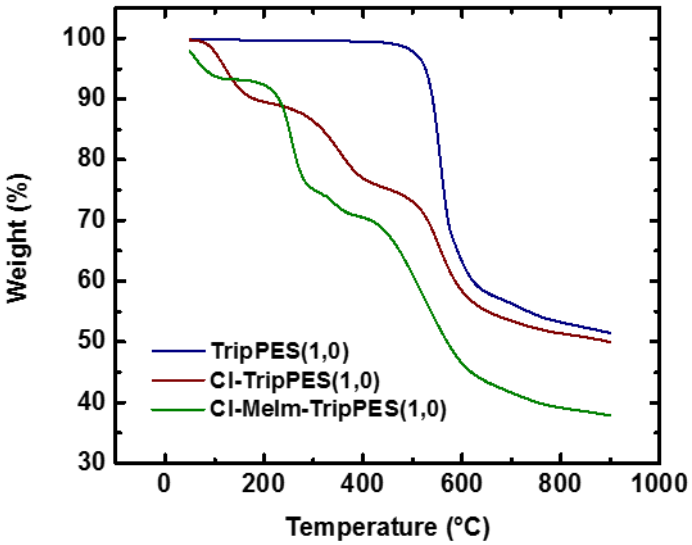

Figure 1.3-12. Thermogravimetric analysis of tripPES and functionalized tripPES. Samples were heated from 50 °C to 900 °C at a heating rate of 10 °C/min.

Membranes with different amount of binders were made to find the optimal binder concentration to form free standing membranes. Unfortunately, membranes of Cl-MeIm-trpPES(1,0) that are more than 50% functionalized, cracked upon drying even with 50 wt% binder concentration. Thus the final membranes used for the rest of this Chapter were made with MeIm-trpPES(1,1) with 10 wt% of trip-PES(1,9) as binder.

1.3.3.3.4. Alkaline Anion Conductivity of OH-MeIm-tripPES(1,1) Membranes

Membranes of OH-MeIm-tripPES(1,1) at various degree of functionalization with 10 wt% binder were made and tested for alkaline anion conductivity in deionized water (Figure 1.3-13). First and foremost, high alkaline conductivity of 108 mS/cm at 80 °C in water was achieved with membrane with 72% degree of functionalization. Since alkaline conductivities above 100 mS/cm are required for more efficient fuel cells,[6,7] tripPES is a great candidate for further improvements and optimization for AAEMFCs.

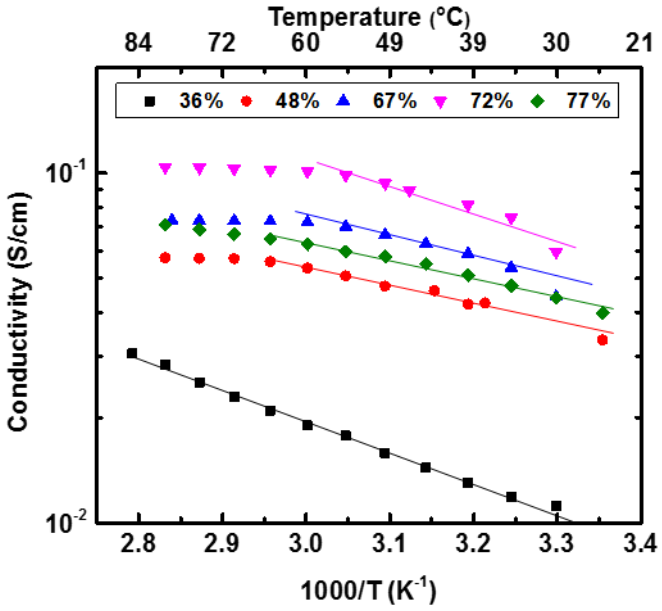

Figure 1.3-13. Alkaline anion conductivity of OH-MeIm-tripPES(1,1) membranes with 10 wt% binder. Degree of functionalization is defined as the percentage of the active phenyl rings on in the polymer that were functionalized. (Table 6) Straight line in this plots represents an Arrhenius behavior in conductivity and serve as a guide to show deviation caused due to swelling.

Secondly, anion conductivity increases with degree of functionalization up to 72% and decreased at 77%. (Figure 1.3-13) This is likely the result of swelling of the membranes at high degree of functionalization, resulting in dilution of methylimidazolium groups in the membrane. With a higher degree of functionalization, the membranes become increasingly more hydrophilic and thus swell more in water. This effect is further aggravated at higher temperatures as a result of increasing solubility of the membranes in water. Closer inspection on the conductivity plots shows that membranes with above 48% functionalization show a deviation of the conductivity from an Arrhenius relation with temperature, suggesting that the conductivity above 60 °C are lower than expected because of membrane swelling. Thus, swelling of the membrane needs to be controlled in order to achieve better conductivity.

Small angle x-ray scattering (SAXS) on the hydrated samples was done in order to identify the reason for the high ion conductivity. (Figure 1.3-14) Nanophase separation with a d-spacing of around 5 nm were observed within the membranes. The nanophase separation is likely caused by phase separation

between the hydrophilic imidazolium group and the hydrophobic polyaryl ether backbone. Increased phase separation has been reportedly in many other polyether and block copolymer systems as a design parameter to improve ion conductivity.[8,46,76,77] In the case of 67% and 77% functionalized tripPES(1,1) membranes, the lack of phase separation even though they have high degrees of functionalization is a concern. One possible reason is that during chloromethylation, there is an uncontrolled amount of crosslinking that occured in the membrane and varies in each experiment. A small amount of crosslinking would hinder aggregation of hydrophilic groups within the membrane and could be the reason for the lack of phase separation observed.

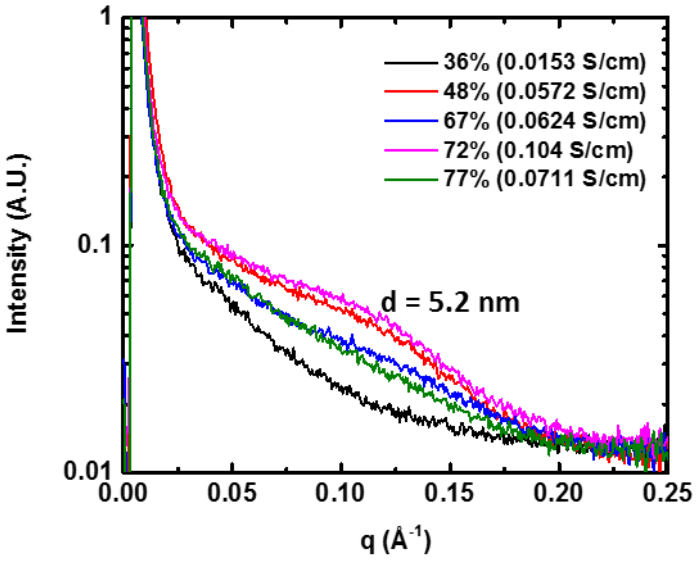

Figure 1.3-14. SAXS data for OH-MeIm-trpPES membranes.

The nanophase separation observed in OH-MeIm-tripPES is possibly related to the triptycene moiety. SAXS data of OH-MeIm-BPA-PES was compared with OH-MeIm-tripPES(1,1) with both membranes having around 70% functionalization (Figure 1.3-15). Triptycene groups in the base polymer allow for nanophase separated domains to become larger and contain more water for ion conduction. However, the membranes do have different composition as the OH-MeIm-tripPES(1,1) contains a binder. More control study needs to be done to confirm this finding.

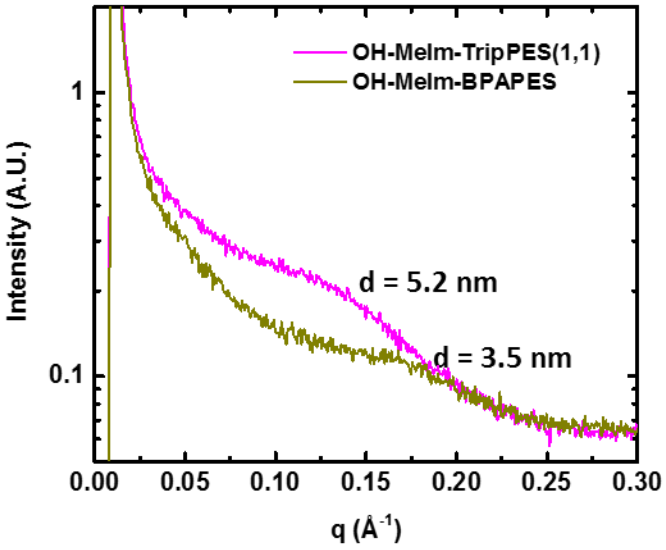

Figure 1.3-15. SAXS data of OH-MeIm-TripPES(1,1) and OH-MeIm-BPAPES with similar degree of functionalization.

The stability of the membranes were then tested by soaking the membranes in 2.0 M sodium hydroxide solutions at an elevated temperature of 80 °C for two weeks. Membranes above 80% functionalization dissolved and dissociated after two weeks. Membranes that were presented in the previous section lost imidazolium groups. This is possibly due to degradation of the imidazolium rings by hydroxide reaction on the CH group between the nitrogens. Substitution on this position is known to increase stability.[7,65,78] Thus, OH-MeIm-tripPES membranes are only stable at low degree of functionalization. The only membrane that retained hydroxide conductivity after the stability test was a 26% functionalized OH-MeIm-tripPES(1,0) membrane (Figure 1.3-16). It is likely that at such low degree of functionalization, the membrane is extremely hydrophobic and thus reduces the access of hydroxide ions to the imidazolium cation and hence prevented the degradation.[65] However, it is not certain why it shows a better conductivity after the test.

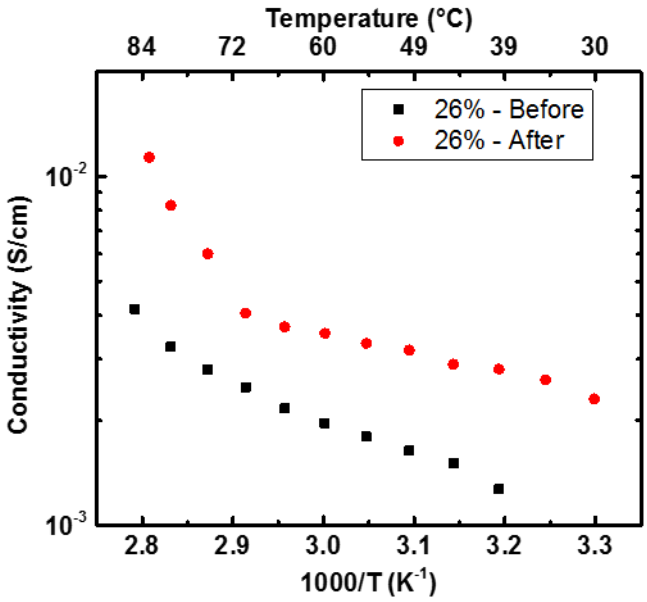

Figure 1.3-16. Ion conductivity of OH-MeIm-tripPES membrane of low degree of functionalization.

1.3.4. Conclusion and Future Direction

Triptycene based poly(aryl ether)s have been shown to produce alkaline anion membranes with ion conductivities of 104 mS/cm at 80 °C in water. High conductivities are possibly due to the nanophase separation observed in the membranes and the triptycene moiety can contribute to the increase in domain sizes. However, the membranes are not stable to basic conditions in the operation of a fuel cell. Furthermore, tripPES membranes studied in this work were made with a binder which might also have contributed to the nanophase separation observed. To further evaluate the improvements that can be attributed to the triptycene moiety, single component membranes need to be made. A strong candidate would be a fluorinated polyarylether with the triptycene moiety. (Figure 1.3-17) The removal of the sulfone linkage reduces the stiffness in the polymer and would probably result in polymers that are less brittle. Furthermore, fluorine groups increases the hydrophobicity of the polymer backbone and would thus encourage nanophase separation which would possibly improve the ion conductivity of the membrane.

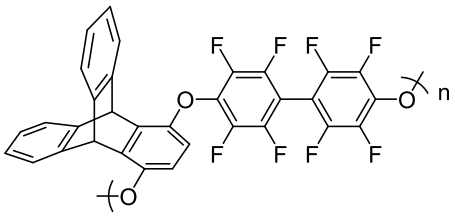

Figure 1.3-17. Possible triptycene polyaryl ether for alkaline anion exchange membrane.

1.4. References

(1) Grove, W. R. On Voltaic Series and the Combination of Gases by Platinum. Philos. Mag. Third Ser. 1839, 14, 127–130.

(2) Grove, W. R. On a Gaseous Voltaic Battery. Philos. Mag. J. Sci. - Third Ser. 1842, 21, 417–420.

(3) Couture, G.; Alaaeddine, A.; Boschet, F.; Ameduri, B. Polymeric Materials as Anion-Exchange Membranes for Alkaline Fuel Cells. Prog. Polym. Sci. 2011, 36 (11), 1521–1557.

(4) Steele, B. C.; Heinzel, A. Materials for Fuel-Cell Technologies. Nature 2001, 414 (6861), 345–352.

(5) Yuan, X.-Z.; Song, C.; Wang, H.; Zhang, J. PEM Fuel Cells and Their Related Electrochemical Fundamentals. In Electrochemical Impedance Spectroscopy in PEM Fuel Cells; Springer London: London, 2010; pp 1–37.

(6) Houchins, C.; Kleen, G. J.; Spendelow, J. S.; Kopasz, J.; Peterson, D.; Garland, N. L.; Ho, D. L.; Marcinkoski, J.; Martin, K. E.; Tyler, R.; et al. U.S. DOE Progress Towards Developing Low-Cost, High Performance, Durable Polymer Electrolyte Membranes for Fuel Cell Applications. Membranes (Basel). 2012, 2 (4), 855–878.

(7) Varcoe, J. R.; Atanassov, P.; Dekel, D. R.; Herring, A. M.; Hickner, M. a.; Kohl, P. A.; Kucernak, A. R.; Mustain, W. E.; Nijmeijer, K.; Scott, K.; et al. Anion-Exchange Membranes in Electrochemical Energy Systems. Energy Environ. Sci. 2014, 7 (10), 3135–3191.

(8) Hickner, M. A.; Herring, A. M.; Coughlin, E. B. Anion Exchange Membranes: Current Status and Moving Forward; 2013; Vol. 51, pp 1727–1735.

(9) Wang, Y.; Chen, K. S.; Mishler, J.; Cho, S. C.; Adroher, X. C. A Review of Polymer Electrolyte Membrane Fuel Cells: Technology, Applications, and Needs on Fundamental Research. Appl. Energy 2011, 88 (4), 981–1007.

(10) Ran, J.; Wu, L.; He, Y.; Yang, Z.; Wang, Y.; Jiang, C.; Ge, L.; Bakangura, E.; Xu, T. Ion Exchange Membranes: New Developments and Applications. J. Memb. Sci. 2017, 522, 267–291.

(11) Hickner, M. a.; Ghassemi, H.; Kim, Y. S.; Einsla, B. R.; McGrath, J. E. Alternative Polymer Systems for Proton Exchange Membranes (PEMs). Chem. Rev. 2004, 104 (10), 4587–4611.

(12) Zhang, Y.; Li, J.; Ma, L.; Cai, W.; Cheng, H. Recent Developments on Alternative Proton Exchange Membranes: Strategies for Systematic Performance Improvement. Energy Technol. 2015, 3 (7), 675–691.

(13) Park, C. H.; Lee, C. H.; Guiver, M. D.; Lee, Y. M. Sulfonated Hydrocarbon Membranes for Medium-Temperature and Low-Humidity Proton Exchange Membrane Fuel Cells (PEMFCs). Prog. Polym. Sci. 2011, 36 (11), 1443–1498.

(14) Li, Q.; Jensen, J. O.; Savinell, R. F.; Bjerrum, N. J. High Temperature Proton Exchange Membranes Based on Polybenzimidazoles for Fuel Cells. Prog. Polym. Sci. 2009, 34 (5), 449–477.

(15) Fang, J.; Guo, X. Phosphoric Acid-Doped Polybenzimidazole Membranes for High-Temperature Proton Exchange Membrane Fuel Cells. In Electrochemical Polymer Electrolyte Membranes; Fang, J., Qiao, J., Wilkinson, D. P., Zhang, J., Eds.; Electrochemical Energy Storage and Conversion; CRC Press, 2015; pp 315–364.

(16) Peighambardoust, S. J.; Rowshanzamir, S.; Amjadi, M. Review of the Proton Exchange Membranes for Fuel Cell Applications. Int. J. Hydrogen Energy 2010, 35 (17), 9349–9384.

(17) Araya, S. S.; Zhou, F.; Liso, V.; Sahlin, S. L.; Vang, J. R.; Thomas, S.; Gao, X.; Jeppesen, C.; Kær, S. K. A Comprehensive Review of PBI-Based High Temperature PEM Fuel Cells. Int. J. Hydrogen Energy 2016, 41 (46), 21310–21344.

(18) Rosli, R. E.; Sulong, A. B.; Daud, W. R. W.; Zulkifley, M. A.; Husaini, T.; Rosli, M. I.; Majlan, E. H.; Haque, M. A. A Review of High-Temperature Proton Exchange Membrane Fuel Cell (HT-PEMFC) System. Int. J. Hydrogen Energy 2016.

(19) Yi, S.; Zhang, F.; Li, W.; Huang, C.; Zhang, H.; Pan, M. Anhydrous Elevated-Temperature Polymer Electrolyte Membranes Based on Ionic Liquids. J. Memb. Sci. 2011, 366 (1–2), 349–355.

(20) Peckham, T. J.; Schmeisser, J.; Rodgers, M.; Holdcroft, S.; Horsfall, J.; Lovell, K. V.; Kreuer, K. D.; Maier, J.; Ding, J. F. Main-Chain, Statistically Sulfonated Proton Exchange Membranes: The Relationships of Acid Concentration and Proton Mobility to Water Content and Their Effect upon Proton Conductivity. J. Mater. Chem. 2007, 17 (30), 3255.

(21) Agmon, N. The Grotthuss Mechanism. Chem. Phys. Lett. 1995, 244 (5), 456–462.

(22) Tuckerman, M. E.; Marx, D.; Parrinello, M. The Nature and Transport Mechanism of Hydrated Hydroxide Ions in Aqueous Solution. Nature 2002, 417 (6892), 925–929.

(23) Ludwig, R. New Insight into the Transport Mechanism of Hydrated Hydroxide Ions in Water. Angew. Chemie Int. Ed. 2003, 42 (3), 258–260.

(24) Kreuer, K.-D.; Rabenau, A.; Weppner, W. Vehicle Mechanism, A New Model for the Interpretation of the Conductivity of Fast Proton Conductors. Angew. Chemie Int. Ed. English 1982, 21 (3), 208–209.

(25) de Grotthuss, C. J. T. Mémoire Sur La Décomposition de L'eau et Des Corps Qu'elle Tient En Dissolution À L'aide de L'électricité Galvanique. Ann. Chim. 1806, 58, 54–74.

(26) Marx, D.; Tuckerman, M. E.; Parrinello, M. Solvated Excess Protons in Water: Quantum Effects on the Hydration Structure. J. Phys. Condens. Matter 2000, 12 (8A), A153–A159.

(27) de Grotthuss, C. J. T. Memoir on the Decomposition of Water and of the Bodies That It Holds in Solution by Means of Galvanic Electricity. Biochim. Biophys. Acta - Bioenerg. 2006, 1757 (8), 871–875.

(28) Park, M. J.; Kim, S. Y. Ion Transport in Sulfonated Polymers. J. Polym. Sci. Part B Polym. Phys. 2013, 51 (7), 481–493.

(29) Kreuer, K.-D. Proton Conductivity: Materials and Applications. Chem. Mater. 1996, 8 (19), 610–641.

(30) Kerres, J. A. Design Concepts for Aromatic Ionomers and Ionomer Membranes to Be Applied to Fuel Cells and Electrolysis. Polym. Rev. 2015, 55 (2), 273–306.

(31) Zhao, C.; Zhang, G.; Na, H. Sulfonated Poly(Ether Ketone) Membranes. In Electrochemical Polymer Electrolyte Membranes; Fang, J., Qiao, J., Wilkinson, D. P., Zhang, J., Eds.; Electrochemical Energy Storage and Conversion; CRC Press, 2015; pp 201–246.

(32) Higashihara, T.; Ueda, M. Sulfonated Poly(Ether Sulfone) Membranes. In Electrochemical Polymer Electrolyte Membranes; Fang, J., Qiao, J., Wilkinson, D. P., Zhang, J., Eds.; Electrochemical Energy Storage and Conversion; CRC Press, 2015; pp 133–200.

(33) Johnson, R. N.; Farnham, A. G.; Clendinning, R. A.; Hale, W. F.; Merriam, C. N. Poly(aryl Ethers) by Nucleophilic Aromatic Substitution. I. Synthesis and Properties. J. Polym. Sci. Part A-1 Polym. Chem. 1967, 5 (9), 2375–2398.

(34) Shin, D. W.; Guiver, M. D.; Lee, Y. M. Hydrocarbon-Based Polymer Electrolyte Membranes: Importance of Morphology on Ion Transport and Membrane Stability. Chem. Rev. 2017, acs.chemrev.6b00586.

(35) Miyatake, K.; Zhou, H.; Uchida, H.; Watanabe, M. Highly Proton Conductive Polyimide Electrolytes Containing Fluorenyl Groups. Chem. Commun. 2003, 32 (3), 368–369.

(36) Lee, H.-F.; Huang, Y.-C.; Wang, P.-H.; Lee, C. C.; Hung, Y.-S.; Gopal, R.; Holdcroft, S.; Huang, W.-Y. Synthesis of Highly Sulfonated Polyarylene Ethers Containing Alternating Aromatic Units. Mater. Today Commun. 2015, 3, 114–121.

(37) Litt, M.; Wycisk, R. Poly(arylenesulfonic Acids) with Frozen-In Free Volume as Hydrogen Fuel Cell Membrane Materials. Polym. Rev. 2015, 55 (2), 307–329.

(38) Sydlik, S. A.; Chen, Z.; Swager, T. M. Triptycene Polyimides: Soluble Polymers with High Thermal Stability and Low Refractive Indices. Macromolecules 2011, 44 (4), 976–980.

(39) Swager, T. M. Iptycenes in the Design of High Performance Polymers. Acc. Chem. Res. 2008, 41 (9), 1181–1189.

(40) Amara, J. P.; Swager, T. M. Incorporation of Internal Free Volume: Synthesis and Characterization of Iptycene-Elaborated Poly(butadiene)s. Macromolecules 2004, 37 (8), 3068–3070.

(41) Yuan, X.-Z.; Song, C.; Wang, H.; Zhang, J. Electrochemical Impedance Spectroscopy in PEM Fuel Cells; Springer London: London, 2010.

(42) Kim, Y. S.; Lee, K.-S. Fuel Cell Membrane Characterizations. Polym. Rev. 2015, 55 (2), 330–370.

(43) Lee, C. H.; Park, H. B.; Lee, Y. M.; Lee, R. D. Importance of Proton Conductivity Measurement in Polymer Electrolyte Membrane for Fuel Cell Application. Ind. Eng. Chem. Res. 2005, 44 (20), 7617–7626.

(44) Warburg, E. Ueber Das Verhalten Sogenannter Unpolarisirbarer Elektroden Gegen Wechselstrom. Ann. der Phys. und Chemie 1899, 303 (3), 493–499.

(45) Xie, Z.; Song, C.; Andreaus, B.; Navessin, T.; Shi, Z.; Zhang, J.; Holdcroft, S. Discrepancies in the Measurement of Ionic Conductivity of PEMs Using Two- and Four-Probe AC Impedance Spectroscopy. J. Electrochem. Soc. 2006, 153 (10), E173.

(46) Miyatake, K.; Chikashige, Y.; Higuchi, E.; Watanabe, M. Tuned Polymer Electrolyte Membranes Based on Aromatic Polyethers for Fuel Cell Applications. J. Am. Chem. Soc. 2007, 129 (13), 3879–3887.

(47) Kusoglu, A.; Weber, A. Z. New Insights into Perfluorinated Sulfonic-Acid Ionomers. Chem. Rev. 2017, 117 (3), 987–1104.

(48) Paddison, S. J. Proton Conduction Mechanisms at Low Degrees of Hydration in Sulfonic Acid-Based Polymer Electrolyte Membranes. Annu. Rev. Mater. Res. 2003, 33 (1), 289–319.

(49) Eikerling, M.; Kornyshev, A. A.; Kuznetsov, A. M.; Ulstrup, J.; Walbran, S. Mechanisms of Proton Conductance in Polymer Electrolyte Membranes. J. Phys. Chem. B 2001, 105 (17), 3646–3662.

(50) Bose, S.; Kuila, T.; Nguyen, T. X. H.; Kim, N. H.; Lau, K.; Lee, J. H. Polymer Membranes for High Temperature Proton Exchange Membrane Fuel Cell: Recent Advances and Challenges. Prog. Polym. Sci. 2011, 36 (6), 813–843.

(51) Blumenthal, G.; Cappadonia, M.; Lehmann, M. Investigation of the Proton Transport in Nafion® Membranes as a Function of Direction, Temperature and Relative Humidity. Ionics (Kiel). 1996, 2 (2), 102–106.

(52) Sugiyasu, K.; Song, C.; Swager, T. M. Tropone-Containing Polythiophene: Synthesis, Characterization, and Electrochemical Properties. Polym. Prepr. (American Chem. Soc. Div. Polym. Chem. 2006, 47 (2), 735–736.

(53) Sone, Y. Proton Conductivity of Nafion 117 as Measured by a Four-Electrode AC Impedance Method. J. Electrochem. Soc. 1996, 143 (4), 1254.

(54) Si, K.; Wycisk, R.; Dong, D.; Cooper, K.; Rodgers, M.; Brooker, P.; Slattery, D.; Litt, M. Rigid-Rod Poly(phenylenesulfonic Acid) Proton Exchange Membranes with Cross-Linkable Biphenyl Groups for Fuel Cell Applications. Macromolecules 2013, 46 (2), 422–433.

(55) Sanders, D. F.; Smith, Z. P.; Guo, R.; Robeson, L. M.; McGrath, J. E.; Paul, D. R.; Freeman, B. D. Energy-Efficient Polymeric Gas Separation Membranes for a Sustainable Future: A Review. Polymer (Guildf). 2013, 54 (18), 4729–4761.

(56) Gong, F.; Zhang, S. Synthesis of Poly(arylene Ether Sulfone)s with Locally and Densely Sulfonated Pentiptycene Pendants as Highly Conductive Polymer Electrolyte Membranes. J. Power Sources 2011, 196 (23), 9876–9883.

(57) Gong, F.; Mao, H.; Zhang, Y.; Zhang, S.; Xing, W. Synthesis of Highly Sulfonated Poly(arylene Ether Sulfone)s with Sulfonated Triptycene Pendants for Proton Exchange Membranes. Polymer (Guildf). 2011, 52 (8), 1738–1747.

(58) Bartlett, P. D.; Ryan, M. J.; Cohen, S. G. Triptycene 1 (9,10-O-Benzenoanthracene). J. Am. Chem. Soc. 1942, 64 (11), 2649–2653.

(59) Shao, Y.; Yin, G.; Wang, Z.; Gao, Y. Proton Exchange Membrane Fuel Cell from Low Temperature to High Temperature: Material Challenges. J. Power Sources 2007, 167 (2), 235–242.

(60) Siroma, Z.; Kakitsubo, R.; Fujiwara, N.; Ioroi, T.; Yamazaki, S.; Yasuda, K. Depression of Proton Conductivity in Recast Nafion® Film Measured on Flat Substrate. J. Power Sources 2009, 189 (2), 994–998.

(61) Cappadonia, M. Conductance of Nafion 117 Membranes as a Function of Temperature and Water Content. Solid State Ionics 1995, 77, 65–69.

(62) Varcoe, J. R.; Atanassov, P.; Dekel, D. R.; Herring, A. M.; Hickner, M. A.; Kohl, P. A.; Kucernak, A. R.; Mustain, W. E.; Nijmeijer, K.; Scott, K.; et al. Anion-Exchange Membranes in Electrochemical Energy Systems. Energy Environ. Sci. 2014, 7 (10), 3135–3191.

(63) Zakaria, Z.; Kamarudin, S. K.; Timmiati, S. N. Membranes for Direct Ethanol Fuel Cells: An Overview. Appl. Energy 2016, 163, 334–342.

(64) Nuñez, S. A.; Hickner, M. A. Quantitative 1 H NMR Analysis of Chemical Stabilities in Anion-Exchange Membranes. ACS Macro Lett. 2013, 2 (1), 49–52.

(65) Cheng, J.; He, G.; Zhang, F. A Mini-Review on Anion Exchange Membranes for Fuel Cell Applications: Stability Issue and Addressing Strategies. Int. J. Hydrogen Energy 2015, 40 (23), 7348–7360.

(66) Gu, S.; Cai, R.; Yan, Y. Self-Crosslinking for Dimensionally Stable and Solvent-Resistant Quaternary Phosphonium Based Hydroxide Exchange Membranes. Chem. Commun. 2011, 47 (10), 2856.

(67) Noonan, K. J. T.; Hugar, K. M.; Kostalik, H. A.; Lobkovsky, E. B.; Abruña, H. D.; Coates, G. W. Phosphonium-Functionalized Polyethylene: A New Class of Base-Stable Alkaline Anion Exchange Membranes. J. Am. Chem. Soc. 2012, 134 (44), 18161–18164.

(68) Zhang, B.; Gu, S.; Wang, J.; Liu, Y.; Herring, A. M.; Yan, Y.; He, G. H.; Yan, Y. S.; Garzon, F.; Wood, D.; et al. Tertiary Sulfonium as a Cationic Functional Group for Hydroxide Exchange Membranes. RSC Adv. 2012, 2 (33), 12683.

(69) Gu, S.; Wang, J.; Kaspar, R. B.; Fang, Q.; Zhang, B.; Bryan Coughlin, E.; Yan, Y. Permethyl Cobaltocenium (Cp*2Co+) as an Ultra-Stable Cation for Polymer Hydroxide-Exchange Membranes. Sci. Rep. 2015, 5, 11668.

(70) Yan, X.; Wu, X.; He, G.; Gu, S.; Gong, X.; Benziger, J. A Methanesulfonic Acid/sulfuric Acid-Based Route for Easily-Controllable Chloromethylation of Poly(ether Ether Ketone). J. Appl. Polym. Sci. 2015, 132 (5), n/a-n/a.

(71) Conceição, T. F.; Bertolino, J. R.; Barra, G. M. O.; Mireski, S. L.; Joussef, A. C.; Pires, A. T. N. Preparation and Characterization of Poly(ether Ether Ketone) Derivatives. J. Braz. Chem. Soc. 2008, 19 (1).

(72) Shackelford, S. A.; Anderson, M. B.; Christie, L. C.; Goetzen, T.; Guzman, M. C.; Hananel, M. A.; Kornreich, W. D.; Li, H.; Pathak, V. P.; Rabinovich, A. K.; et al. Electrophilic Tetraalkylammonium Nitrate Nitration. II. Improved Anhydrous Aromatic and Heteroaromatic Mononitration with Tetramethylammonium Nitrate and Triflic Anhydride, Including Selected Microwave Examples †. J. Org. Chem. 2003, 68 (2), 267–275.

(73) Chen, Z.; Swager, T. M. Synthesis and Characterization of Poly(2,6-Triptycene). Macromolecules 2008, 41 (19), 6880–6885.

(74) White, N. G.; MacLachlan, M. J. Soluble Tetraaminotriptycene Precursors. J. Org. Chem. 2015, 80 (16), 8390–8397.

(75) Zhao, Z.; Gong, F.; Zhang, S.; Li, S. Poly(arylene Ether Sulfone)s Ionomers Containing Quaternized Triptycene Groups for Alkaline Fuel Cell. J. Power Sources 2012, 218, 368–374.

(76) Liu, L.; Ahlfield, J.; Tricker, A.; Chu, D.; Kohl, P. A.; Tavares, A. C.; Pivovar, B. S.; Li, X.; Lu, J.; Zhuang, L.; et al. Anion Conducting Multiblock Copolymer Membranes with Partial Fluorination and Long Head-Group Tethers. J. Mater. Chem. A 2016, 4 (41), 16233–16244.

(77) Ran, J.; Wu, L.; Varcoe, J. R.; Ong, A. L.; Poynton, S. D.; Xu, T. Development of Imidazolium-Type Alkaline Anion Exchange Membranes for Fuel Cell Application. J. Memb. Sci. 2012, 415–416, 242–249.

(78) Ye, Y.; Elabd, Y. A. Relative Chemical Stability of Imidazolium-Based Alkaline Anion Exchange Polymerized Ionic Liquids. Macromolecules 2011, 44 (21), 8494–8503.

Chapter 2. Dithiolodithiole as a Building Block for Conjugated Materials in Photovoltaic Devices

This chapter is adapted from the paper by Schipper et al and the contribution was evenly distributed between Dr. Derek Schipper and myself.[79] All starting dialkynes were synthesized by Dr. Derek Schipper and were subsequently converted to dithiolodithiole derivatives by Dr. Derek Schipper and myself. My main contribution was in the characterization of the photophysical and electrochemical properties of the compounds. Dr. Peter Müller obtained all the crystal structures that were discussed in this project.

2.1.Introduction

Since the discovery of organic semiconductors in 1862 and the development of synthetic methods and control over their conductivity in 1977 that led to the Nobel Prize in Chemistry in 2000,[80] chemists have been exploring new functional groups to create new materials for specific applications in organic electronics such as field effect transistors, light emitting diodes, photo detectors, and solar cells.[81–90] Organic semiconductors have many advantages over inorganic materials such as low temperature fabrication, compatibility with flexible substrates, versatile chemistries, and customizable chemical structures. However, they are currently still lacking in performance and in some cases stability. In the field of photovoltaics, organic solar cells, at best, have an efficiency of around 12% as compared to silicon solar cells at 27%.[91] Thus, there is a need to create new materials for organic solar cells.

An organic solar cell is typically made up of a light absorbing layer sandwiched between a transparent electrode and a metal electrode.[88] (Figure 2.1-1) The light absorbing layer is made up of a mixture of an electron donor and an electron acceptor. When light is absorbed by the electron donating material, electrons in the highest occupied molecular orbital (HOMO) are excited beyond the lowest unoccupied molecular orbital (LUMO) to form excitons or electron-hole pairs. (Figure 2.1-1(1)) The electron and hole in each exciton are associated to each other through a weak electrostatic interaction. These

excitons would diffuse to the interface between the donor and acceptor material (Figure 2.1-1(2)) where it becomes dissociated into holes and electrons. (Figure 2.1-1(3)) These mobile charges would then diffuse to the respective electrodes and into the external circuit to create current that can drive a load. (Figure 2.1-1(4))

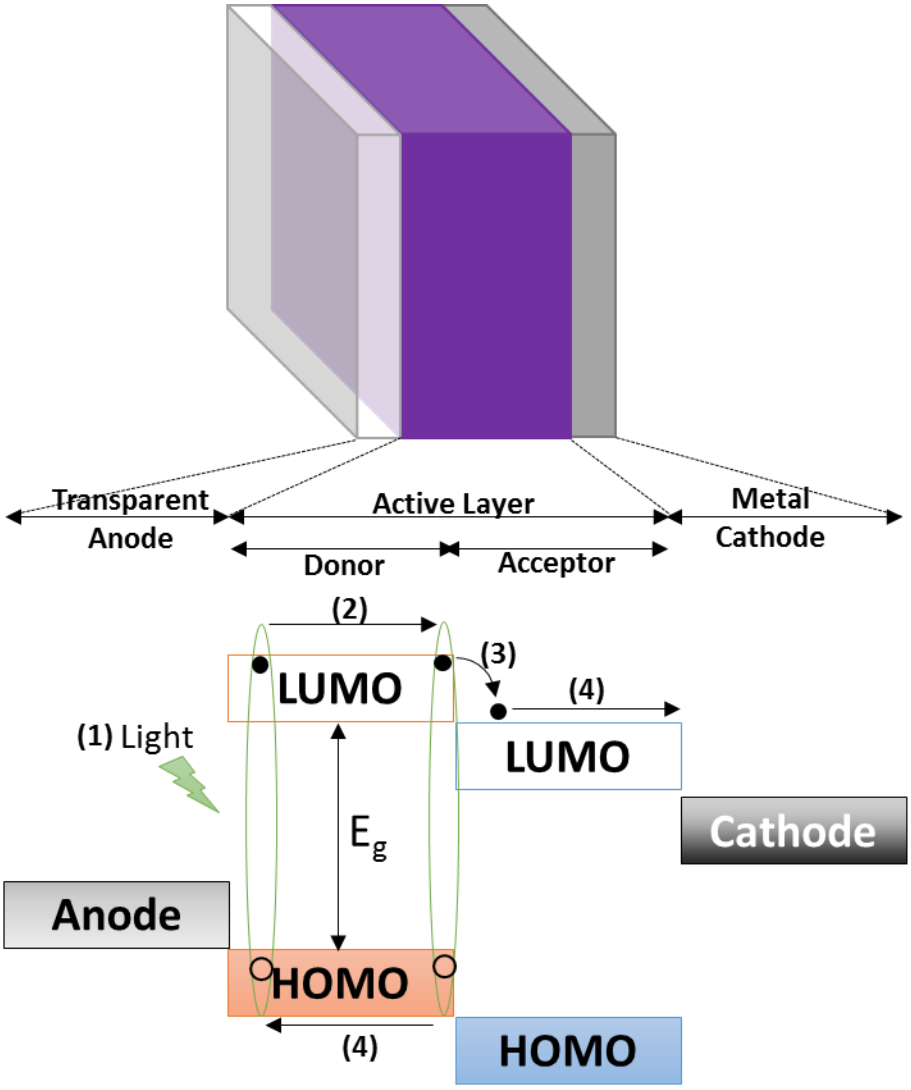

Figure 2.1-1. Schematic of an organic solar cell. Numbers correspond to the events within a solar cell that converts light to electricity. (1) Light is absorbed in the electron donor and excites an electron to form an exciton. (2) Exciton diffuses to the interface between electron donor and acceptor. (3) At the interface, the exciton splits into unbound electron and hole. (4) Electrons and holes then diffuse to the electrodes through the electron acceptor and donor phases respectively.

The ongoing challenge is to develop new improved materials to (i) absorb more light in the solar spectrum, (ii) efficiently split and transport the charge carriers to the electrodes and (iii) be chemically

stable during operation.[88] These requirements translate into material properties such as a relatively low optical band gap, high charge mobility, and chemical stability respectively. Many functional groups have been developed in this field to customize new materials for these specific properties and have been extensively reviewed over the years.[81–87] These functional groups can be divided into two groups, electron donors and electron acceptors. Many different combinations of these functional groups have resulted in a variety of strategies in optimizing the properties for photovoltaics. One particular strategy that has been employed repeatedly is to use donor-acceptor interactions in narrowing the bandgap.[81,83,86]

The optical bandgap is related the difference in energy level between the HOMO and LUMO states. Only photons with higher energy than the bandgap is absorbed by the material. Thus in order to increase the absorption of visible light within the solar spectrum, a narrow bandgap of less 1.5 eV is preferred.[86] The bandgap of an organic semiconductor is closely related to the delocalization of its extended π-electron system and the heteroatoms, which is affected by average bond length alternation between conjugated nearest carbon atoms and planarity of the molecule.[83]

Organic semiconductors are conjugated molecules with linked carbon-carbon double bonds in which their π-electrons are delocalized due to the existence of nondegenerate resonance structures at the ground state. In polyaromatic conjugated systems, the two resonance structures are the energetically more stable aromatic structure and the quinoidal structure. (Figure 2.1-2) Although the quinoidal structure is less stable as compared to the aromatic structure, more uniformity in carbon-carbon bond lengths indicate a closer energy between the aromatic and quinoidal structures and gives rise to a lower bandgap. Thus, one key strategy to reduce band gap is to improve the stability of the quinoidal structure or destabilize the aromatic structure.

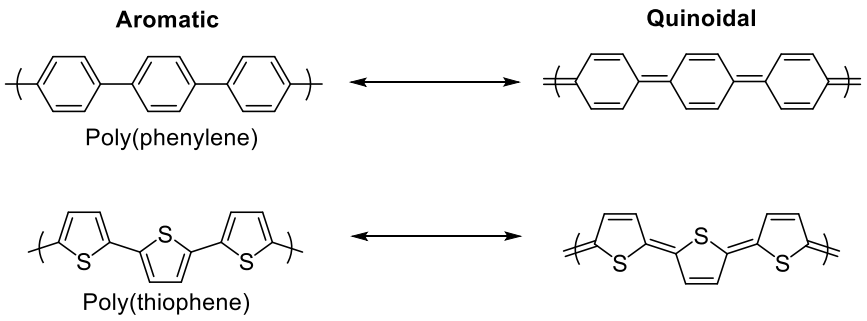

Figure 2.1-2. Examples of aromatic and quinoidal forms of common polyaromatic conjugated polymers, poly(phenylene) and poly(thiophene).

The second factor affecting the delocalization of the π-electron system in organic semiconductors is the planarity of the molecule. In polyaromatic conjugated polymers, π-bonds are parallel to the plane of aromatic groups. If neighboring aromatic rings are at an angle, overlap of the π-electron cloud is reduced and an increase in bandgap is observed. Hence, to narrow a bandgap and promote electronic delocalization, the dihedral angle between consecutive rings needs generally needs to be close to 0. One structural design to ensure a low dihedral angle is to introduce fused ring structures.

Organic semiconductors based on donor-acceptor interactions were found to stabilize the quinoidal structure and improve the planarity of the molecule which results in narrow bandgap semiconductors.[81,83,86] Currently, many donor units are based on the thiophene functional group due to the unique electronic and physical properties that the sulfur atom impart. The high polarizability of the sulfur atom stabilizes the conjugation in the thiophene unit. Furthermore, strong binding between sulfur and an array of other atoms such as gold and sulfur itself aids the self-assembly of thiophene based semiconductors for better charge transport properties.[92] Herein, I would describe our design for a new functional group, dithiolodithiole (C_4S_4) (Figure 2.1-3), a sulfur-rich, fused ring donor unit, in an effort to further expand the scope of available building blocks for organic semiconductors.

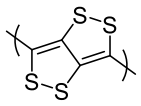

Dithiolodithole

Figure 2.1-3. Structure of the dithiolodithiol (C_4S_4) functional group.

A rudimentary analysis to compare some commonly employed electron donors was done to identify the potential of the C_4S_4 unit (Figure 2.1-4). Thiophenes have a lower aromatic stabilization energy which contributes to lower HOMO-LUMO gaps in the resulting analogous materials. This effect is demonstrated by the difference in wavelength of maximum absorption (λ_{max}) between p-terphenyl (274 nm) (Figure 2.1-4a) and 2,5-diphenylthiophene (326 nm) (Figure 2.1-4b). Substitution with 2-benzothiophene leads to a further reduction in HOMO-LUMO gap (369 nm) (Figure 2.1-4c) due to a partial retention of aromatic character in the excited state. Additionally, (benzo)thiophenes can exhibit S–S contacts in the solid state which can lead to favorable change transport characteristics.[93,94]

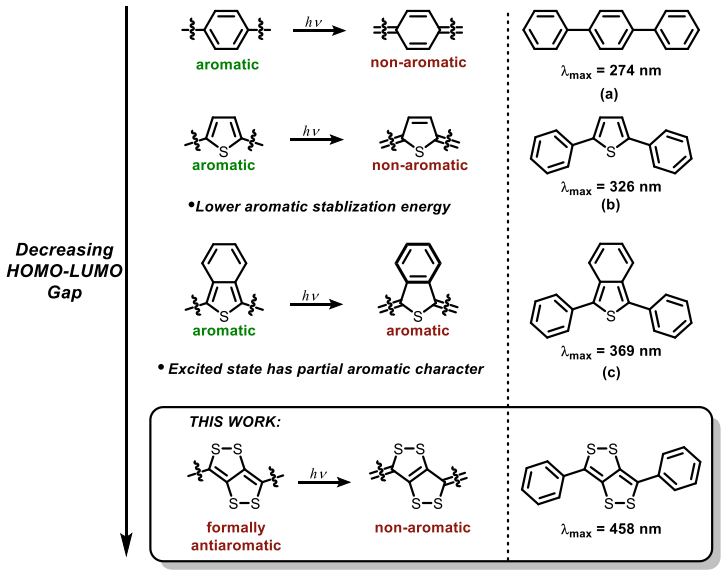

Figure 2.1-4. Comparison of various conjugated building blocks. Wavelength of maximum absorption (λ_{max}) for (a) p-terphenyl, (b) 2,5-diphenylthiophene and (c) 2,5-diphenyl benzothiophene are listed.

Successful implementation (benzo)thiophene-based materials for a variety of applications are ascribable to the range of desirable properties they exhibit.[95] Given that these properties can be attributed

to the presence of a sulfur atom and/or fused ring system, we hypothesized that a heterocycle that contains multiple sulfur atoms in a fused ring system may lead to a material with enhanced properties. A survey of possible atomic arrangements revealed that the dithiolodithiole (C_4S_4) heterocycle could be a viable candidate. Examination of the C_4S_4 unit reveals a 12e (formally anti-aromatic by Hückel's rule) π system in the ground state that is not aromatically stabilized and a non-aromatic π system in the quinoidal excited state. This behavior could potentially lead to a donor unit that can have a low bandgap. Illustratively, the absorption maximum of 3,6-diphenyldithiolodithiole (458 nm) is at significantly longer wavelength than the analogous (benzo)thiophene materials.

Despite the potential advantages of the C_4S_4 system, literature examples are scant.[96–99] In order to study C_4S_4 derivatives in more detail, synthetic accessibility is required. A suitable approach was demonstrated by Blum and co-workers who reported the synthesis of a single example of a C_4S_4 derivative in 26% yield from 1,4-diphenylbutadiyne and elemental sulfur at 150 °C for 52 hours.[96] Although butadiynes and elemental sulfur are convenient starting materials, a reduction of reaction times and increase in yields would be beneficial. Thus in this project, the synthesis conditions for synthesizing the C_4S_4 unit were first optimized, before a library of C_4S_4 derivatives were made and characterized for their photophysical and electrochemical properties.

2.2. Results and Discussion

Starting from the conditions reported by Blum et al.,[96] various reaction conditions were screened. Two sets of conditions were identified, using either thermal (conditions A) or microwave heating (conditions B), which improved both the reaction time and product yield (Scheme 2.2-1). In most cases, addition of a disulfide catalyst proved beneficial for achieving shorter reaction times and/or lower reaction temperatures. The reaction likely proceeds through sulfur-centered radicals with the disulfide catalyst acting as a radical mediator.

Scheme 2.2-1. Reaction conditions for synthesizing ditholodithole functional group.

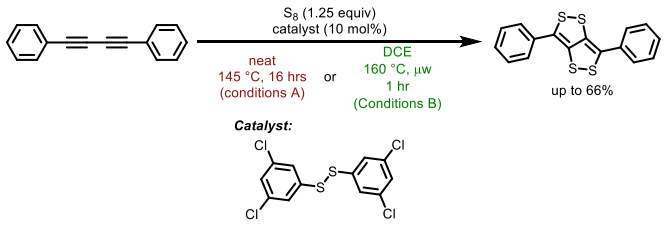

The synthesis of a variety of different C_4S_4 derivatives was carried out using the newly developed conditions. (Table 2.2-1) (See Appendix A for synthesis of all materials and raw CV and UV/Vis data) The reaction is tolerant of a variety of functional groups including halogens, alkyl, ester, cyano and boronic esters. The reaction yields are adequate (11-66%) to obtain material to study the photophysical and electrochemical properties. Substrates containing only strong electron-donating group led to a complex mixture of products (Figure 2.2-1) of which some have been completely characterized. (Appendix A)

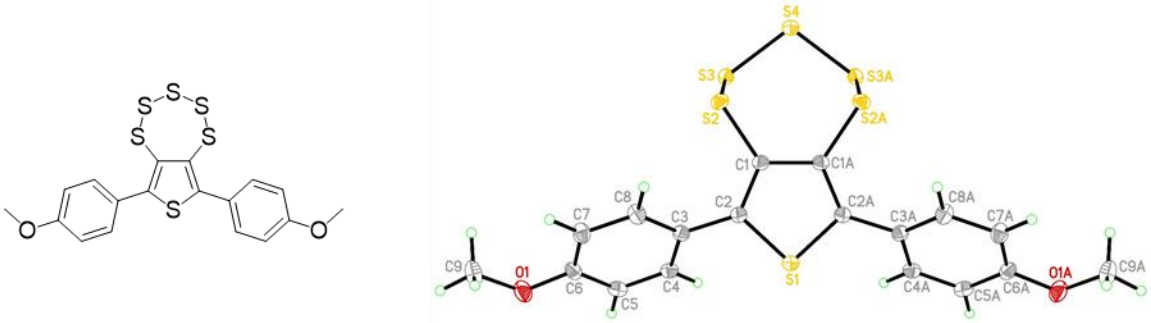

Figure 2.2-1. One of the side products found in the mixture for derivatives with only strong electron donating groups

From the absorption spectra, the C_4S_4 derivatives generally display a relatively broad absorption band with absorption maxima (λ_{max}) ranging from 449 nm to 649 nm with molar extinction coefficients (ε) ranging from 5700-26300 $M^{-1}cm^{-1}$. Compounds with electron withdrawing groups generally exhibit a bathochromic shift as well as an increase in ε values likely due to the increased donor-π-acceptor nature of the chromophore.[85] The ability of the C_4S_4 to act as a strong electron-donating group was also confirmed by the relatively low oxidation potential. Cyclic voltammetry of this series of compounds reveals two reversible oxidations with $E_{1/2}$ values ranging from 0.01 V to 0.21 V for the first oxidation and 0.62 V to

0.78 V for the second oxidation relative to a Fc/Fc^+ reference. The UV/Vis and CV data were used to estimate bandgap E_g and HOMO/LUMO values, summarized in Table 2.2-1.

Table 2.2-1. Dithiolodithiole scope and photo/electrochemical properties. (a) Isolated yield. (b) Measured in CH_2Cl_2. (c) CV measured in CH_2Cl_2 with 0.1 M nBu_4NPF_6 as supporting electrolyte using a Pt button working electrode, Pt counter electrode with Fc/Fc^+ reference. (d) Estimated from the absorption onset: $E_g = 1240/\lambda$. (e) Calculated from the first oxidation $E_{1/2}$: HOMO = $-(E_{1/2ox} + 4.80)$; LUMO = HOMO – E_g. EH = 2-ethylhexyl, Pin = Pinacolato.

Product	Yield[a]	λ_{max}[b] (nm)	ε[b] (M^{-1} cm^{-1})	$E_{1/2}$ vs Fc/Fc^+[c] (V)	Bandgap[d] (eV)	HOMO/LUMO[e] (eV)
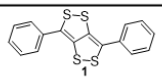 **1**	66%	458	8580	0.06, 0.67	2.38	-4.86/-2.48
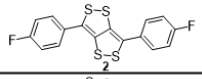 **2**	54%	449	5750	0.09, 0.68	2.41	-4.88/-2.48
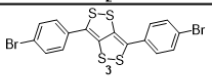 **3**	17%	463	5810	0.13, 0.71	2.32	-4.95/-2.63
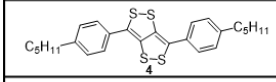 **4**	58%	455	6920	0.01, 0.62	2.40	-4.80/-2.40
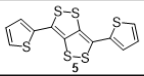 **5**	21%	370	12600	0.75	2.88	-5.59/-2.71
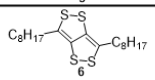 **6**	16%	238	11100	--	3.40	--
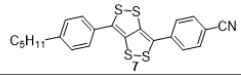 **7**	24%	517	26300	0.13, 0.71	2.14	-4.93/-2.79
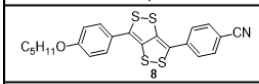 **8**	23%	516	18000	0.10, 0.65	2.15	-4.90/-2.75
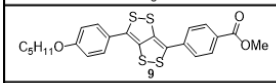 **9**	31%	507	13300	0.06, 0.63	2.19	-4.88/-2.69
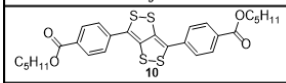 **10**	21%	520	21000	0.16, 0.74	2.13	-4.96/-2.83
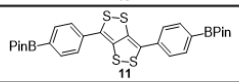 **11**	11%	503	9870	0.09, 0.69	2.24	-4.89/-2.55
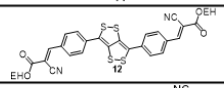 **12**	21%	630	14800	0.21, 0.76	1.73	-5.01/-3.28
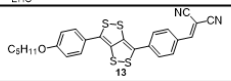 **13**	27%	649	14000	0.10, 0.63	1.65	-4.90/-3.25

Materials that undergo significant redox induced changes in their absorption properties have demonstrated utility in electrochromic devices[100–103] and electrochemical oxidation of C_4S_4 derivatives were studied using spectroelectrochemistry. An illustrative example using **7** is depicted in Figure 2.2-2. As shown, the radical cation produces the longest wavelength absorptions whereas further oxidation to the closed shell dication produces a shift to a larger bandgap. Apart from the drastic change in UV/Vis absorption upon

oxidation, further evidence for oxidation of the π-system as opposed to oxidation of sulfur atoms is provided by the fact that **6** does not undergo oxidation within the solvent window. Compound **6** would be expected to have similar $E_{1/2}$ values as compared to other C_4S_4 compounds if oxidation occurred at the sulfur atom, but very different $E_{1/2}$ values if oxidation occurs at the π-system given the disparate nature of the conjugated systems.

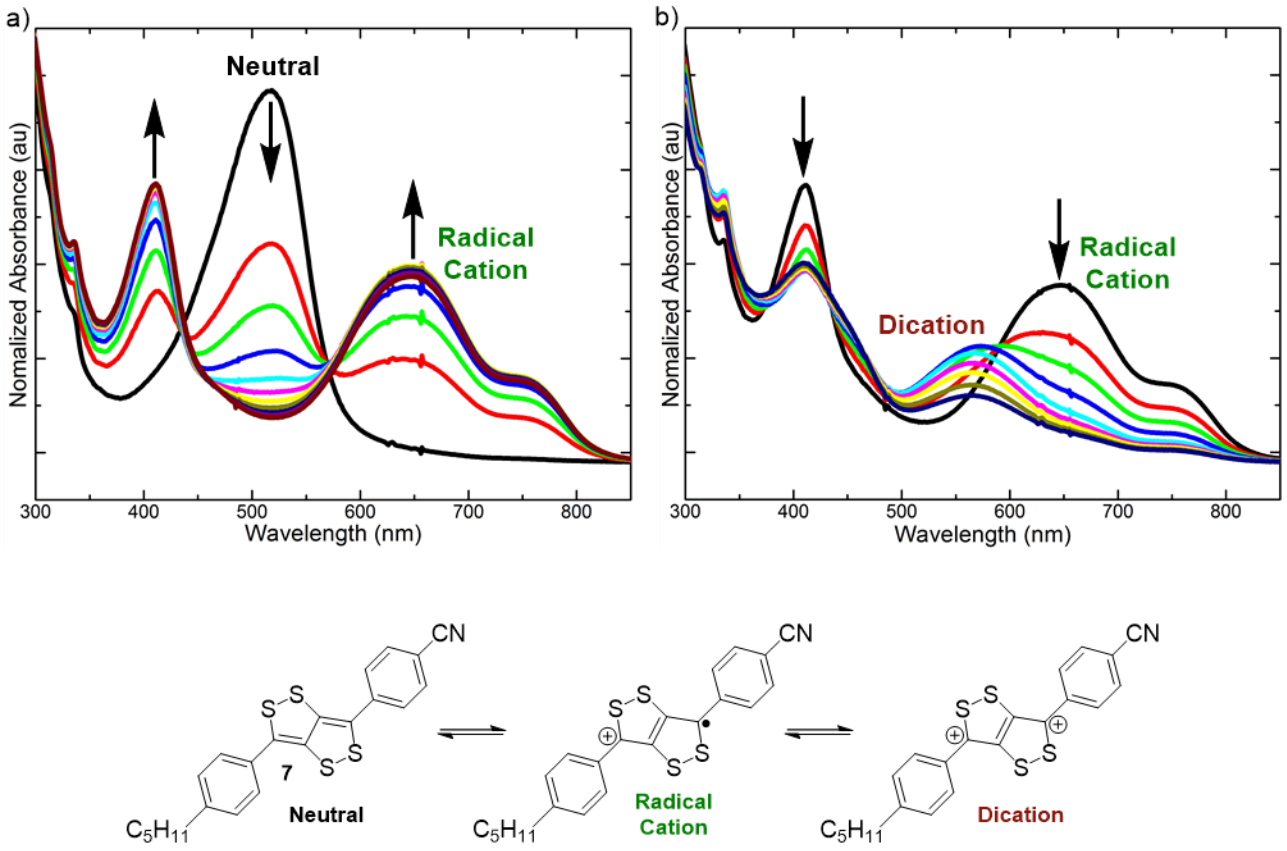

Figure 2.2-2. Spectroelectrochemistry of Compound **7**. Absorption spectra taken in situ with sample in a quartz electrochemical cell in a 0.1 M nBu_4NPF_6 in CH_2Cl_2 solution with a gold working electrode, gold counter electrode and a gold reference electrode that is externally referenced with Fc/Fc^+. Sample was held at a fix potential beyond (a) the first and (b) second oxidation peaks and the absorption spectra was taken every 30 seconds.

The x-ray crystal structures of Compounds **1** and **12** are shown in Figure 2.2-3 along with some elements of their packing characteristics. The morphology of organic materials in the solid state is an important parameter that strongly affects performance in a variety of potential applications.[104–106] Thiophenes have been shown to exhibit favourable charge transport properties due, in part, to their ability

of form S–S contacts.[105,107–109] The presence of multiple sulfur atoms in the C_4S_4 heterocycle will likely lead to a higher degree of S–S contacts in the solid state and perhaps to favourable charge transport properties. Indeed, x-ray crystallography of **1** reveals multiple possible S–S contacts for the sulfurs of the C_4S_4 heterocycle. "Internal" sulfurs exhibit two S–S contacts whereas the "external" sulfurs exhibit one S–S contact. Overall, this leads to six S–S contacts for a single molecule which compares favourably to analogous thiophene compounds. Additionally, the presence of a large number of S–S contacts imparts highly crystalline characteristics, which could lead to favourable charge transport properties. Moreover, the crystal structure of **1** reveals that there is a significant dihedral angle of 24.54(4)° between the planes defined by the central C_4S_4 heterocycle and the pendant phenyl rings. This high value of dihedral angle may limit the effective conjugation length of the molecule. However, other C_4S_4 derivatives can exhibit very different molecular packing depending on the nature of the substituents employed. For example, the molecular packing of **12**, which contains strong electron withdrawing groups (2-cyanoacrylate), is dominated by intermolecular charge transfer interactions between electron rich C_4S_4 heterocycle and electron poor 2-cyanoacrylate groups while not exhibiting any close S–S contacts. The intermolecular distance for **12** of 3.312 Å indicates the close proximity of the conjugated systems within the crystal packing which should be favourable for charge transport properties. In addition, the dihedral angle between the C_4S_4 heterocycle and the phenyl rings of **12** is 0.49(8)°, which indicates a higher degree of π-orbital overlap and increased effective conjugation length than that of **1**, as a result of enhanced electronic communication between the electron rich C_4S_4 heterocycle and electron poor 2-cyanoacrylate group. These altering characteristics demonstrate the tunability of properties for this series of compounds by varying substituents.

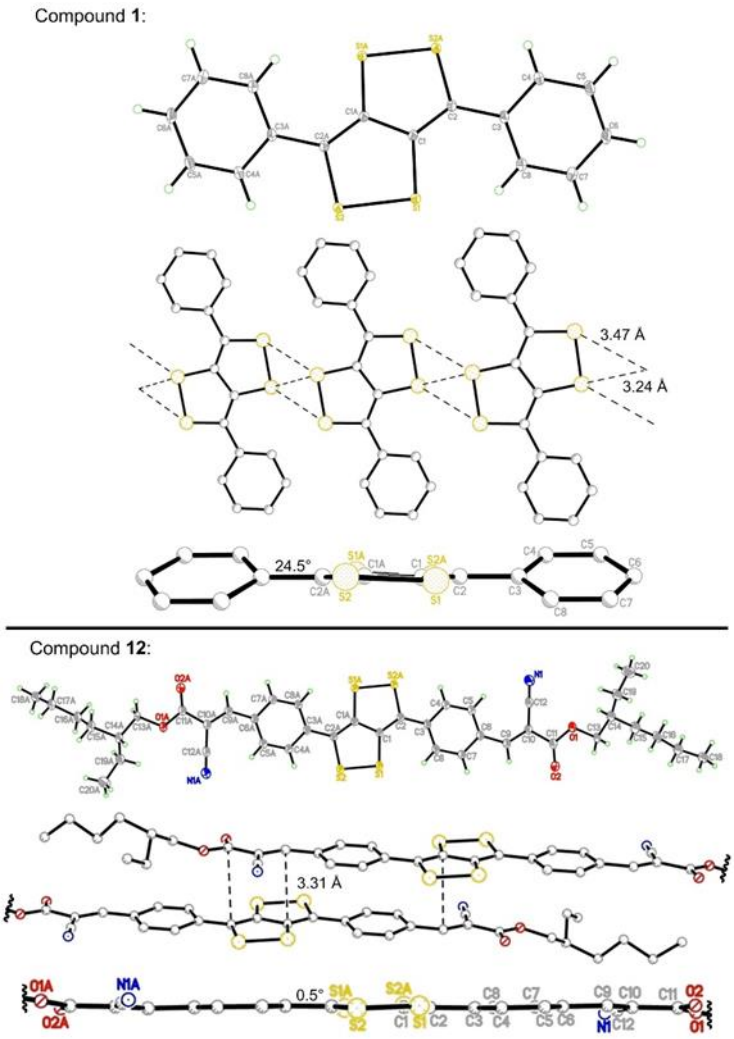

Figure 2.2-3. Crystal structure of compound 1 and 12.

Given that many high performance organic electronic materials include thiophene moieties, a direct comparison of a thiophene- with C_4S_4-based material would be germane. (Figure 2.2-4) Thiophene based analogues, **14**, **15**, and **16** of C_4S_4-based **7**, **9** and **10** respectively were synthesized and characterized. These compounds have the same substitution pattern and functional groups, with the only difference being the central heterocycle. Additionally, both chromophores have equal π-conjugation lengths with both C_4S_4 and thiophene being a four carbon π-conjugated unit. However, the disparity of the resulting properties is striking. UV/Vis spectroscopy reveals that compounds **7**, **9** and **10** exhibit much broader absorption than **14**, **15** and **16**. Moreover, the absorption maximum and onset of absorption is, on average, redshifted by

160 nm and 175 nm respectively when moving from thiophene to analogous C_4S_4-based materials. Cyclic voltammetry (CV) demonstrates that C_4S_4 donates electrons much more readily than thiophene since **14**, **15** and **16** have an average 0.84 V higher $E_{1/2}$ value for the first oxidation event. Moreover, C_4S_4 derivatives will lose a second electron to form a dication at a lower oxidation potential than it takes analogous thiophene derivatives to lose the first electron. UV/Vis and CV data were also used to estimate the energy level diagram for comparison between C_4S_4 and thiophene compounds. C_4S_4 derivatives have significantly smaller HOMO-LUMO gaps, ranging from than 0.85 eV difference between **9** and **15** to 1.00 eV difference between **10** and **16**. This difference is due mainly to a much higher lying HOMO level but also, in part, a slightly lower lying LUMO level.

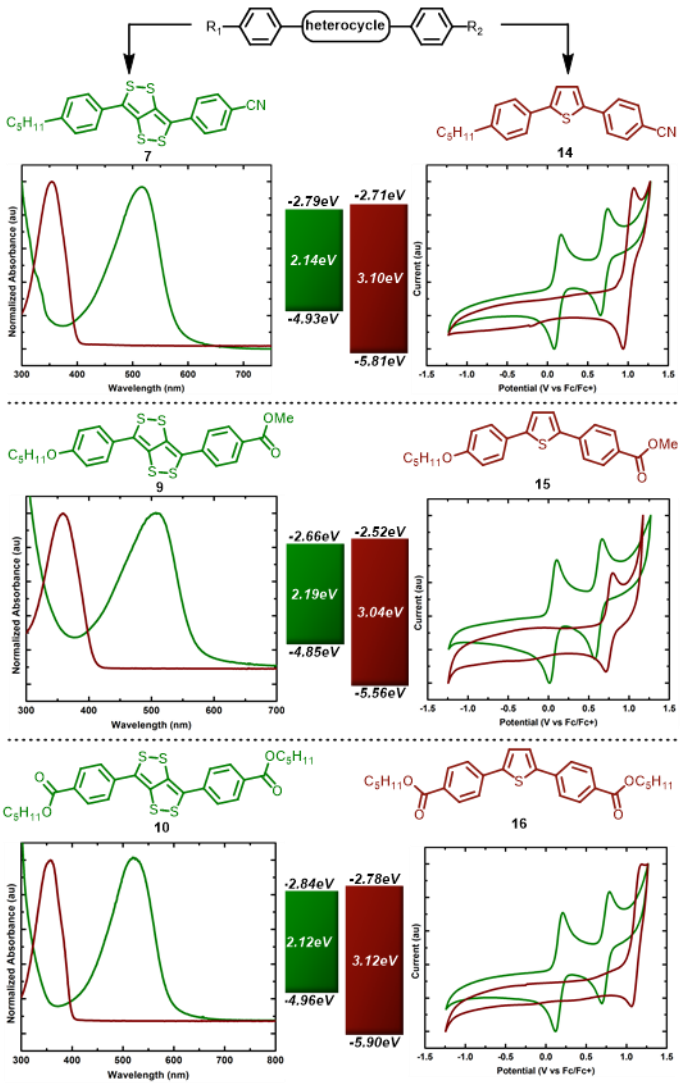

Figure 2.2-4. Direct comparison of photo/electro properties of dithiolodithiole and its thiophene counterpart.

2.3. Conclusion

In conclusion, we have demonstrated the use of the dithiolodithiole heterocycle as a new building block for organic electronic materials. The dithiolodithiole motif is readily synthetically accessible using catalytic processes. Materials containing dithiolodithioles tend to be highly crystalline due to multiple close S–S contacts or charge transfer interactions in the solid state and exhibit complimentary optical and electronic properties compared to analogous, widely used thiophene derivatives. The varying properties of C_4S_4 derivatives should lead to ability to fine tune both the molecular and bulk properties of materials based

on this building block by judicious choice of substituents. This work should contribute meaningfully to the repertoire of available building blocks for conjugated organic materials and lead to the discovery of new materials with exciting properties.

2.4. References

(79) Schipper, D. J.; Moh, L. C. H.; Müller, P.; Swager, T. M. Dithiolodithiole as a Building Block for Conjugated Materials. *Angew. Chemie, Int. Ed.* **2014**, *53* (23), 5847–5851.

(80) Norden, B.; Krutmeijer, E. The Nobel Prize in Chemistry 2000 - Advanced Information https://www.nobelprize.org/nobel_prizes/chemistry/laureates/2000/advanced.html (accessed Apr 2, 2017).

(81) Guo, X.; Baumgarten, M.; Müllen, K. Designing π-Conjugated Polymers for Organic Electronics. *Prog. Polym. Sci.* **2013**, *38* (12), 1832–1908.

(82) Müllen, K.; Pisula, W. Donor–Acceptor Polymers. *J. Am. Chem. Soc.* **2015**, *137* (30), 9503–9505.

(83) Liu, C.; Wang, K.; Gong, X.; Heeger, A. J. Low Bandgap Semiconducting Polymers for Polymeric Photovoltaics. *Chem. Soc. Rev.* **2016**, *45* (17), 4825–4846.

(84) Heeger, A. J. Semiconducting Polymers: The Third Generation. *Chem. Soc. Rev.* **2010**, *39* (7), 2354–2371.

(85) Ni, W.; Wan, X.; Li, M.; Wang, Y.; Chen, Y.; Zhu, D.; Zhan, X.; Wan, X.; Chen, Y.; Bauerle, P.; et al. A–D–A Small Molecules for Solution-Processed Organic Photovoltaic Cells. *Chem. Commun.* **2015**, *51* (24), 4936–4950.

(86) Jemison, R. C.; McCullough, R. D. Techniques for the Molecular Design of Push-Pull Polymers towards Enhanced Organic Photovoltaic Performance. In *ACS Symposium Series*; Li, L., Wong-Ng, W., Sharp, J., Eds.; ACS Symposium Series; American Chemical Society: Washington, DC, 2014; Vol. 1161, pp 71–109.

(87) Jeffries-EL, M.; Kobilka, B. M.; Hale, B. J. Optimizing the Performance of Conjugated Polymers in Organic Photovoltaic Cells by Traversing Group 16. *Macromolecules* **2014**, *47* (21), 7253–7271.

(88) Hedley, G. J.; Ruseckas, A.; Samuel, I. D. W. Light Harvesting for Organic Photovoltaics. *Chem. Rev.* **2017**, *117* (2), 796–837.

(89) Root, S. E.; Savagatrup, S.; Printz, A. D.; Rodriquez, D.; Lipomi, D. J. Mechanical Properties of Organic Semiconductors for Stretchable, Highly Flexible, and Mechanically Robust Electronics.

Chem. Rev. **2017**, acs.chemrev.7b00003.

(90) Liu, X.; Chen, H.; Tan, S. Overview of High-Efficiency Organic Photovoltaic Materials and Devices. *Renew. Sustain. Energy Rev.* **2015**, *52*, 1527–1538.

(91) NREL. Best Research-Cell Efficiencies https://www.nrel.gov/pv/assets/images/efficiency-chart.png (accessed Apr 2, 2017).

(92) Mishra, A.; Ma, C.-Q.; Bäuerle, P. Functional Oligothiophenes: Molecular Design for Multidimensional Nanoarchitectures and Their Applications. *Chem. Rev.* **2009**, *109* (3), 1141–1276.

(93) Liu, Y.; Di, C.; Du, C.; Liu, Y.; Lu, K.; Qiu, W.; Yu, G. Synthesis, Structures, and Properties of Fused Thiophenes for Organic Field-Effect Transistors. *Chem. - A Eur. J.* **2010**, *16* (7), 2231–2239.

(94) Curtis, M. D.; Cao, J.; Kampf, J. W. Solid-State Packing of Conjugated Oligomers: From π-Stacks to the Herringbone Structure. *J. Am. Chem. Soc.* **2004**, *126* (13), 4318–4328.

(95) Yao, H.; Ye, L.; Zhang, H.; Li, S.; Zhang, S.; Hou, J. Molecular Design of Benzodithiophene-Based Organic Photovoltaic Materials. *Chem. Rev.* **2016**, *116* (12), 7397–7457.

(96) Blum, J.; Badrieh, Y.; Shaaya, O.; Meltser, L.; Schumann, H. On the Various Modes of Interaction of Sulfur with Phenylated Diynes. *Phosphorus, Sulfur, and Silicon* **1993**, *79*, 87–96.

(97) Chiacchio, U.; Corsaro, A.; Rescifina, A.; Testa, M. G.; Purrello, G. The Reaction of Unsaturated Carbonyl Compounds with Activated Sulfur. *Heterocycles* **1993**, *36* (2), 223–229.

(98) Chiacchio, U.; Corsaro, A.; Pistara, V.; Rescifina, A.; Purrello, G. The Reaction of Unsaturated Carbonyl Compounds With "activated" sulfur. Part 3. Reaction Course. *Phosphorus, Sulfur Silicon Relat. Elem.* **1998**, *134/135*, 463–474.

(99) Stachel, H. D.; Schorp, M.; Zoukas, T. Condensed 1,2-Dithioles. II. Synthesis of Thieno-1,2-Dithioles. *Liebigs Ann. der Chemie* **1992**, No. 10, 1039–1044.

(100) Amb, C. M.; Dyer, A. L.; Reynolds, J. R. Navigating the Color Palette of Solution-Processable Electrochromic Polymers †. *Chem. Mater.* **2011**, *23* (3), 397–415.

(101) Argun, A. A.; Aubert, P.-H.; Thompson, B. C.; Schwendeman, I.; Gaupp, C. L.; Hwang, J.; Pinto, N. J.; Tanner, D. B.; MacDiarmid, A. G.; Reynolds, J. R. Multicolored Electrochromism in Polymers:

Structures and Devices. *Chem. Mater.* **2004**, *16* (23), 4401–4412.

(102) Stalder, R.; Mei, J.; Graham, K. R.; Estrada, L. A.; Reynolds, J. R. Isoindigo, a Versatile Electron-Deficient Unit For High-Performance Organic Electronics. *Chem. Mater.* **2013**, 131104151716007.

(103) Beaujuge, P. M.; Reynolds, J. R. Color Control in Pi-Conjugated Organic Polymers for Use in Electrochromic Devices. *Chem. Rev.* **2010**, *110* (1), 268–320.

(104) Ling, M. M.; Bao, Z. Thin Film Deposition, Patterning, and Printing in Organic Thin Film Transistors. *Chem. Mater.* **2004**, *16* (23), 4824–4840.

(105) Chung, H.; Diao, Y. Polymorphism as an Emerging Design Strategy for High Performance Organic Electronics. *J. Mater. Chem. C* **2016**, *4* (18), 3915–3933.

(106) Hains, A. W.; Liang, Z.; Woodhouse, M. A.; Gregg, B. A. Molecular Semiconductors in Organic Photovoltaic Cells. *Chem. Rev.* **2010**, *110* (11), 6689–6735.

(107) Liu, Y.; Di, C.; Du, C.; Liu, Y.; Lu, K.; Qiu, W.; Yu, G. Synthesis, Structures, and Properties of Fused Thiophenes for Organic Field-Effect Transistors. *Chem. - A Eur. J.* **2010**, *16* (7), 2231–2239.

(108) Curtis, M. D.; Cao, J.; Kampf, J. W. Solid-State Packing of Conjugated Oligomers: From π-Stacks to the Herringbone Structure. *J. Am. Chem. Soc.* **2004**, *126* (13), 4318–4328.

(109) Li, X.-C.; Sirringhaus, H.; Garnier, F.; Holmes, A. B.; Moratti, S. C.; Feeder, N.; Clegg, W.; Teat, S. J.; Friend, R. H. A Highly π-Stacked Organic Semiconductor for Thin Film Transistors Based on Fused Thiophenes. *J. Am. Chem. Soc.* **1998**, *120* (9), 2206–2207.

(110) Nie, X.; Wang, G. Synthesis and Self-Assembling Properties of Diacetylene Containing. 1–38.

(111) Neubert, M. E.; Fisch, M. R.; Keast, S. S.; Kim, J. M.; Lohman, M. C.; Murray, R. S.; Miller, K. J.; Shenoy, R. A.; Smith, M. J.; Stayshich, R. M.; et al. The Effect of Terminal Chain Modifications on the Mesomorphic Properties of 4,4′-Disubstituted Diphenyldiacetylenes. *Liq. Cryst.* **2004**, *31* (7), 941–963.

(112) Osowska, K.; Lis, T.; Szafert, S. Protection/Deprotection-Free Syntheses and Structural Analysis of (Keto-Aryl)diynes. *European J. Org. Chem.* **2008**, *2008* (27), 4598–4606.

(113) Cox, J. R.; Ferris, L. A.; Thalladi, V. R. Selective Growth of a Stable Drug Polymorph by

Suppressing the Nucleation of Corresponding Metastable Polymorphs. *Angew. Chemie Int. Ed.* **2007**, *46* (23), 4333–4336.

(114) Zhang, S.; Liu, X.; Wang, T. An Efficient Copper-Catalyzed Homocoupling of Terminal Alkynes to Give Symmetrical 1,4-Disubstituted 1,3-Diynes. *Adv. Synth. Catal.* **2011**, *353* (9), 1463–1466.

(115) Yin, W.; He, C.; Chen, M.; Zhang, H.; Lei, A. Nickel-Catalyzed Oxidative Coupling Reactions of Two Different Terminal Alkynes Using O2 as the Oxidant at Room Temperature: Facile Syntheses of Unsymmetric 1,3-Diynes. *Org. Lett.* **2009**, *11* (3), 709–712.

(116) Arakawa, Y.; Nakajima, S.; Ishige, R.; Uchimura, M.; Kang, S.; Konishi, G.; Watanabe, J. Synthesis of Diphenyl-Diacetylene-Based Nematic Liquid Crystals and Their High Birefringence Properties. *J. Mater. Chem.* **2012**, *22* (17), 8394.

(117) Spitler, E. L.; Koo, B. T.; Novotney, J. L.; Colson, J. W.; Uribe-Romo, F. J.; Gutierrez, G. D.; Clancy, P.; Dichtel, W. R. A 2D Covalent Organic Framework with 4.7-Nm Pores and Insight into Its Interlayer Stacking. *J. Am. Chem. Soc.* **2011**, *133* (48), 19416–19421.

(118) Sheldrick, G. M. Phase Annealing in SHELX-90: Direct Methods for Larger Structures. *Acta Crystallogr. Sect. A Found. Crystallogr.* **1990**, *46* (6), 467–473.

(119) Sheldrick, G. M. A Short History of SHELX. *Acta Crystallogr. Sect. A Found. Crystallogr.* **2008**, *64* (1), 112–122.

(120) Müller, P. Practical Suggestions for Better Crystal Structures. *Crystallogr. Rev.* **2009**, *15* (1), 57–83.

2.5. Appendix A

2.5.1. General Methods

Unless otherwise specified all reactions were run without regard to exclusion of ambient air or moisture. Microwave heating was performed using a CEM Discover Microwave at 200W unless otherwise stated. 4-*n*-Pentyloxyphenylacetylene and 4-*n*-Pentylphenylacetylene were purchased from Alfa Aesar. 4-Ethynylbenzonitrile was purchased from Aldrich. 2-Ethylhexyl cyanoacetate and bis(3,5-dichlorophenyl) disulfide were purchased from TCI. All other reagents and solvents were used as received from commercial sources. ^{1}H NMR spectra were recorded in $CDCl_3$ solutions on a Bruker AVANCE 400 or 600 MHz spectrometer. The chemical shift data are reported in units of δ (ppm) relative to residual solvent. All electrochemical measurements were carried out with Autolab PGSTAT30 potentiostat (Eco Chemie B.V.) in a conventional three-electrode configuration system: a platinum working electrode (1.6 mm diameter), a platinum wire counter electrode and a silver wire in 0.01mM silver nitrate in acetonitrile with 0.1mM nBu_4PF_6 as electrolyte in a porous vycor fritted electrode as pseudo-reference electrode with ferrocene added after every run as the internal standard. Dichloromethane was employed as the solvent with 0.1mM nBu_4NPF_6 as electrolyte and the experiments were performed under ambient condition with scan rate of 0.1 V/s. Ultraviolet-visible absorption spectra were measured with an Agilent 8453 diode array spectrophotometer and corrected for background signal with a solvent filled cuvette.

2.5.2. Preparation of Starting Materials

2.5.2.1. Pentyl 4-ethynylbenzoate

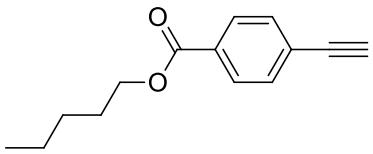

To a solution of methyl 4-ethynylbenzoate (370 mg, 2.31 mmol) in 1-pentanol (40 mL), methyl 4-ethynylbenzoate (370 mg, 2.31 mmol) was added. The reaction mixture was allowed to stir in an open vessel under nitrogen at 80 °C for 48 hours. The resulting mixture was diluted with hexanes (60 mL), washed with saturated aqueous sodium bicarbonate, deionized water, brine and dried with magnesium sulfate. Volatiles were then removed *in vacuo* and the residue purified by chromatography on silica gel (0-60% CH_2Cl_2/Hexanes) to give the product (yellow oil) in 82% yield. **^{1}H NMR (400MHz, $CDCl_3$, 293K, $CHCl_3$):** 7.98 (2H, d, J=8.2Hz), 7.53 (2H, d, J=8.2Hz), 4.30 (2H, t, J=6.7Hz), 3.22 (1H, s), 1.75 (2H, p, J=7.0Hz), 1.45-1.31 (4H, m), 0.91 (3H, t, J=7.0Hz);

^{13}C NMR (100MHz, $CDCl_3$, 293K, $CHCl_3$): 165.9, 132.0, 130.4, 129.3, 126.5, 82.8, 79.9, 65.3, 28.3, 28.1, 22.3, 13.9; **HRMS** calculated for $C_{14}H_{16}O_2$ (M+H) 217.1229; Found: 217.1226;

2.5.2.2. Dipentyl 4,4'-(buta-1,3-diyne-1,4-diyl)dibenzoate

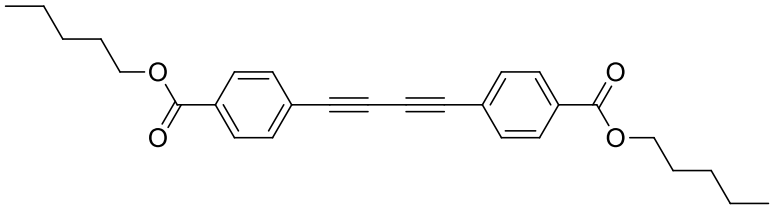

To a solution of pentyl 4-ethynylbenzoate (411 mg, 1.90 mmol), tetramethylethylenediamine (270 µL, 1.90 mmol) and triethylamine (0.82 mL, 5.7 mmol) in acetone (20 mL) was added copper(I) iodide (181 mg, 0.95 mmol). The reaction mixture was allowed to stir at room temperature for 16 hours. Volatiles were then removed *in vacuo* and the residue purified by chromatography on silica gel (30-60% CH_2Cl_2/Hexanes) to

give the product in 82% yield. **^{1}H NMR (400MHz, $CDCl_3$, 293K, $CHCl_3$):** 8.01 (4H, d, J=8.6Hz), 7.59 (4H, d, J=8.6Hz), 4.32 (4H, t, J=6.7Hz), 1.77 (4H, p, 7.0 Hz), 1.47-1.33 (8H, m), 0.93 (6H, t, J=7.0Hz); **^{13}C NMR (100MHz, $CDCl_3$, 293K, $CHCl_3$):** 165.8, 132.4, 130.9, 129.5, 125.9, 81.9, 76.2, 65.5, 28.4, 28.1, 22.3, 14.0; **HRMS** calculated for $C_{28}H_{30}O_4$ (M+H) 431.2222; Found: 431.2201;

2.5.2.3. Methyl 4-((4-(pentyloxy)phenyl)buta-1,3-diyn-1-yl)

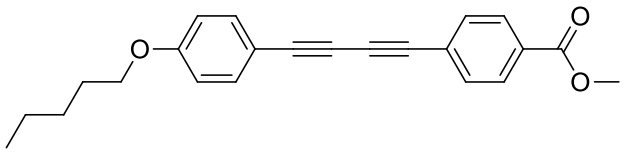

Prepared by a modified previously described procedure.[110] To a solution of 4-*n*-Pentyloxyphenylacetylene (2.26 g, 12 mmol) in acetone (80 mL) was added *N*-bromosuccinimide (2.49 g, 14 mmol) and silver nitrate (204 mg, 1.2 mmol) in order. The mixture was stirred at room temperature until the reaction was judged complete by TLC (~2 hours) then poured into ice-water and extracted with hexanes (3x). The extract was washed with water and brine, dried over $MgSO_4$ Upon removal of solvent *in vacuo* crude 1-(bromoethynyl)-4-(pentyloxy)benzene was pure enough for use without further purification. Copper(I) chloride (10 mg, 0.1 mmol) was added to a 30% *n*-$BuNH_2$ aqueous solution (8 mL) at room temperature, which resulted in the formation of a blue solution. A few crystals of hydroxylamine hydrochloride were added to discharge the blue color. Methyl 4-ethynylbenzoate (320 mg, 2 mmol) was then added to the solution and the reaction mixture was cooled with an ice-water bath. 1-(Bromoethynyl)-4-(pentyloxy)benzene (2.4 mmol) in diethyl ether (4 mL) was added dropwise to the cooled reaction mixture. Occasionally adding a small amount of hydroxylamine hydrochloride was necessary to keep the color of the reaction light yellow. After the addition of bromoalkyne, the cooling bath was removed. The reaction mixture was stirred at room temperature for 3 hours during which more crystals of hydroxylamine hydrochloride were added whenever the reaction mixture started to turn blue or green. The reaction mixture was diluted with EtOAc then washed with 1 M HCl, water and brine. The combined organic layer was dried over $MgSO_4$ and concentrated under reduced pressure. The residue was purified by chromatography on silica gel (50% CH_2Cl_2/Hexanes) to give

the product in 81% yield. It should be noted the product co-spots with methyl 4-ethynylbenzoate using this eluent but they can be differentiated because the product stains significantly faster with CAM (ceric ammonium molybdate) stain than does methyl 4-ethynylbenzoate. **^{1}H NMR (400MHz, $CDCl_3$, 293K, $CHCl_3$):** 8.00 (2H, d, J=8.6Hz), 7.56 (2H, d, J=8.6Hz), 7.46 (2H, d, J=8.9Hz), 6.85 (2H, d, J=8.9Hz), 3.97 (2H, t, J=6.6Hz), 3.92 (3H, s), 1.79 (2H, p, 6.6 Hz), 1.33-1.49 (4H, m), 0.93 (3H, t, J=7.1Hz); **^{13}C NMR (100MHz, $CDCl_3$, 293K, $CHCl_3$):** 166.3, 160.2, 134.2, 132.3, 130.0, 129.5, 126.8, 114.7, 113.0, 83.6, 80.0, 77.1, 72.4, 68.1, 52.275, 28.8, 28.1, 22.4, 14.0; **HRMS** calculated for $C_{23}H_{22}O_3$ (M+H) 347.1642; Found: 347.1649;

2.5.2.4. 4-((4-Pentylphenyl)buta-1,3-diyn-1-yl)benzonitrile

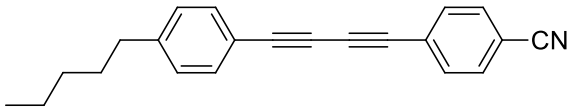

To a solution of 4-*n*-Pentylphenylacetylene (3.89 mL, 20 mmol), 4-ethynylbenzonitrile (254 mg, 2 mmol), tetramethylethylenediamine (60 µL, 0.4 mmol) and triethylamine (838 µL, 6 mmol) in acetone (10 mL) was added copper(I) iodide (38 mg, 0.2mmol). The reaction mixture was allowed to stir at room temperature for 16 hours. Volatiles were then removed *in vacuo* and the residue purified by chromatography on silica gel (0-60% CH_2Cl_2/Hexanes) to give the product in 70% yield. Spectral data corresponds to that previously described in the literature.[111]

2.5.2.5. 4-((4-(pentyloxy)phenyl)buta-1,3-diyn-1-yl)benzonitrile

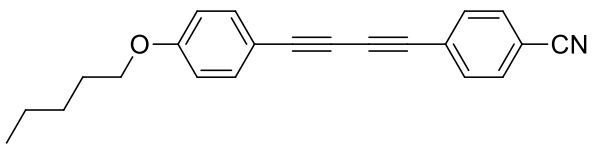

Prepared by a modified previously described procedure.[110] To a solution of 4-*n*-Pentyloxyphenylacetylene (2.26 g, 12 mmol) in acetone (80 mL) was added *N*-bromosuccinimide (2.49 g, 14 mmol) and silver nitrate (204 mg, 1.2 mmol) in order. The mixture was stirred at room temperature until the reaction was judged

complete by TLC (~2 hours) then poured into ice-water and extracted with hexanes (3x). The extract was washed with water and brine, dried over $MgSO_4$ Upon removal of solvent *in vacuo* crude 1-(bromoethynyl)-4-(pentyloxy)benzene was pure enough for use without further purification. Copper(I) chloride (10 mg, 0.1 mmol) was added to a 30% *n*-$BuNH_2$ aqueous solution (8 mL) at room temperature, which resulted in the formation of a blue solution. A few crystals of hydroxylamine hydrochloride were added to discharge the blue color. 4-Ethynylbenzonitrile (254 mg, 2 mmol) was then added to the solution and the reaction mixture was cooled with an ice-water bath. 1-(Bromoethynyl)-4-(pentyloxy)benzene (2.4 mmol) in diethyl ether (4 mL) was added dropwise to the cooled reaction mixture. Occasionally adding a small amount of hydroxylamine hydrochloride was necessary to keep the color of the reaction light yellow. After the addition of bromoalkyne, the cooling bath was removed. The reaction mixture was stirred at room temperature for 3 hours during which more crystals of hydroxylamine hydrochloride were added whenever the reaction mixture started to turn blue or green. The reaction mixture was diluted with EtOAc then washed with 1 M HCl, water and brine. The combined organic layer was dried over $MgSO_4$ and concentrated under reduced pressure. The residue was purified by chromatography on silica gel (30-50% CH_2Cl_2/Hexanes) to give the product in 76% yield. **^{1}H NMR (400MHz, $CDCl_3$, 293K, $CHCl_3$):** 7.62 (2H, d, J=8.6Hz), 7.58 (2H, d, J=8.6Hz), 7.47 (2H, d, J=8.9Hz), 6.90 (2H, d, J=8.9Hz), 3.97 (2H, t, J=6.6Hz), 1.79 (2H, p, J=6.6Hz), 1.49-1.33 (4H, m), 0.93 (3H, t, J=7.1Hz); **^{13}C NMR (100MHz, $CDCl_3$, 293K, $CHCl_3$):** 160.4, 134.3, 132.8, 132.0, 127.1, 118.3, 114.7, 112.7, 112.1, 84.5, 78.9, 78.6, 72.1, 68.2, 28.8, 28.1, 22.4, 14.0; **HRMS** calculated for $C_{22}H_{19}NO$ (M+H) 314.1545; Found: 314.1552;

2.5.2.6. (2E,2'E)-Bis(2-ethylhexyl)3,3'-(buta-1,3-diyne-1,4-diylbis(4,1-phenylene))bis(2-cyanoacrylate)

To a solution of 4,4'-(buta-1,3-diyne-1,4-diyl)dibenzaldehyde (430 mg, 1.67 mmol, prepared as previously described[112]) and 2-ethylhexyl cyanoacetate (728 µl, 3.5 mmol) in CH_2Cl_2 was added piperidine (33 µl, 0.33 mmol). The resulting solution was stirred at room temperature for 5 hours then concentrated under reduced pressure. The resulting residue was purified by chromatography on silica gel (50-70% CH_2Cl_2/Hexanes) to give the product in 69% yield.

^{1}H NMR (400MHz, $CDCl_3$, 293K, $CHCl_3$): 8.20 (2H, s), 7.98 (4H, d, J=8.3Hz), 7.64 (4H, d, J=8.4Hz), 4.29-4.20 (4H, m), 1.72 (2H, sept, J=6.1Hz), 1.45 (4H, p, J=7.4Hz), 1.40-1.26 (12H, m), 0.94 (6H, t, J=7.4Hz), 0.91 (6H, t, J=6.8Hz);

^{13}C NMR (100MHz, $CDCl_3$, 293K, $CHCl_3$): 162.3, 153.1, 133.2, 132.1, 130.9, 126.2, 115.1, 104.2, 82.5, 77.4, 69.2, 38.7, 30.3, 28.9, 23.7, 22.9, 14.0, 11.0;

HRMS calculated for $C_{40}H_{44}N_2O_4$ ([M+Na]+) 639.3199; Found: 639.3177;

2.5.2.7. 4-((4-(Pentyloxy)phenyl)buta-1,3-diyn-1-yl)benzaldehyde

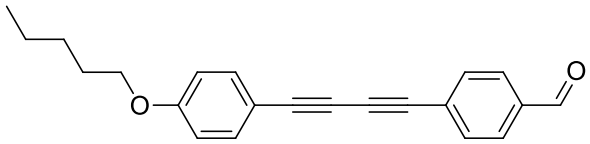

To a solution of 1-ethynyl-4-(pentyloxy)benzene (6.2 mL, 31.5 mmol), 4-ethynylbenzaldehyde (410 mg, 3.15 mmol), tetramethylethylenediamine (94.5 µL, 0.63 mmol) and triethylamine (1.3 mL, 9.45 mmol) in acetone (16 mL) was added copper(I) iodide (60 mg, 0.315 mmol). The reaction mixture was allowed to stir at room temperature for 16 hours. Volatiles were then removed *in vacuo* and the residue purified by chromatography on silica gel (50% CH_2Cl_2/Hexanes) to give the product in 37% yield.

^{1}H NMR (400MHz, $CDCl_3$, 293K, $CHCl_3$): 10.02 (1H, s), 7.84 (2H, d, J=8.4Hz), 7.65 (2H, d, J=8.2Hz), 7.47 (2H, d, J=8.9Hz), 6.86 (2H, d, J=8.9Hz), 3.97 (2H, t, J=6.6Hz), 1.80 (2H, p, 7.0Hz), 1.49-1.33 (4H, m), 0.94 (3H, t, J=7.1Hz);

^{13}C NMR (100MHz, $CDCl_3$, 293K, $CHCl_3$): 191.1, 160.3, 135.8, 134.3, 132.9, 129.5, 128.4, 114.8, 112.9, 84.3, 79.8, 78.2, 72.3, 68.2, 28.8, 28.1, 22.4, 14.0;

HRMS calculated for $C_{22}H_{20}O_2$ ([M+H]+) 317.1542; Found: 317.1555;

2.5.2.8. 2-(4-((4-(Pentyloxy)phenyl)buta-1,3-diyn-1-yl)benzylidene)malononitrile

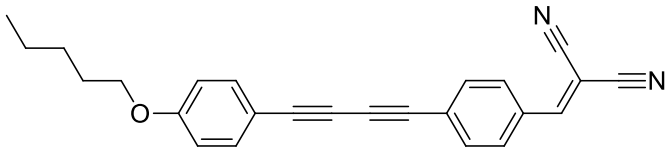

To a solution of 4-((4-(pentyloxy)phenyl)buta-1,3-diyn-1-yl)benzaldehyde (323 mg, 1.02 mmol) and malononitrile (74.2 mg, 1.12 mmol) in dichloromethane (5 mL), piperidine (20.2 µL, 0.204 mmol) was added. The reaction mixture was allowed to stir at room temperature for 1 hour. Volatiles were then removed *in vacuo* and the residue purified by chromatography on silica gel (50-100% CH_2Cl_2/Hexanes) to give the product in 97% yield.

^{1}H NMR (400MHz, $CDCl_3$, 293K, $CHCl_3$): 7.87 (2H, d, J=8.5Hz), 7.72 (1H, s), 7.63 (2H, d, J=8.4Hz), 7.47 (2H, d, J=8.7Hz), 6.86 (2H, d, J=8.7Hz), 3.98 (2H, t, J=6.6Hz), 1.80 (2H, p, J=6.9Hz), 1.49-1.33 (4H, m), 0.94 (3H, t, J=7.0Hz);

^{13}C NMR (100MHz, $CDCl_3$, 293K, $CHCl_3$): 160.5, 158.2, 134.3, 133.2, 130.7, 130.6, 128.8, 114.8, 113.6, 112.7, 112.4, 85.4, 83.3, 79.9, 79.5, 72.3, 68.2, 28.8, 28.1, 22.4, 14.0;

HRMS calculated for $C_{25}H_{20}N_2O$ ([M+H]+) 365.1654; Found: 365.1655;

Addition of sulfur to diphenyldiacetylenes and the other derivatives yields corresponding dithiolodithiole (C_4S_4) compounds which are generally highly colored and have R_f values that are slightly smaller than those of the parent diacetylenes. While most C_4S_4 derivatives are easily purified by flash chromatography there are examples of the crude reaction mixture containing small amounts of co-eluting and electrochemically active impurities which are most likely polysulfide heterocycles (*vide infra*). Analytically pure samples can be obtained by with the aid triphenylphosphine which reacts with the impurities to form triphenylphosphine sulfide as follows: The product mixture is dissolved in dichloromethane (0.25 M). To the resulting solution, 3 equivalents of triphenylphosphine are added. The reaction is then stirred at room

temperature for 2 hours. The reaction is then concentrated under reduced pressure and the resulting residue purified by chromatography on silica gel.

2.5.3. Preparation and Characterization of Dithiolodithiole Derivatives

2.5.3.1. 3,6-Diphenyl-[1,2]dithiolo[4,3-c][1,2]dithiole (1)

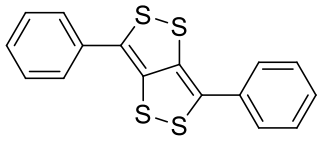

1,4-Diphenylbutadiyne (202 mg, 1 mmol) and elemental sulfur (641 mg, 20 mmol) were charged into a pressure vessel which was heated at 140 °C for 16 hours. The reaction was cooled and the resulting residue was purified by chromatography on silica gel (0-30% CH_2Cl_2/hexanes) to give the product in 66% yield. A large scale procedure was also performed: 1,4-diphenylbutadiyne (1.414 g, 17 mmol), elemental sulfur (2.24 g, 70 mmol) and TEMPO (2,2,6,6-tetramethyl-1-piperidinyloxy, 218 mg, 1.4 mmol) were charged into a pressure vessel which was heated at 130 °C for 16 hours. The reaction was cooled and the resulting residue was purified by chromatography on silica gel (0-30% CH_2Cl_2/hexanes) to give the product in 50% yield. An analytically pure sample was obtained via purification by reaction with triphenylphosphine (*vide supra*). Suitable crystals for single crystal x-ray crystallography were grown by slow evaporation of a CH_2Cl_2 solution in a non-stick coated vial.[113]

^{1}H NMR (400MHz, $CDCl_3$, 293K, $CHCl_3$): 7.50-7.45 (4H, m), 7.44-7.39 (4H, m), 7.34-7.29 (2H, m);

^{13}C NMR (100MHz, $CDCl_3$, 293K, $CHCl_3$): 138.6, 132.6, 129.0, 128.4, 125.9, 123.0;

HRMS calculated for $C_{16}H_{10}S_4$ (M+) 329.9665; Found: 329.9667;

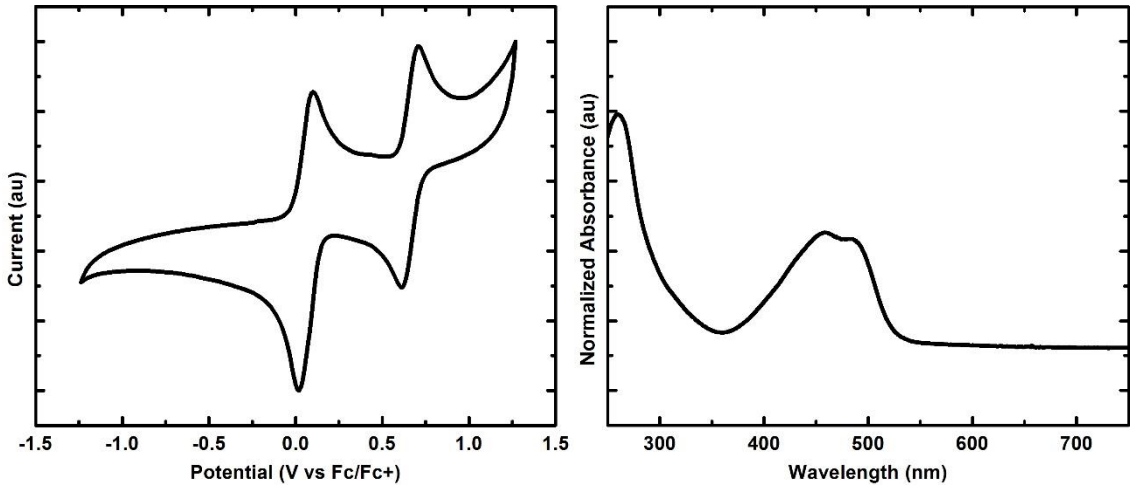

2.5.3.2. 3,6-Bis(4-fluorophenyl)-[1,2]dithiolo[4,3-c][1,2]dithiole (2)

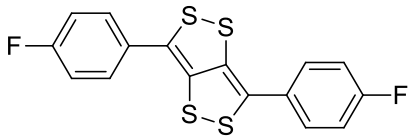

1,4-Bis(4-fluorophenyl)buta-1,3-diyne (238 mg, 1.0 mmol, prepared as previously described[114]), elemental sulfur (321 mg, 10 mmol) and bis(3,5-dichlorophenyl) disulfide (71 mg, 0.4 mmol) were charged into a pressure vessel which was heated at 140 °C for 16 hours. The reaction was cooled and the resulting residue was purified by chromatography on silica gel (0-20% CH_2Cl_2/hexanes) to give the product in 64% yield. An analytically pure sample was obtained via purification by reaction with triphenylphosphine (*vide supra*). Suitable crystals for single crystal x-ray crystallography were grown by slow evaporation of a CH_2Cl_2 solution in a non-stick coated vial.[113]

^{1}H NMR (400MHz, $CDCl_3$, 293K, $CHCl_3$): 7.49-7.43 (4H, m), 7.14-7.07 (4H, m);

^{13}C NMR (100MHz, $CDCl_3$, 293K, $CHCl_3$): 162.1 (d, J=250.7Hz), 138.3, 128.6 (d, J=3.5Hz), 128.0 (d, J=8.2Hz), 122.0, 116.2 (d, J=22.0Hz);

HRMS calculated for $C_{16}H_8F_2S_4$ (M+) 365.9477; Found: 365.9468;

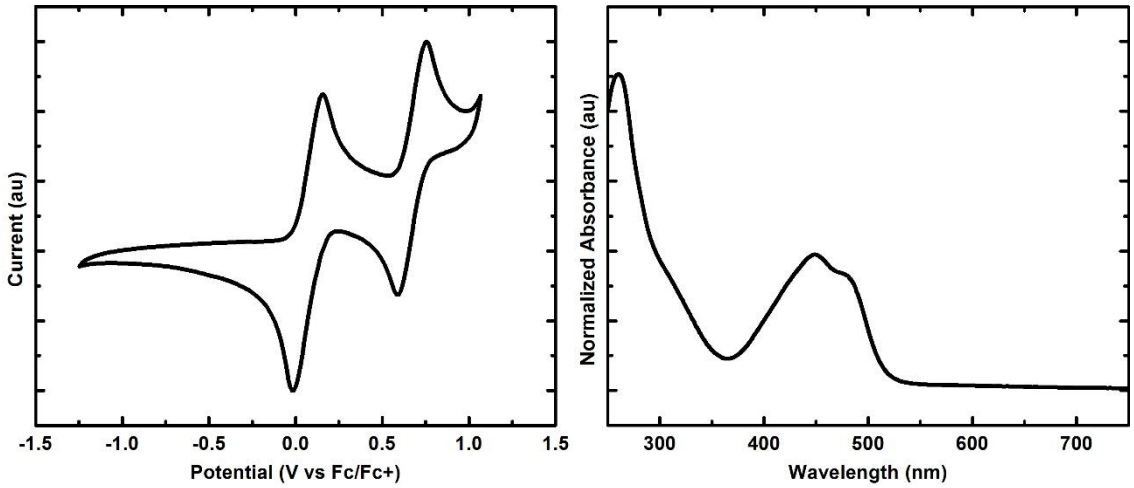

2.5.3.3. 3,6-Bis(4-bromophenyl)-[1,2]dithiolo[4,3-c][1,2]dithiole (3)

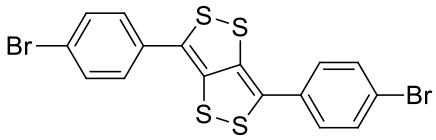

1,4-Bis(4-bromophenyl)buta-1,3-diyne (612 mg, 1.7 mmol, prepared as previously described[115]) and elemental sulfur (1.09 g, 34 mmol) were charged into a pressure vessel which was heated at 145 °C for 16 hours. The reaction was cooled and the resulting residue was purified by chromatography on silica gel (0-20% CH_2Cl_2/Hexanes) to give the product in 17% yield. An analytically pure sample was obtained via purification by reaction with triphenylphosphine (*vide supra*).

^{1}H NMR (400MHz, $CDCl_3$, 293K, $CHCl_3$): 7.54 (4H, d, J=8.6Hz), 7.33 (4H, d, J=8.6Hz);

^{13}C NMR (150MHz, $CDCl_3$, 293K, $CHCl_3$): 147.1, 138.4, 131.9, 131.5, 131.2, 123.9;

HRMS calculated for $C_{16}H_8Br_2S_4$ (M+) 485.7876; Found: 485.7888;

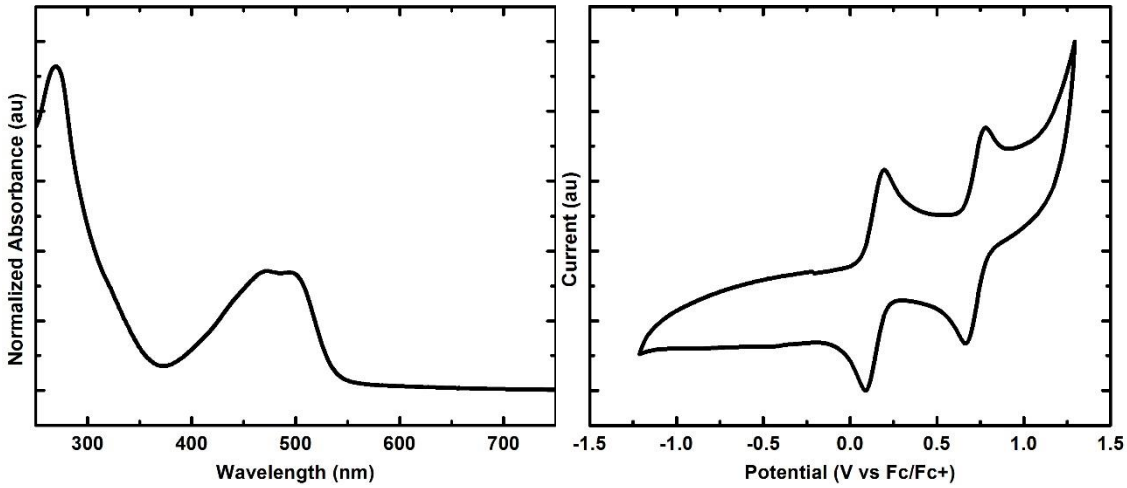

2.5.3.4. 3,6-Bis(4-pentylphenyl)-[1,2]dithiolo[4,3-c][1,2]dithiole (4)

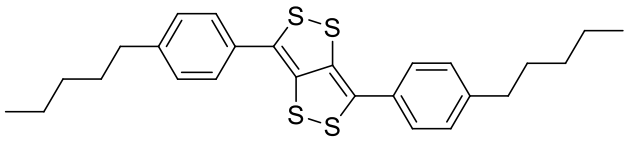

1,4-Bis(4-pentylphenyl)buta-1,3-diyne (171 mg, 0.5 mmol, prepared as previously described[116]) and elemental sulfur (321 mg, 10 mmol) were charged into a pressure vessel which was heated at 145 °C for 16 hours. The reaction was cooled and the resulting residue was purified by chromatography on silica gel (100% hexanes) to give the product in 51% yield.

^{1}H NMR (400MHz, $CDCl_3$, 293K, $CHCl_3$): 7.44 (4H, d, J=8.2Hz), 7.26 (4H, d, J=8.2Hz), 2.65 (4H, t, J=7.8Hz), 1.71-1.61 (4H, m), 1.4-1.32 (8H, m), 0.91 (6H, t, J=6.9Hz)

^{13}C NMR (100MHz, $CDCl_3$, 293K, $CHCl_3$): 148.4, 144.3, 137.3, 129.9, 129.9, 128.6, 35.7, 31.6, 31.0, 22.5, 14.0;

HRMS calculated for $C_{26}H_{30}S_4$ (M+H) 471.1309; Found: 471.1316;

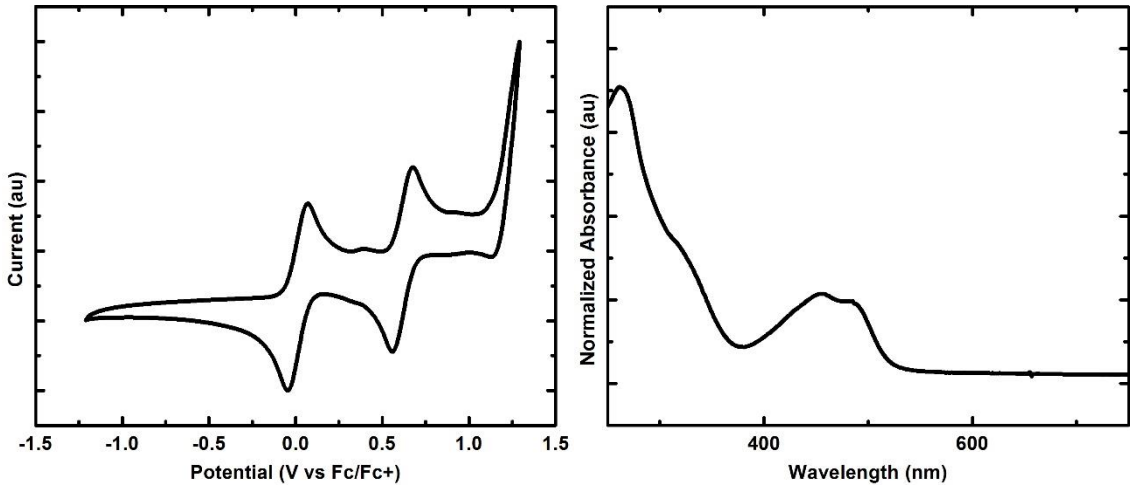

2.5.3.5. 3,6-Di(thiophen-2-yl)-[1,2]dithiolo[4,3-c][1,2]dithiole (5)

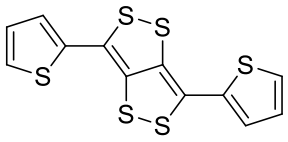

1,4-Di(thiophen-2-yl)buta-1,3-diyne (214 mg, 1.0 mmol, prepared as previously described[114]) and elemental sulfur (641 mg, 20 mmol) were weighed in air and placed in a microwave tube with a magnetic stir bar and capped with a microwave tube cap. The mixture is then placed in a CEM Discover microwave reactor at 170 ºC for 7 hours. The reaction is then concentrated under reduced pressure and the resulting residue purified by chromatography on silica gel (0-10% CH_2Cl_2/Hexanes) to give the product in 21% yield.

^{1}H NMR (400MHz, $CDCl_3$, 293K, $CHCl_3$): 7.42 (2H, dd, J=5.1, 1.2Hz), 7.36 (2H, dd, J=3.7, 1.2Hz), 7.06 (2H, dd, J=5.1, 3.7Hz);

^{13}C NMR (150MHz, $CDCl_3$, 293K, $CHCl_3$): 140.6, 136.7, 133.8, 128.6, 128.4, 127.3;

HRMS calculated for $C_{12}H_6S_6$ (M+) 341.8794; Found: 341.8787;

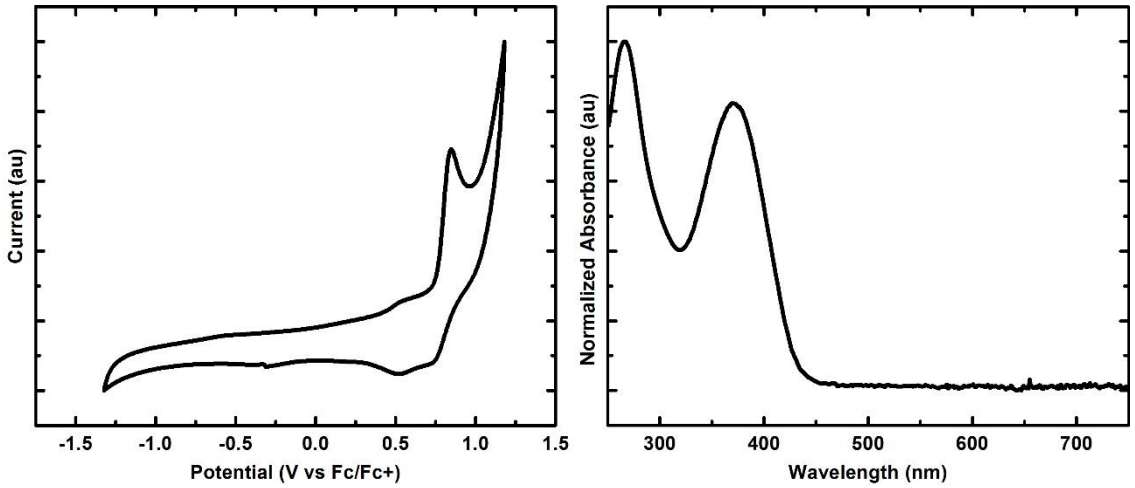

2.5.3.6. 3,6-Dioctyl-[1,2]dithiolo[4,3-c][1,2]dithiole (6)

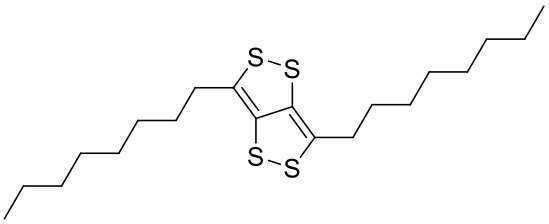

Icosa-9,11-diyne (274 mg, 1.0 mmol, prepared as previously described[114]) and elemental sulfur (641 mg, 20 mmol) were charged into a pressure vessel which was heated at 145 °C for 16 hours. The reaction was cooled and the resulting residue was purified by chromatography on silica gel (100% hexanes) to give the product in 16% yield. No redox events where observed within the solvent window -1.23V to 1.27V with respect to Fc/Fc+ (define solvent window).

^{1}H NMR (400MHz, $CDCl_3$, 293K, $CHCl_3$): 3.02-2.82 (4H, m), 1.66-1.56 (4H, m), 1.40-1.21 (20H, m), 0.88 (6H, t, J=7.0Hz);

^{13}C NMR (100MHz, $CDCl_3$, 293K, $CHCl_3$): 149.4, 136.8, 31.9, 31.8, 29.9, 29.2, 29.1, 29.0, 22.7, 14.1;

HRMS calculated for $C_{20}H_{34}S_4$ (M+) 402.1543; Found: 402.1553;

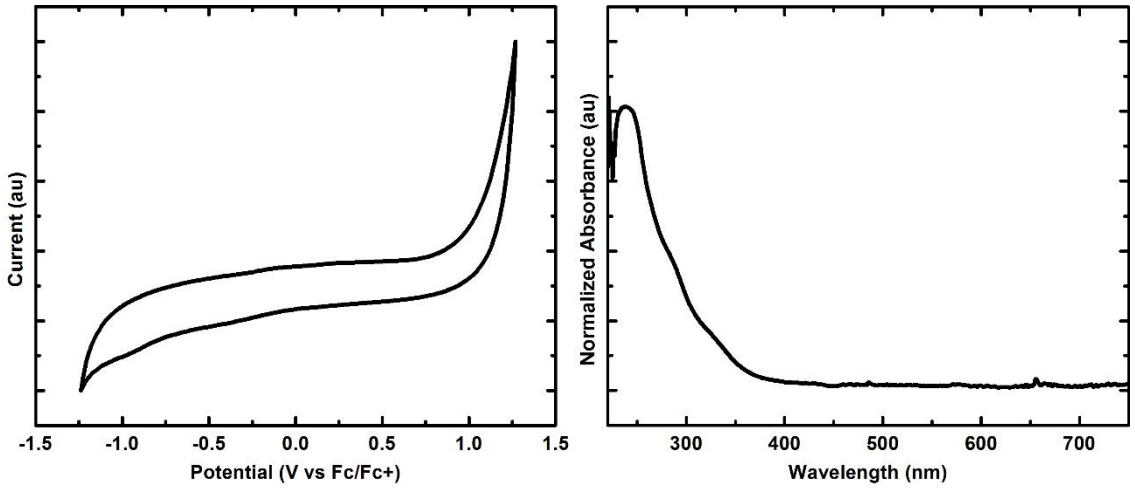

2.5.3.7. 4-(6-(4-Pentylphenyl)-[1,2]dithiolo[4,3-c][1,2]dithiol-3-yl)benzonitrile (7)

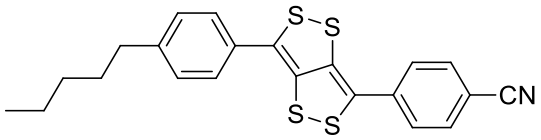

4-((4-Pentylphenyl)buta-1,3-diyn-1-yl)benzonitrile (157 mg, 0.53 mmol), elemental sulfur (160 mg, 5 mmol), bis(3,5-dichlorophenyl) disulfide (53 mg, 0.15 mmol) and 1,2-dichloroethane (2 mL) were placed in a microwave tube with a magnetic stir bar and capped with a microwave tube cap. The mixture is then placed in a CEM Discover microwave reactor at 160 ºC for 1.5 hours. The reaction is then concentrated under reduced pressure and the resulting residue purified by chromatography on silica gel (10-50% CH_2Cl_2/Hexanes) to give the product in 24% yield.

^{1}H NMR (400MHz, $CDCl_3$, 293K, $CHCl_3$): 7.68 (2H, d, J=8.7Hz), 7.53 (2H, d, J=8.7Hz), 7.39 (2H, d, J=8.3Hz), 7.24 (2H, d, J=8.3Hz), 2.62 (2H, t, J=7.7Hz), 1.62 (2H, p, J=7.5Hz), 1.38-1.28 (4H, m), 0.90 (3H, t, J=6.9Hz);

^{13}C NMR (150MHz, $CDCl_3$, 293K, $CHCl_3$): 144.3, 142.7, 137.7, 137.1, 132.6, 129.3, 129.2, 126.0, 125.9, 120.0, 118.5, 110.4, 35.8, 31.4, 30.9, 22.5, 14.0, 1 overlapping signal as one peak is missing even with prolonged scans;

HRMS calculated for $C_{22}H_{19}NS_4$ (M+H) 426.0479; Found: 426.0488;

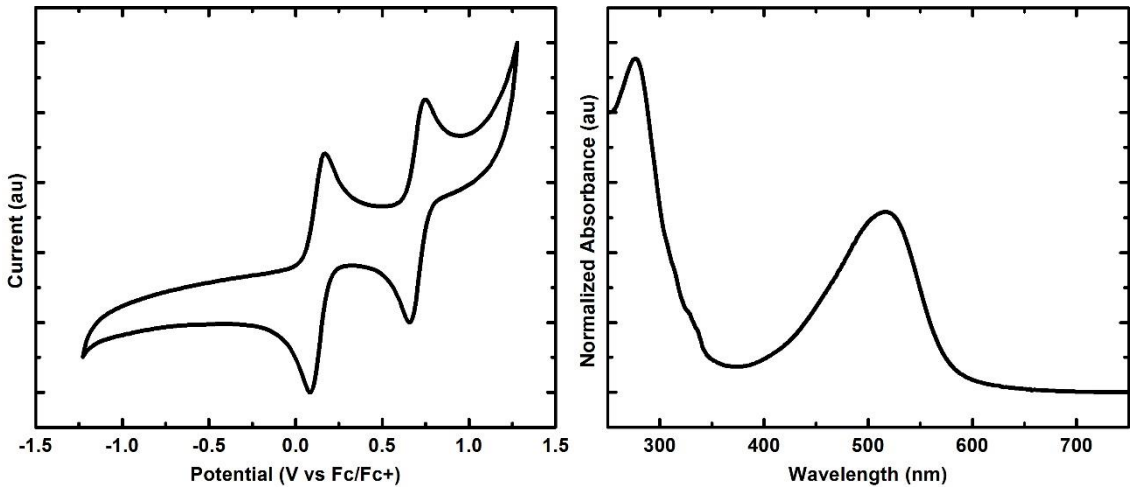

2.5.3.8. 4-(6-(4-(Pentyloxy)phenyl)-[1,2]dithiolo[4,3-c][1,2]dithiol-3-yl)benzonitrile (8)

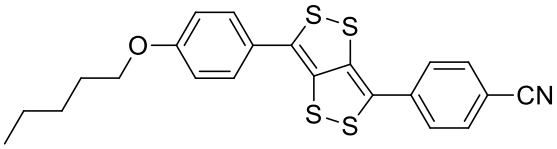

4-((4-(Pentyloxy)phenyl)buta-1,3-diyn-1-yl)benzonitrile (157 mg, 0.5 mmol), elemental sulfur (160 mg, 5 mmol), bis(3,5-dichlorophenyl) disulfide (36 mg, 0.1 mmol) and 1,2-dichloroethane (1 mL) were placed in a microwave tube with a magnetic stir bar and capped with a microwave tube cap. The mixture is then placed in a CEM Discover microwave reactor at 160 ºC for 1.5 hours. The reaction is then concentrated under reduced pressure and the resulting residue purified by chromatography on silica gel (30-50% CH_2Cl_2/Hexanes) to give the product in 23% yield.

^{1}H NMR (400MHz, $CDCl_3$, 293K, $CHCl_3$): 7.67 (2H, d, J=8.4Hz), 7.52 (2H, d, J=8.5Hz), 7.41 (2H, d, J=8.7Hz), 6.93 (2H, d, J=8.7Hz), 3.98 (2H, t, J=6.4Hz), 1.80 (2H, p, J=6.5Hz), 1.33-1.50 (4H, m), 0.94 (3H, t, J=6.6Hz);

^{13}C NMR (100MHz, $CDCl_3$, 293K, $CHCl_3$): 159.6, 137.2, 136.7, 132.56, 127.7, 125.99, 125.96, 125.91, 124.1, 119.6, 118.5, 115.0, 110.4, 68.2, 28.8, 28.1, 22.4, 14.0;

HRMS calculated for $C_{22}H_{19}NOS_4$ (M+H) 442.0422; Found: 442.0426;

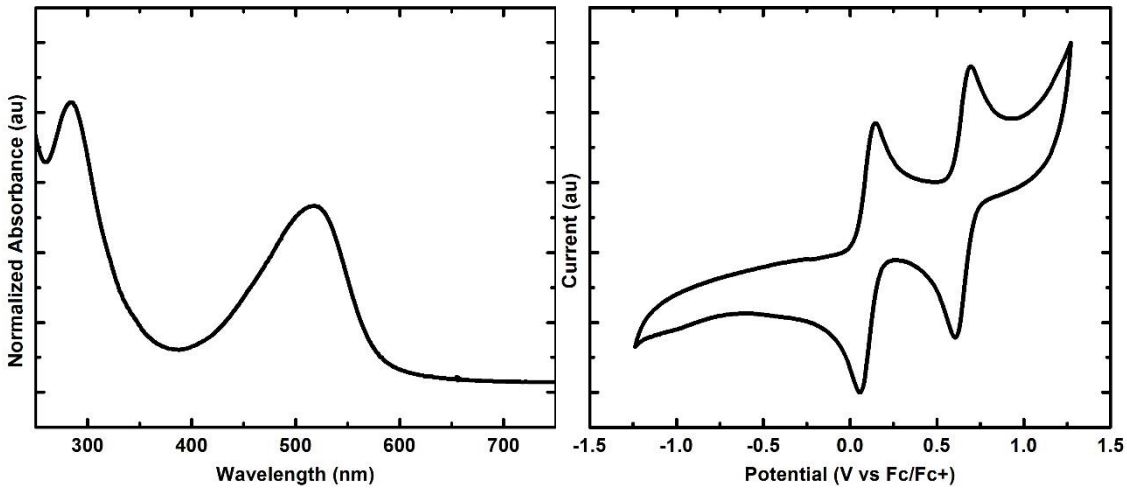

2.5.3.9. Methyl-4-(6-(4-(pentyloxy)phenyl)-[1,2]dithiolo[4,3-c][1,2]dithiol-3-yl)benzoate (9)

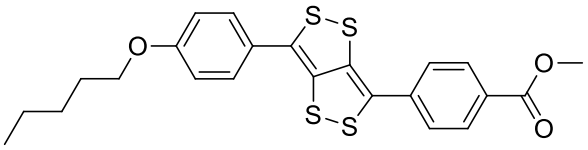

Methyl 4-((4-(pentyloxy)phenyl)buta-1,3-diyn-1-yl)benzoate (173 mg, 0.5 mmol), elemental sulfur (160 mg, 5 mmol), bis(3,5-dichlorophenyl) disulfide (36 mg, 0.1 mmol) and 1,2-dichloroethane (1.5 mL) were placed in a microwave tube with a magnetic stir bar and capped with a microwave tube cap. The mixture is then placed in a CEM Discover microwave reactor at 160 ºC for 1 hour. The reaction is then concentrated under reduced pressure and the resulting residue purified by chromatography on silica gel (10-50% CH_2Cl_2/Hexanes) to give the product in 23% yield.

^{1}H NMR (400MHz, $CDCl_3$, 293K, $CHCl_3$): 8.05 (2H, d, J=8.6Hz), 7.50 (2H, d, J=8.6Hz), 7.41 (2H, d, J=8.8Hz), 6.92 (2H, d, J=8.8Hz), 3.98 (2H, t, J=6.5Hz), 3.92 (3H, s), 1.80 (2H, p, J=6.9Hz), 1.34-1.49 (4H, m), 0.94 (3H, t, J=7.1Hz);

^{13}C NMR (100MHz, $CDCl_3$, 293K, $CHCl_3$): 166.2, 159.4, 141.3, 137.1, 136.9, 130.2, 128.8, 127.6, 125.4, 124.9, 124.4, 120.7, 115.0, 68.2, 52.2, 28.8, 28.1, 22.4, 14.0;

HRMS calculated for $C_{23}H_{22}O_3S_4$ (M+H) 475.0525; Found: 475.0525;

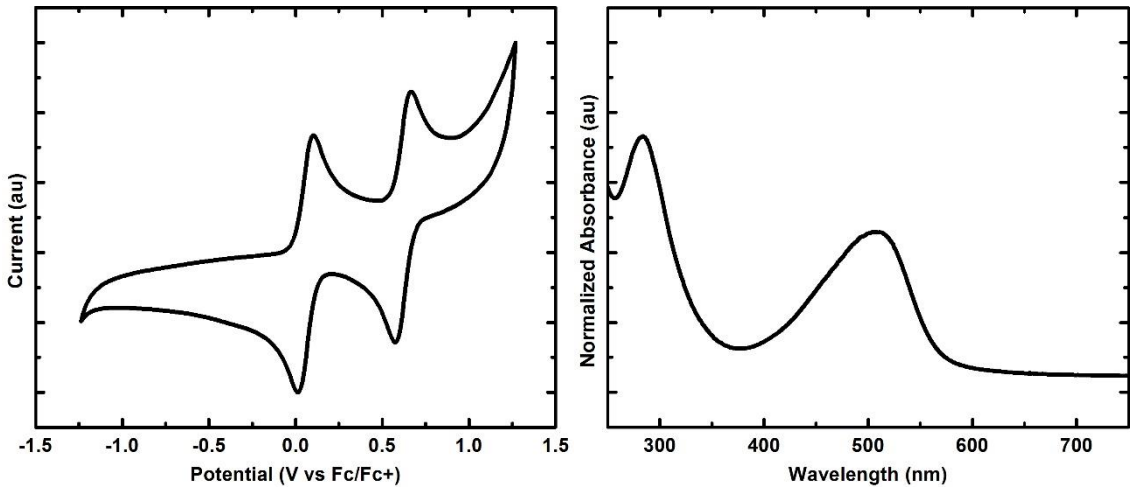

2.5.3.10. Dipentyl 4,4'-([1,2]dithiolo[4,3-c][1,2]dithiole-3,6-diyl)dibenzoate (10)

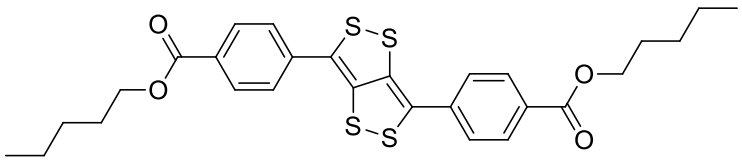

Dipentyl 4,4'-(buta-1,3-diyne-1,4-diyl)dibenzoate (43 mg, 0.1 mmol), elemental sulfur (32 mg, 1 mmol) and bis(3,5-dichlorophenyl) disulfide (11 mg, 0.03 mmol) were charged into a pressure vessel which was heated at 140 °C for 16 hour. The reaction was cooled and the resulting residue was purified by chromatography on silica gel (0-70% CH_2Cl_2/hexanes) to give the product in 21% yield.

^{1}H NMR (400MHz, $CDCl_3$, 293K, $CHCl_3$): 8.08 (4H, d, J=8.7Hz), 7.52 (4H, d, J=8.7Hz), 4.32 (4H, t, J=6.7Hz), 1.78 (4H, p, J=6.8Hz), 1.34-1.48 (8H, m), 0.94 (6H, t, J=7.1Hz);

^{13}C NMR (100MHz, $CDCl_3$, 293K, $CHCl_3$): 165.7, 141.0, 136.6, 130.2, 129.9, 125.7, 123.2, 65.4, 28.4, 28.2, 22.4, 14.0,

HRMS calculated for $C_{28}H_{30}O_4S_4$ (M+H) 558.1027; Found: 558.1039;

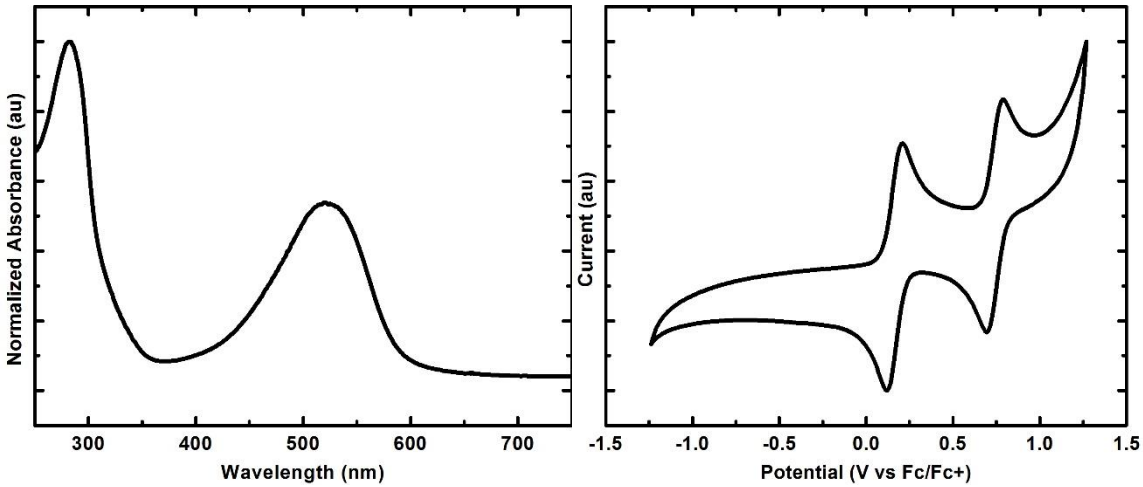

2.5.3.11. 3,6-Bis(4-(4,4,5,5-tetramethyl-1,3,2-dioxaborolan-2-yl)phenyl)-[1,2]dithiolo[4,3-c][1,2]dithiole (11)

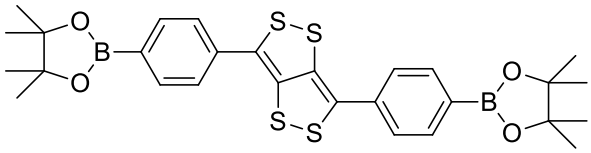

1,4-Bis(4-(4,4,5,5-tetramethyl-1,3,2-dioxaborolan-2-yl)phenyl)buta-1,3-diyne (200 mg, 0.44 mmol, prepared as previously described[117]), elemental sulfur (141 mg, 4.4 mmol), bis(3,5-dichlorophenyl) disulfide (32 mg, 0.09 mmol) and 1,2-dichloroethane (1 mL) were placed in a microwave tube with a magnetic stir bar and capped with a microwave tube cap. The mixture is then placed in a CEM Discover microwave reactor at 160 ºC for 1 hour. The reaction is then concentrated under reduced pressure and the resulting residue purified by chromatography on silica gel (0-80% CH_2Cl_2/Hexanes) to give the product in 11% yield.

^{1}H NMR (400MHz, $CDCl_3$, 293K, $CHCl_3$): 7.90 (4H, d, J=8.2Hz), 7.54 (4H, d, J=8.2Hz), 1.35 (24H, s);

^{13}C NMR (100MHz, $CDCl_3$, 293K, $CHCl_3$): 148.5, 138.2, 135.1, 134.9, 129.3, 128.8, 84.0, 24.9;

HRMS calculated for $C_{28}H_{32}B_2O_4S_4$ (M+H) 583.1448; Found: 583.1453;

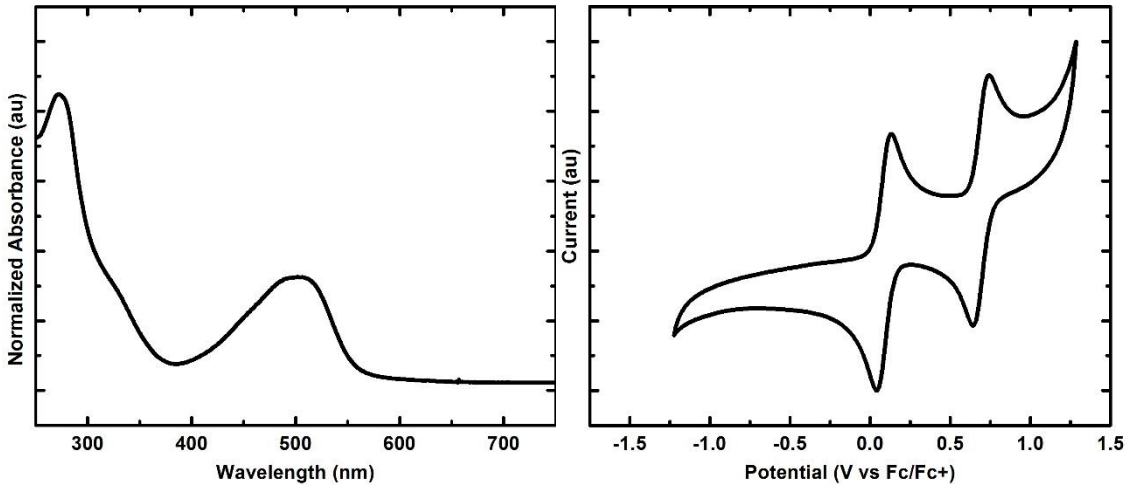

2.5.3.12. (2E,2'E)-Bis(2-ethylhexyl) 3,3'-([1,2]dithiolo[4,3-c][1,2]dithiole-3,6-diylbis(4,1-phenylene))bis(2-cyanoacrylate) (12)

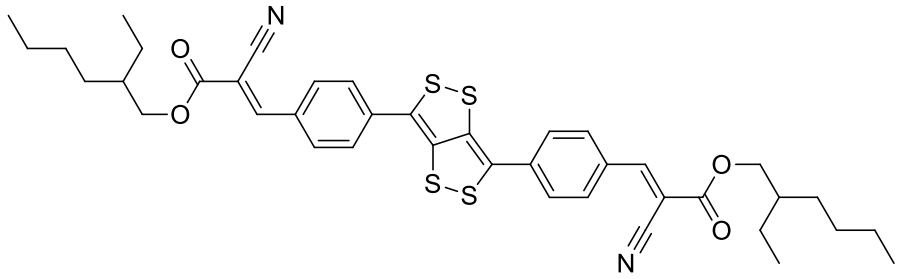

(2E,2'E)-Bis(2-ethylhexyl)3,3'-(buta-1,3-diyne-1,4-diylbis(4,1-phenylene))bis(2-cyanoacrylate) (308 mg, 0.5 mmol), elemental sulfur (160 mg, 5 mmol), bis(3,5-dichlorophenyl) disulfide (36 mg, 0.1 mmol) and 1,2-dichloroethane (2 mL) were placed in a microwave tube with a magnetic stir bar and capped with a microwave tube cap. The mixture is then placed in a CEM Discover microwave reactor at 160 ºC for 1 hour. The reaction is then concentrated under reduced pressure and the resulting residue purified by chromatography on silica gel (60-80% CH_2Cl_2/Hexanes) to give the product in 21% yield. Caution should be taken to neutralize $CDCl_3$ or use alternative solvents as the presence of acid can cause the formation of radical cations (confirmed by EPR and UV experiments with acid titration and spectroelectrochemical measurements) and cause the disappearance of NMR signals. Suitable crystals (needles) for single crystal x-ray crystallography were grown by slow evaporation of a CH_2Cl_2 solution in a non-stick coated vial.[113]

^{1}H NMR (400MHz, CD_2Cl_2, 293K, $CHDCl_2$): 8.19 (2H, s), 8.07 (4H, d, J=8.5Hz), 7.61 (4H, d, J=8.4Hz), 4.28-4.19 (4H, m), 1.72 (2H, sept, J=6.1Hz) 1.50-1.30 (16H, m), 0.95 (6H, t, J=7.5Hz), 0.92 (6H, t, J=7.1Hz);

^{13}C NMR (100MHz, CD_2Cl_2, 293K, $CHDCl_2$): 163.0, 153.2, 143.0, 137.2, 132.2, 131.5, 126.9, 124.3, 116.0, 103.9, 69.6, 39.4, 30.9, 29.5, 24.3, 23.5, 14.4, 11.4;

HRMS calculated for $C_{40}H_{44}N_2O_4S_4$ (M+) 744.2178; Found: 744.2173;

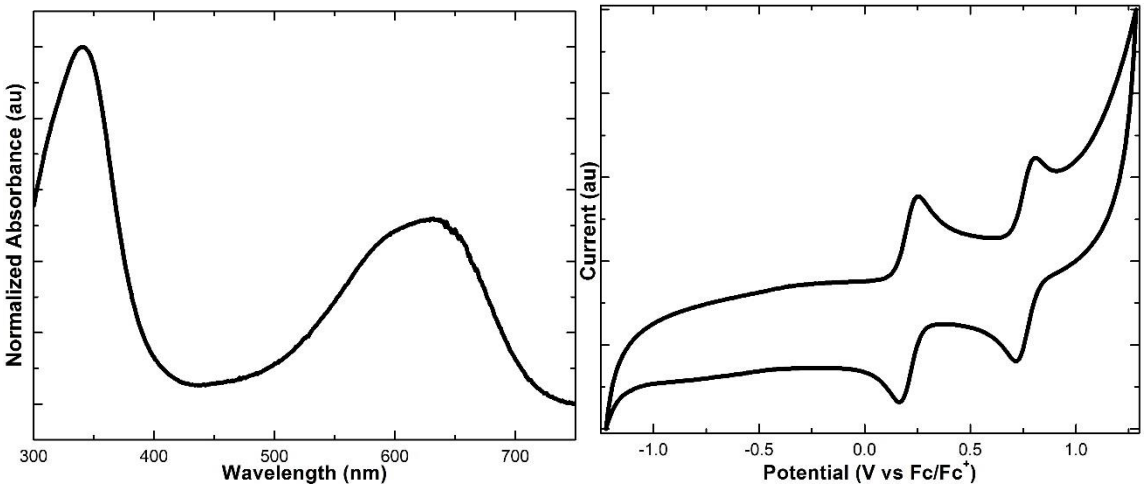

2.5.3.13. 2-(4-(6-(4-(Pentyloxy)phenyl)-[1,2]dithiolo[4,3-c][1,2]dithiol-3-yl)benzylidene)malononitrile (13)

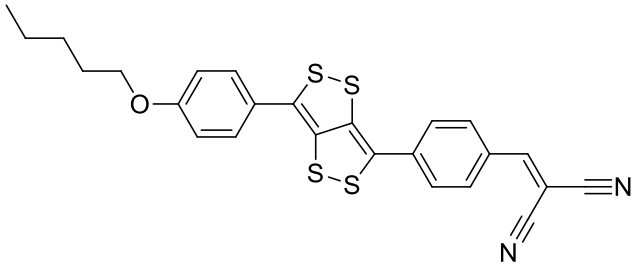

2-(4-((4-(Pentyloxy)phenyl)buta-1,3-diyn-1-yl)benzylidene)malononitrile (182 mg, 0.5 mmol), elemental sulfur (160 mg, 5 mmol), bis(3,5-dichlorophenyl) disulfide (36 mg, 0.1 mmol) and 1,2-dichloroethane (1.5 mL) were placed in a microwave tube with a magnetic stir bar and capped with a microwave tube cap. The

mixture is then placed in a CEM Discover microwave reactor at 160 ºC for 1 hour. The reaction is then concentrated under reduced pressure and the resulting residue purified by chromatography on silica gel (50-80% CH_2Cl_2/Hexanes) to give the product in 27% yield. An EPR experiment (*vide infra*) revealed the presence of some radical character in the ground state or low lying excited sate of the title compound. The radical causes broadening of ^{1}H and disappearance of ^{13}C NMR signals.

^{1}H NMR (400MHz, CD_2Cl_2, 293K, $CHDCl_2$): 7.96 (2H, d, J=9.3Hz), 7.73 (1H, s), 7.56 (2H, d, J=9.0Hz), 7.48-7.40 (2H, m), 6.95(2H, d, J=9.3Hz), 4.00 (2H, m), 1.85-1.73 (2H, m), 1.48-1.35 (4H, m), 0.98-0.90 (3H, m);

HRMS calculated for $C_{25}H_{20}N_2OS_4$ (M+) 492.0458; Found: 492.0477;

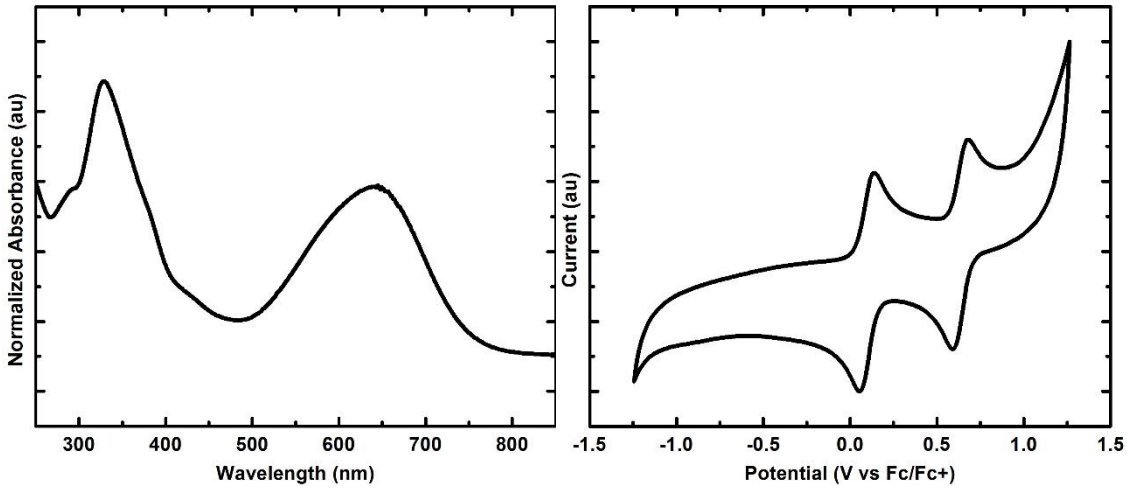

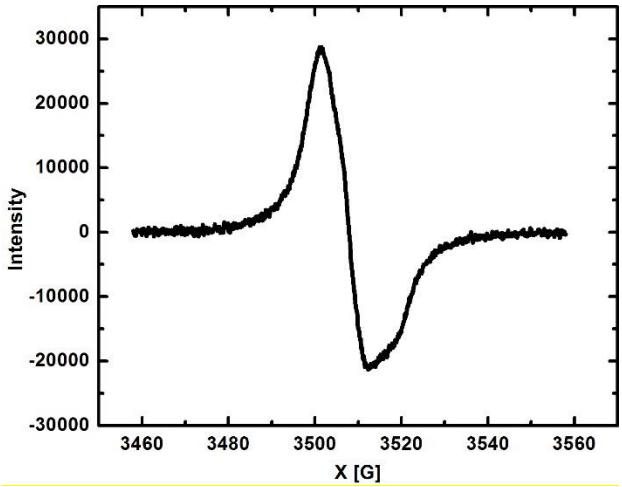

2.5.4. Preparation and Characterization of Thiophene Derivatives

2.5.4.1. 4-(5-(4-Pentylphenyl)thiophen-2-yl)benzonitrile (14)

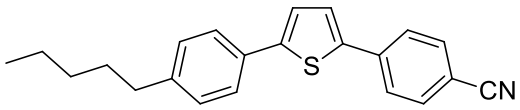

To a solution of 4-((4-pentylphenyl)buta-1,3-diyn-1-yl)benzonitrile (69 mg, 0.22 mmol) in ethanol was added sodium sulfide nonahydrate (58 mg, 0.24 mmol). The reaction was stirred at 50 °C for 16 hours. Volatiles were then removed *in vacuo* and the residue purified by chromatography on silica gel (30-45% CH_2Cl_2/Hexanes) to give the product in 17% yield.

^{1}H NMR (400MHz, $CDCl_3$, 293K, $CHCl_3$): 7.70 (2H, d, J=8.4Hz), 7.65(2H, d, J=8.2Hz), 7.55 (2H, d, J=7.9Hz), 7.39 (1H, d, J=3.8Hz), 7.29 (1H, d, J=3.8Hz), 7.22 (2H, d, J=7.9Hz), 2.63 (2H, t, J=7.7Hz), 1.64 (2H, p, J=7.3Hz), 1.29-1.41 (4H, m), 0.91 (3H, t, J=6.6Hz);

^{13}C NMR (100MHz, $CDCl_3$, 293K, $CHCl_3$): 146.4, 143.3, 140.4, 138.6, 132.7, 131.1, 129.1, 126.0, 125.7, 125.6, 123.9, 118.9, 110.3, 35.6, 31.5, 31.0, 22.5, 14.0;

HRMS calculated for $C_{22}H_{21}NS$ (M+H) 332.1467; Found: 332.1477;

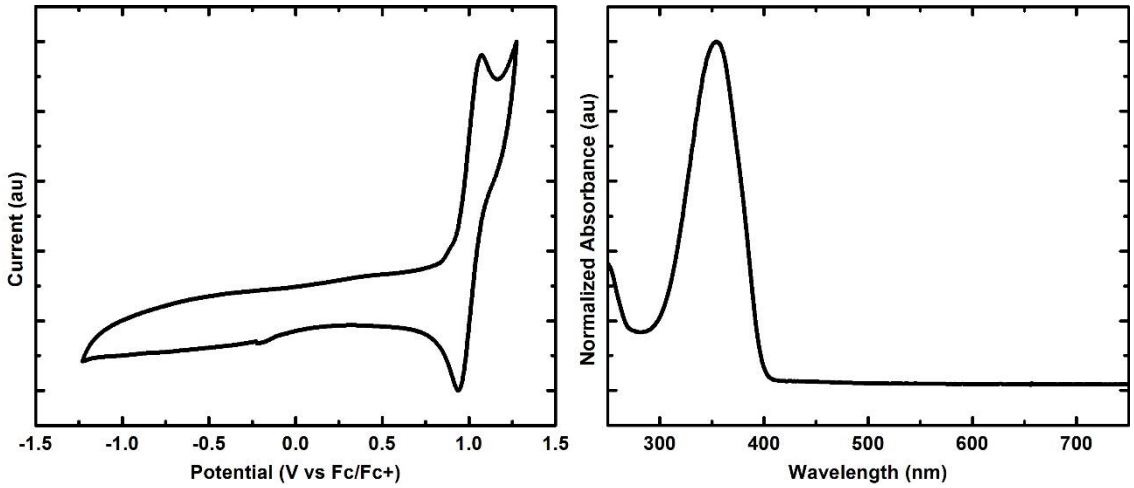

2.5.4.2. Methyl 4-(5-(4-(pentyloxy)phenyl)thiophen-2-yl)benzoate (15)

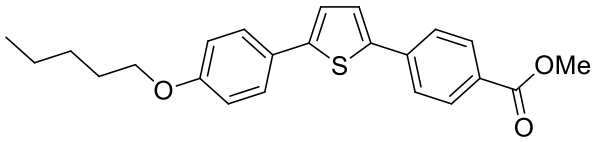

To a solution of methyl 4-((4-(pentyloxy)phenyl)buta-1,3-diyn-1-yl)benzoate (69.3 mg, 0.2 mmol) in a mixture of dichloromethane (1 ml) and methanol (1 ml) was added sodium sulfide nonahydrate (72 mg, 0.3 mmol) and crushed activated 3 Å molecular sieves. The reaction was stirred at 60 °C for 48 hours. Volatiles were then removed in vacuo and the residue purified by chromatography on silica gel (50% CH_2Cl_2/Hexanes) to give the product in 10% yield.

^{1}H NMR (600MHz, $CDCl_3$, 293K, $CHCl_3$): 8.04 (2H, d, J=8.1Hz), 7.67 (2H, d, J=8.1 Hz), 7.55 (2H, d, J=8.4Hz), 7.38 (1H, d, J=3.5Hz), 7.20 (1H, d, J=3.5Hz), 6.92 (2H, d, J=8.4Hz), 3.99 (2H, t, J=6.5Hz), 3.93 (3H, s), 1.81 (2H, p, J=6.8Hz), 1.49-1.36 (4H, m), 0.94 (3H, t, J=7.0Hz);

^{13}C NMR (150MHz, $CDCl_3$, 293K, $CHCl_3$): 167.0, 159.3, 145.6, 141.1, 138.9, 130.5, 128.6, 127.2, 126.8, 125.7, 125.2, 123.3, 115.1, 68.3, 52.4, 29.2, 28.4, 22.7, 14.3;

HRMS calculated for $C_{23}H_{24}O_3S$ (M+H) 381.1524; Found: 381.1534;

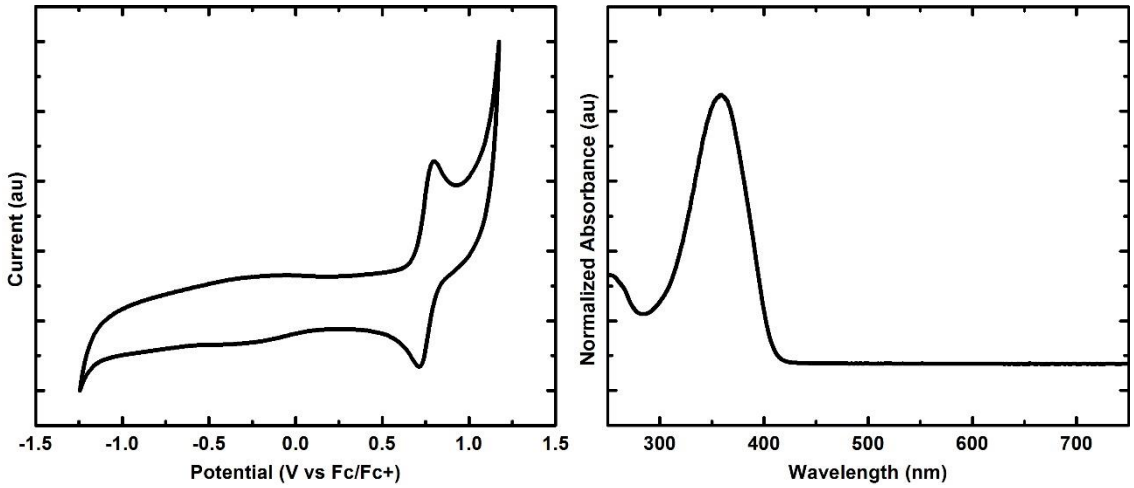

2.5.4.3. Dipentyl 4,4'-(thiophene-2,5-diyl)dibenzoate (16)

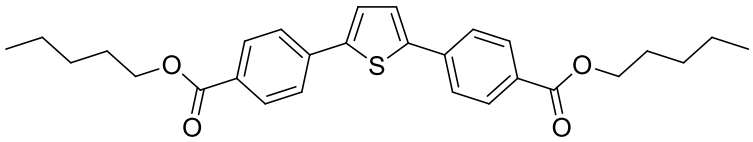

To a solution of dipentyl 4,4'-(buta-1,3-diyne-1,4-diyl)dibenzoate (129 mg, 0.3 mmol) in pentanol was added sodium sulfide nonahydrate (82.4 mg, 0.34 mmol) and crushed activated 3 Å molecular sieves (500 mg). The reaction was stirred at 60 °C for 16 hours. Volatiles were then removed *in vacuo* and the residue purified by chromatography on silica gel (30-45% CH_2Cl_2/Hexanes) to give the product in 23% yield.

^{1}H NMR (400MHz, $CDCl_3$, 293K, $CHCl_3$): 8.06 (4H, d, J=8.6Hz), 7.69 (4H, d, J=8.6Hz), 7.42 (2H, s), 4.33 (4H, t, J=6.7Hz), 1.79 (4H, p, J=7.0Hz), 1.49-1.35 (8H, m), 0.94 (6H, t, J=7.1Hz);

^{13}C NMR (100MHz, $CDCl_3$, 293K, $CHCl_3$): 166.2, 143.7, 138.1, 130.3, 129.5, 125.6, 125.3, 65.2, 28.4, 28.2, 22.4, 14.0;

HRMS calculated for $C_{28}H_{32}O_4S$ (M+H) 465.2100; Found: 465.2073;

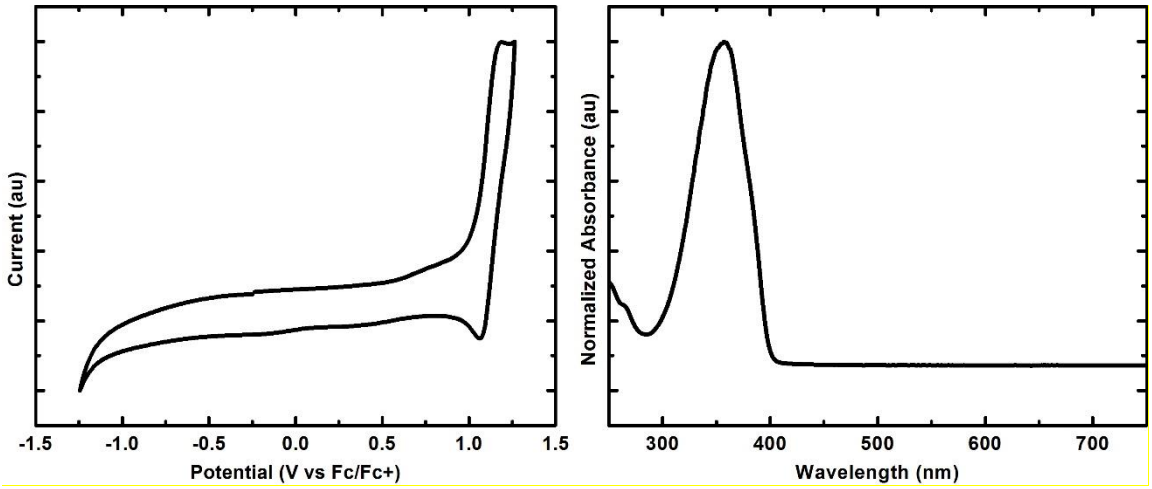

2.5.5. Preparation and Characterization of 6,8-Bis(4-methoxyphenyl)thieno[3,4-f][1,2,3,4,5]pentathiepine

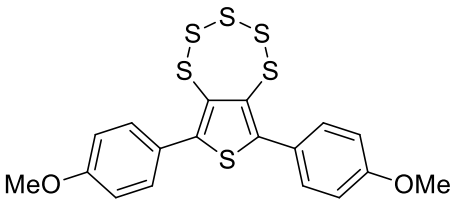

1,4-Bis(4-methoxyphenyl)buta-1,3-diyne (393 mg, 1.5 mmol), prepared as previously described[114]), elemental sulfur (962 mg, 30 mmol), bis(3,5-dichlorophenyl) disulfide (197 mg, 0.9 mmol) and 1,2-dichloroethane (3 mL) were placed in a microwave tube with a magnetic stir bar and capped with a microwave tube cap. The mixture is then placed in a CEM Discover microwave reactor at 160 ºC for 1 hour. The reaction is then filtered through a celite pad (washing with CH_2Cl_2) and the filtrate concentrated under reduced pressure. The resulting residue is then purified by chromatography on silica gel (0-60% CH_2Cl_2/Hexanes) to give a complex mixture of co-eluting products (310 mg) as demonstrated by NMR, TLC (visualizing with various techniques, *vide infra*) and differential pulse voltammetry. The differential pulse voltammogram is shown below along with hypothesized structures of the corresponding peaks.

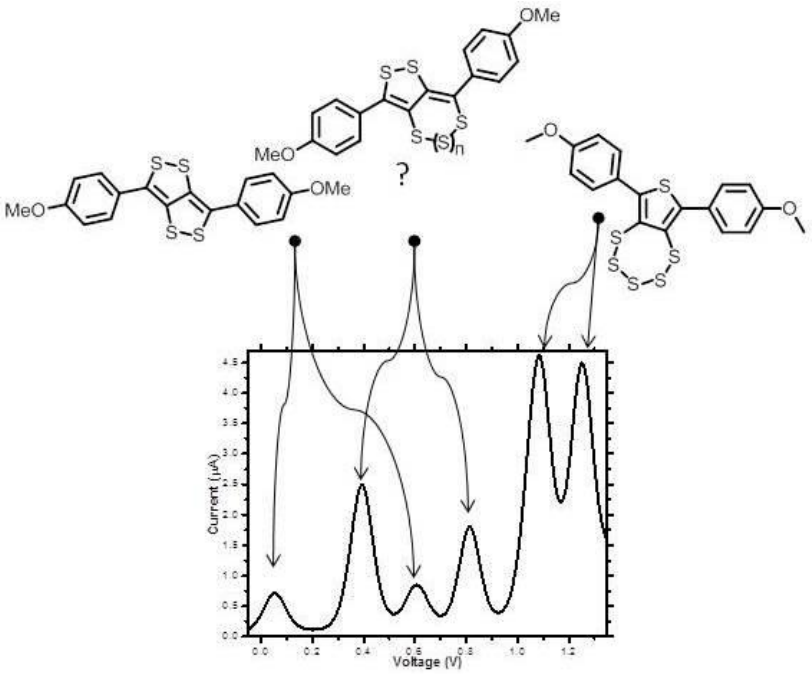

The first and third peaks in the voltammogram are likely to correspond to the C_4S_4 derivative because the redox potentials would be consistent with the the rest of the C_4S_4 compounds that have been synthesized. Since the title compound has been isolated and characterized the fifth and six peaks of the voltammogram can be assigned to the title compound. The second and fourth peaks are assigned to a structure that is hypothesized to possibly resemble a C_4S_4 derivative with extra sulfurs on one or both sides of the central, fused, sulfur-containing heterocycle. This hypothesis is based on the title compound containing many sulfur atoms in one cycle and the fact that this impurity can react with triphenylphosphine to give triphenylphosphine sulfide (*vide supra*). The complex mixture (39 mg) was dissolved in CH_2Cl_2 (3 mL). Upon addition silver hexafluorophosphate (34 mg, 0.13 mmol) the solution immediately turned green and metallic silver plated out. The reaction was allowed to stir at room temperature for 10 minutes. TLC analysis revealed that two of the three components of the mixture had been oxidized leaving the component with the highest oxidation potential unreacted.

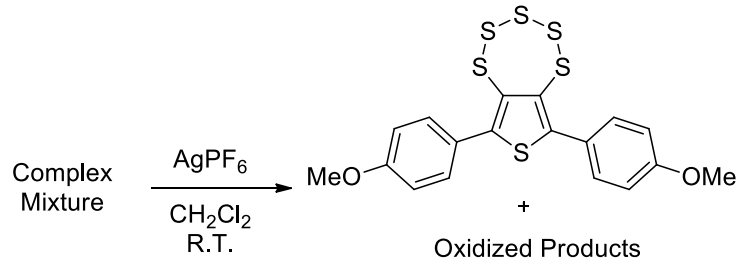
Complex Mixture
AgPF6
CH2Cl2
R.T.
MeO
OMe
+
Oxidized Products

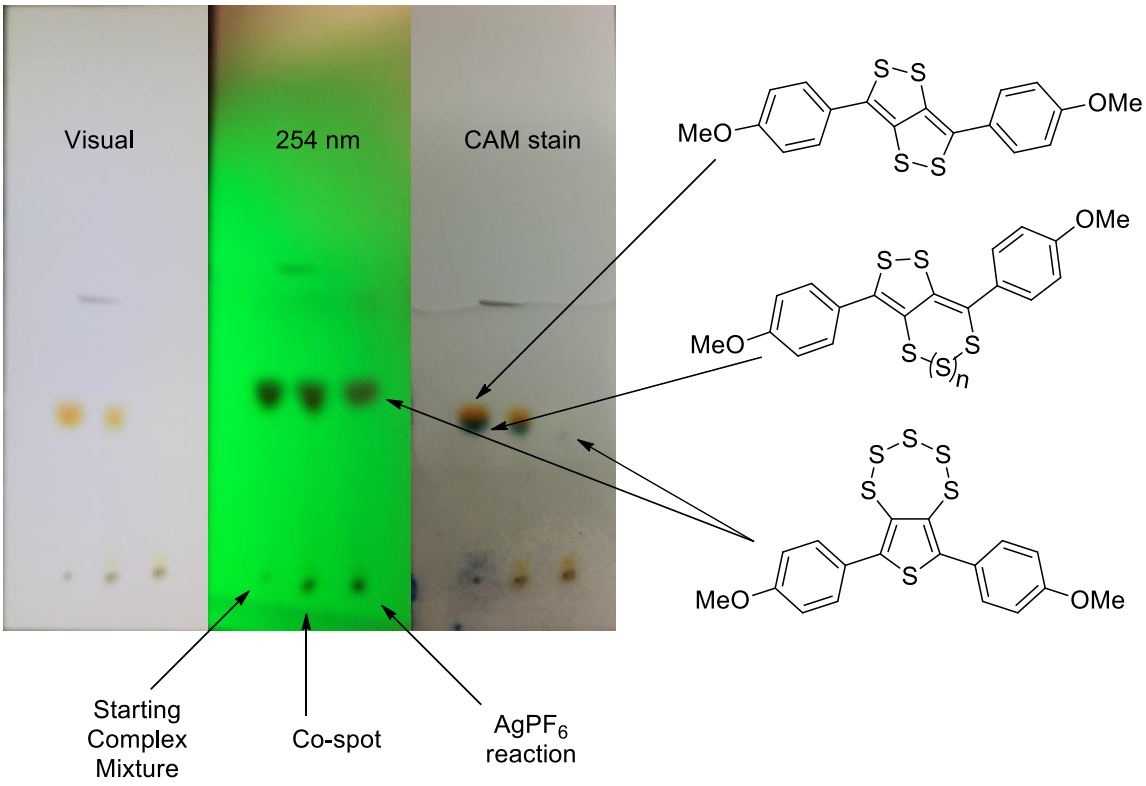
Visual
254 nm
CAM stain
MeO
OMe
MeO
OMe
MeO
OMe
Starting Complex Mixture
Co-spot
AgPF6 reaction

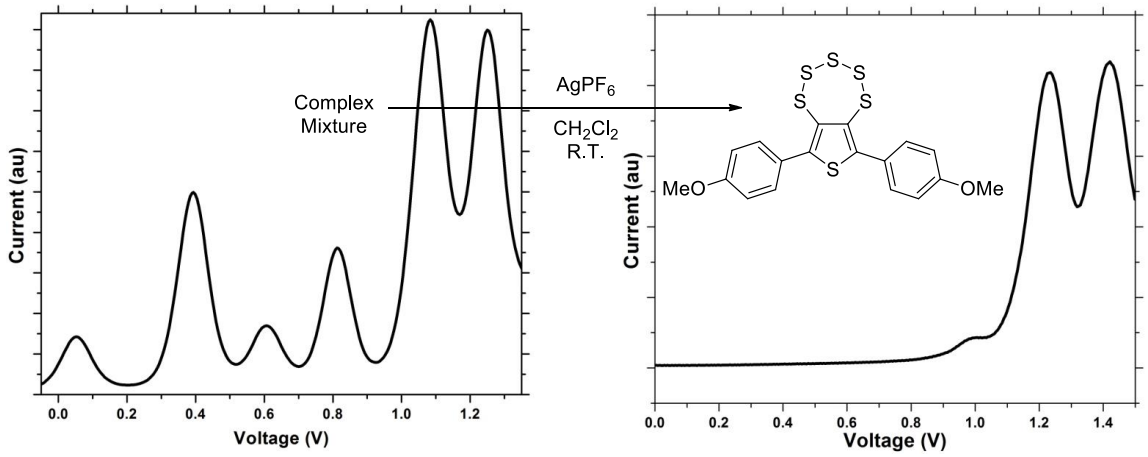

The reaction is then concentrated under reduced pressure and the resulting residue purified by chromatography on silica gel (40-50% CH_2Cl_2/Hexanes) to give the title compound (23 mg). Suitable crystals for single crystal x-ray crystallography were grown by slow evaporation of a CH_2Cl_2 solution in a non-stick coated vial.[113]

^{1}H NMR (400MHz, $CDCl_3$, 293K, $CHCl_3$): 7.47 (4H, d, J=8.7Hz), 6.98 (4H, d, J=8.7Hz), 3.87 (6H, s);

^{13}C NMR (100MHz, $CDCl_3$, 293K, $CHCl_3$): 160.3, 147.9, 137.0, 131.3, 125.0, 114.0, 55.4,;

HRMS calculated for $C_{18}H_{14}O_2S_6$ (M+H) 454.9396; Found: 454.9394;

2.5.6. X-Ray Crystallography Data

Low-temperature diffraction data (φ-and ω-scans) were collected on a Siemens Platform three-circle diffractometer coupled to a Bruker-AXS Smart Apex CCD detector with graphite-monochromated Mo K_α radiation (λ = 0.71073 Å) for the structure of compound **1** and on a Bruker-AXS X8 Kappa Duo diffractometer coupled to a Smart Apex2 CCD detector with Mo K_α radiation (λ = 0.71073 Å), from an IμS micro-source. The structures were solved by direct methods using SHELXS[118] and refined against F^2 on all data by full-matrix least squares with SHELXL[119] following established refinement strategies[120]. All non-hydrogen atoms were refined anisotropically. All hydrogen atoms bound to carbon were included into

the model at geometrically calculated positions and refined using a riding model. The isotropic displacement parameters of all hydrogen atoms were fixed to 1.2 times the U_{eq} value of the atoms they are linked to (1.5 times for methyl groups). Details of the data quality and a summary of the residual values of the refinements are listed in tables S1 to S20.

Compounds **1** and **2** both crystallize in the monoclinic space group $P2_1/c$ with half a molecule of **1** or **2**, respectively, per asymmetric unit. The molecules are completed by one of the space group's crystallographic inversion centers.

Compound **12** crystallizes in the triclinic space group *P*-2 with half a molecule of **12** per asymmetric unit. The molecule is completed by one of the space group's crystallographic inversion centers. The 2-ethylhexyl group in **12** was modeled as disordered over two positions. This disorder was refined with the help of similarity restraints on 1-2 and 1-3 distances and displacement parameters as well as rigid bond restraints for anisotropic displacement parameters. The disorder ratio was refined freely and converged at 0.576(5).

Compound **17** crystallizes in the orthorhombic space group *Pnma* with half a molecule of **17** per asymmetric unit. The molecule is completed by the space group's crystallographic mirror plane, which extends through atoms S1 and S4.

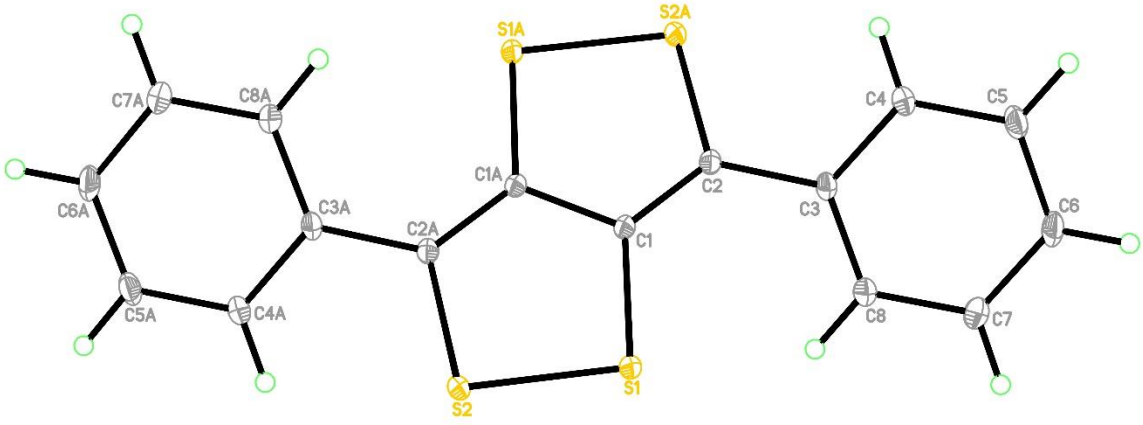

Thermal ellipsoid representation for the crystal structure of compound **1** with atomic labeling scheme. Ellipsoids are drawn at the 50% probability level. The structure contains only half a molecule in the asymmetric unit, the second half of the molecule is generated by a crystallographic inversion center. The figure shows the full molecule; symmetry related atoms are labeled with the letter A in the atom name and are generated by the symmetry operator 1-x, 1-y, 1-z.

Table 1. Crystal data and structure refinement for compound **1**.

Identification code	13018
Empirical formula	C_{16} H_{10} S_4
Formula weight	330.48
Temperature	100(2) K
Wavelength	0.71073 Å
Crystal system	Monoclinic
Space group	$P2_1/c$
Unit cell dimensions	a = 13.7506(18) Å
	b = 7.1690(9) Å
	c = 7.0998(9) Å
Volume	697.39(15) Å^3
Z	2
Density (calculated)	1.574 Mg/m^3
Absorption coefficient	0.665 mm^{-1}
F(000)	340
Crystal size	0.55 x 0.30 x 0.25 mm^3
Theta range for data collection	2.97 to 30.98°.
Index ranges	-19<=h<=19, -10<=k<=10, -10<=l<=10
Reflections collected	19293
Independent reflections	2225 [R_{int} = 0.0349]
Completeness to theta = 30.98°	99.8 %
Absorption correction	Semi-empirical from equivalents
Max. and min. transmission	0.8514 and 0.7112
Refinement method	Full-matrix least-squares on F^2
Data / restraints / parameters	2225 / 0 / 91
Goodness-of-fit on F^2	1.063
Final R indices [$I>2\sigma(I)$]	$R1$ = 0.0281, $wR2$ = 0.0797
R indices (all data)	$R1$ = 0.0295, $wR2$ = 0.0807
Largest diff. peak and hole	0.498 and -0.446 e.Å^{-3}

Table 2. Atomic coordinates (x 10^4) and equivalent isotropic displacement parameters (Å^{2}x 10^3) for compound **1**. U(eq) is defined as one third of the trace of the orthogonalized U^{ij} tensor.

	x	y	z	U(eq)
S(1)	5276(1)	4306(1)	7940(1)	11(1)

S(2)	3757(1)	4327(1)	7593(1)	12(1)
C(1)	5450(1)	4909(1)	5593(1)	9(1)
C(2)	6324(1)	5190(1)	4856(1)	10(1)
C(3)	7312(1)	5112(1)	5801(1)	10(1)
C(4)	8070(1)	6131(2)	5059(2)	13(1)
C(5)	9015(1)	6068(2)	5928(2)	14(1)
C(6)	9232(1)	4986(2)	7543(2)	15(1)
C(7)	8490(1)	3970(2)	8291(2)	16(1)
C(8)	7539(1)	4029(2)	7428(2)	13(1)

Table 3. Bond lengths [Å] and angles [°] for compound **1**.

	Bond lengths [Å]
S(1)-C(1)	1.7572(10)
S(1)-S(2)	2.0836(4)
S(2)-C(2)#1	1.7668(10)
C(1)-C(2)	1.3646(13)
C(1)-C(1)#1	1.4436(18)
C(2)-C(3)	1.4660(13)
C(2)-S(2)#1	1.7668(10)
C(3)-C(8)	1.4050(14)
C(3)-C(4)	1.4100(13)
C(4)-C(5)	1.3912(13)
C(4)-H(4)	0.9500
C(5)-C(6)	1.3955(15)
C(5)-H(5)	0.9500
C(6)-C(7)	1.3948(15)
C(6)-H(6)	0.9500
C(7)-C(8)	1.3963(14)
C(7)-H(7)	0.9500
C(8)-H(8)	0.9500
	Bond angles [°]
C(1)-S(1)-S(2)	95.81(3)
C(2)#1-S(2)-S(1)	95.55(3)
C(2)-C(1)-C(1)#1	120.13(11)
C(2)-C(1)-S(1)	126.48(7)
C(1)#1-C(1)-S(1)	113.39(9)
C(1)-C(2)-C(3)	129.12(9)
C(1)-C(2)-S(2)#1	114.99(7)
C(3)-C(2)-S(2)#1	115.88(7)
C(8)-C(3)-C(4)	118.26(9)
C(8)-C(3)-C(2)	122.06(9)
C(4)-C(3)-C(2)	119.68(9)
C(5)-C(4)-C(3)	120.63(10)
C(5)-C(4)-H(4)	119.7
C(3)-C(4)-H(4)	119.7
C(4)-C(5)-C(6)	120.59(10)
C(4)-C(5)-H(5)	119.7

C(6)-C(5)-H(5)	119.7
C(7)-C(6)-C(5)	119.41(9)
C(7)-C(6)-H(6)	120.3
C(5)-C(6)-H(6)	120.3
C(6)-C(7)-C(8)	120.29(10)
C(6)-C(7)-H(7)	119.9
C(8)-C(7)-H(7)	119.9
C(7)-C(8)-C(3)	120.82(10)
C(7)-C(8)-H(8)	119.6
C(3)-C(8)-H(8)	119.6

Symmetry transformations used to generate equivalent atoms:

#1 -x+1,-y+1,-z+1

Table 4. Anisotropic displacement parameters ($Å^2 x\ 10^3$) for compound **1**. The anisotropic displacement factor exponent takes the form: $-2\pi^2[h^2 a^{*2} U^{11} + ... + 2 h k a^* b^* U^{12}]$

	U^{11}	U^{22}	U^{33}	U^{23}	U^{13}	U^{12}
S(1)	7(1)	16(1)	9(1)	2(1)	1(1)	0(1)
S(2)	7(1)	19(1)	10(1)	3(1)	2(1)	0(1)
C(1)	8(1)	10(1)	8(1)	0(1)	0(1)	0(1)
C(2)	7(1)	12(1)	9(1)	0(1)	0(1)	0(1)
C(3)	7(1)	12(1)	12(1)	-1(1)	0(1)	0(1)
C(4)	8(1)	16(1)	14(1)	1(1)	1(1)	-1(1)
C(5)	7(1)	19(1)	18(1)	0(1)	2(1)	-1(1)
C(6)	8(1)	20(1)	17(1)	-1(1)	-2(1)	1(1)
C(7)	10(1)	21(1)	17(1)	4(1)	-2(1)	2(1)
C(8)	8(1)	16(1)	14(1)	3(1)	0(1)	0(1)

Table 5. Hydrogen coordinates ($x\ 10^4$) and isotropic displacement parameters ($Å^2 x\ 10^3$) for compound **1**.

	x	y	z	U(eq)
H(4)	7934	6867	3956	15
H(5)	9517	6768	5417	17
H(6)	9879	4943	8128	18
H(7)	8632	3234	9393	19
H(8)	7040	3328	7948	16

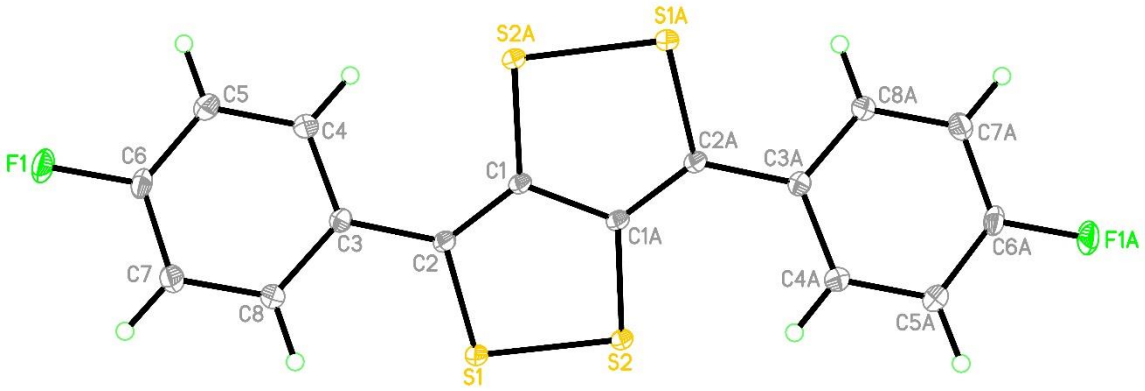

Thermal ellipsoid representation for the crystal structure of compound **2** with atomic labeling scheme. Ellipsoids are drawn at the 50% probability level. The structure contains only half a molecule in the asymmetric unit, the second half of the molecule is generated by a crystallographic inversion center. The figure shows the full molecule; symmetry related atoms are labeled with the letter A in the atom name and are generated by the symmetry operator 2-x, 2-y, 2-z.

Table 6. Crystal data and structure refinement for compound **2**.

Identification code	X8_12058
Empirical formula	C_{16} H_8 F_2 S_4
Formula weight	366.46
Temperature	100(2) K
Wavelength	0.71073 Å
Crystal system	Monoclinic
Space group	$P2_1/c$
Unit cell dimensions	a = 13.987(4) Å
	b = 7.1212(19) Å
	c = 7.1668(19) Å
Volume	713.1(3) Å^3
Z	2
Density (calculated)	1.707 Mg/m^3
Absorption coefficient	0.679 mm^{-1}
F(000)	372
Crystal size	0.35 x 0.25 x 0.20 mm^3
Theta range for data collection	1.46 to 30.85°.
Index ranges	-19<=h<=20, -10<=k<=10, -9<=l<=10
Reflections collected	14051
Independent reflections	2243 [R_{int} = 0.0292]
Completeness to theta = 30.85°	99.9 %
Absorption correction	Semi-empirical from equivalents
Max. and min. transmission	0.8762 and 0.7971

Refinement method	Full-matrix least-squares on F^2
Data / restraints / parameters	2243 / 0 / 100
Goodness-of-fit on F^2	1.043
Final R indices [$I>2\sigma(I)$]	$R1$ = 0.0242, $wR2$ = 0.0661
R indices (all data)	$R1$ = 0.0256, $wR2$ = 0.0670
Largest diff. peak and hole	0.601 and -0.249 e.Å^{-3}

Table 7. Atomic coordinates (x 10^4) and equivalent isotropic displacement parameters (Å^{2}x 10^3) for compound **2**. U(eq) is defined as one third of the trace of the orthogonalized U^{ij} tensor.

	x	y	z	U(eq)
S(1)	8789(1)	10638(1)	12680(1)	12(1)
S(2)	10278(1)	10658(1)	12905(1)	11(1)
F(1)	4991(1)	10132(1)	6996(1)	20(1)
C(1)	9557(1)	9916(1)	9446(1)	9(1)
C(2)	8706(1)	10183(1)	10251(1)	10(1)
C(3)	7735(1)	10127(1)	9387(1)	10(1)
C(4)	7504(1)	9038(2)	7794(2)	14(1)
C(5)	6581(1)	9024(2)	6981(2)	16(1)
C(6)	5892(1)	10111(2)	7785(1)	14(1)
C(7)	6082(1)	11193(2)	9358(2)	15(1)
C(8)	7005(1)	11188(2)	10160(1)	13(1)

Table 8. Bond lengths [Å] and angles [°] for compound **2**.

S(1)-C(2)	1.7693(11)
S(1)-S(2)	2.0817(6)
S(2)-C(1)#1	1.7594(10)
F(1)-C(6)	1.3575(12)
C(1)-C(2)	1.3600(13)
C(1)-C(1)#1	1.4451(18)
C(1)-S(2)#1	1.7594(10)
C(2)-C(3)	1.4664(13)
C(3)-C(8)	1.4046(14)
C(3)-C(4)	1.4046(14)
C(4)-C(5)	1.3912(14)
C(4)-H(4)	0.9500
C(5)-C(6)	1.3827(15)
C(5)-H(5)	0.9500
C(6)-C(7)	1.3814(15)
C(7)-C(8)	1.3889(14)
C(7)-H(7)	0.9500
C(8)-H(8)	0.9500
C(2)-S(1)-S(2)	95.53(3)
C(1)#1-S(2)-S(1)	95.75(3)

C(2)-C(1)-C(1)#1	120.06(11)
C(2)-C(1)-S(2)#1	126.53(7)
C(1)#1-C(1)-S(2)#1	113.41(9)
C(1)-C(2)-C(3)	128.97(9)
C(1)-C(2)-S(1)	115.12(7)
C(3)-C(2)-S(1)	115.91(7)
C(8)-C(3)-C(4)	118.27(9)
C(8)-C(3)-C(2)	119.65(9)
C(4)-C(3)-C(2)	122.07(9)
C(5)-C(4)-C(3)	121.19(10)
C(5)-C(4)-H(4)	119.4
C(3)-C(4)-H(4)	119.4
C(6)-C(5)-C(4)	118.20(10)
C(6)-C(5)-H(5)	120.9
C(4)-C(5)-H(5)	120.9
F(1)-C(6)-C(7)	118.21(9)
F(1)-C(6)-C(5)	118.98(9)
C(7)-C(6)-C(5)	122.81(9)
C(6)-C(7)-C(8)	118.35(10)
C(6)-C(7)-H(7)	120.8
C(8)-C(7)-H(7)	120.8
C(7)-C(8)-C(3)	121.17(9)
C(7)-C(8)-H(8)	119.4
C(3)-C(8)-H(8)	119.4

Symmetry transformations used to generate equivalent atoms:

#1 -x+2,-y+2,-z+2

Table 9. Anisotropic displacement parameters ($Å^2 x\ 10^3$) for compound **2**. The anisotropic displacement factor exponent takes the form: $-2\pi^2[h^2 a^{*2} U^{11} + ... + 2 h k a^* b^* U^{12}]$

	U^{11}	U^{22}	U^{33}	U^{23}	U^{13}	U^{12}
S(1)	10(1)	16(1)	9(1)	-2(1)	1(1)	0(1)
S(2)	10(1)	14(1)	8(1)	-2(1)	0(1)	0(1)
F(1)	9(1)	32(1)	18(1)	-1(1)	-4(1)	-1(1)
C(1)	11(1)	8(1)	7(1)	0(1)	-1(1)	0(1)
C(2)	11(1)	9(1)	9(1)	0(1)	-1(1)	0(1)
C(3)	10(1)	10(1)	10(1)	1(1)	0(1)	0(1)
C(4)	13(1)	15(1)	14(1)	-4(1)	0(1)	0(1)
C(5)	13(1)	19(1)	15(1)	-4(1)	-1(1)	-2(1)
C(6)	9(1)	19(1)	14(1)	2(1)	-2(1)	-2(1)
C(7)	11(1)	18(1)	14(1)	0(1)	1(1)	1(1)
C(8)	12(1)	16(1)	12(1)	-2(1)	0(1)	1(1)

Table 10. Hydrogen coordinates ($x\ 10^4$) and isotropic displacement parameters ($Å^2 x\ 10^3$) for compound **2**.

	x	y	z	U(eq)
H(4)	7987	8299	7263	17
H(5)	6428	8287	5903	19
H(7)	5592	11924	9880	18
H(8)	7146	11914	11250	16

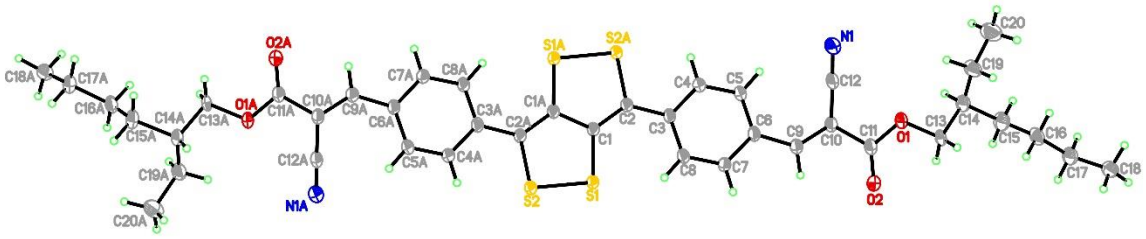

Thermal ellipsoid representation for the crystal structure of compound **12** with atomic labeling scheme. Ellipsoids are drawn at the 50% probability level. The structure contains only half a molecule in the asymmetric unit, the second half of the molecule is generated by a crystallographic inversion center. The figure shows the full molecule; symmetry related atoms are labeled with the letter A in the atom name and are generated by the symmetry operator -x, 2-y, 1-z. Atoms of the minor disorder component are omitted for clarity.

Table 11. Crystal data and structure refinement for compound **12**.

Identification code	X8_13119
Empirical formula	C_{40} H_{44} N_2 O_4 S_4
Formula weight	745.01
Temperature	100(2) K
Wavelength	0.71073 Å
Crystal system	Triclinic
Space group	*P*-1
Unit cell dimensions	*a* = 8.0881(6) Å
	b = 8.2695(6) Å
	c = 15.6391(12) Å
Volume	915.19(12) Å^3
Z	1
Density (calculated)	1.352 Mg/m^3
Absorption coefficient	0.304 mm^{-1}
F(000)	394
Crystal size	0.600 x 0.140 x 0.050 mm^3
Theta range for data collection	1.328 to 30.508°.
Index ranges	-11<=*h*<=11, -11<=*k*<=11, -22<=*l*<=22
Reflections collected	54347
Independent reflections	5549 [R_{int} = 0.0336]
Completeness to theta = 25.242°	99.6 %
Absorption correction	Semi-empirical from equivalents
Max. and min. transmission	0.7462 and 0.6890
Refinement method	Full-matrix least-squares on F^2
Data / restraints / parameters	5549 / 276 / 299

Goodness-of-fit on F^2	1.055
Final R indices [$I>2\sigma(I)$]	$R1$ = 0.0451, $wR2$ = 0.1201
R indices (all data)	$R1$ = 0.0545, $wR2$ = 0.1270
Largest diff. peak and hole	1.056 and -0.361 e.Å^{-3}

Table 12. Atomic coordinates (x 10^4) and equivalent isotropic displacement parameters (Å^{2}x 10^3) for compound **12**. U(eq) is defined as one third of the trace of the orthogonalized U^{ij} tensor.

	x	y	z	U(eq)
S(2)	329(1)	12192(1)	3758(1)	29(1)
S(1)	2464(1)	10147(1)	4284(1)	26(1)
O(2)	12741(2)	1615(2)	6420(1)	32(1)
N(1)	7351(2)	1400(3)	8094(1)	44(1)
C(1)	981(2)	9508(2)	5033(1)	21(1)
C(2)	1523(2)	8196(2)	5630(1)	22(1)
C(3)	3391(2)	7044(2)	5813(1)	22(1)
C(4)	3607(2)	5751(2)	6455(1)	31(1)
C(5)	5342(2)	4593(2)	6647(1)	30(1)
C(6)	6985(2)	4660(2)	6196(1)	23(1)
C(7)	6774(2)	5951(2)	5553(1)	24(1)
C(8)	5033(2)	7122(2)	5367(1)	24(1)
C(9)	8885(2)	3507(2)	6334(1)	24(1)
C(12)	8333(2)	1754(2)	7574(1)	30(1)
C(10)	9526(2)	2231(2)	6922(1)	24(1)
C(11)	11598(2)	1327(2)	6928(1)	26(1)
O(1)	11965(2)	208(2)	7583(1)	32(1)
C(13)	13885(12)	-590(14)	7748(6)	41(2)
C(14)	13741(6)	-1131(6)	8709(3)	32(1)
C(15)	15702(11)	-1717(13)	8974(6)	40(1)
C(16)	17349(11)	-3464(12)	8531(7)	34(1)
C(17)	19177(10)	-3762(14)	8798(6)	36(1)
C(18)	20891(9)	-5539(8)	8470(5)	32(1)
C(19)	13073(5)	-2559(5)	8840(2)	36(1)
C(20)	12718(8)	-3036(8)	9793(3)	50(1)
C(13A)	13841(15)	-525(16)	7789(7)	30(2)
C(14A)	13914(11)	-1793(13)	8544(6)	63(2)
C(15A)	15591(17)	-1890(20)	8988(11)	62(3)
C(16A)	17411(19)	-3340(20)	8529(13)	58(3)
C(17A)	19090(20)	-3720(30)	8940(11)	61(3)
C(18A)	20720(20)	-5380(20)	8506(12)	82(4)
C(19A)	12254(8)	-782(10)	9290(3)	56(2)
C(20A)	11992(12)	-2041(15)	9996(5)	70(2)

Table 13. Bond lengths [Å] and angles [°] for compound **12**.

S(2)-C(2)#1	1.7659(15)

S(2)-S(1)	2.0738(5)
S(1)-C(1)	1.7499(15)
O(2)-C(11)	1.200(2)
N(1)-C(12)	1.148(2)
C(1)-C(2)	1.368(2)
C(1)-C(1)#1	1.443(3)
C(2)-C(3)	1.454(2)
C(2)-S(2)#1	1.7659(15)
C(3)-C(8)	1.404(2)
C(3)-C(4)	1.408(2)
C(4)-C(5)	1.378(2)
C(4)-H(4)	0.9500
C(5)-C(6)	1.403(2)
C(5)-H(5)	0.9500
C(6)-C(7)	1.407(2)
C(6)-C(9)	1.450(2)
C(7)-C(8)	1.381(2)
C(7)-H(7)	0.9500
C(8)-H(8)	0.9500
C(9)-C(10)	1.352(2)
C(9)-H(9)	0.9500
C(12)-C(10)	1.433(2)
C(10)-C(11)	1.498(2)
C(11)-O(1)	1.3309(19)
O(1)-C(13A)	1.455(9)
O(1)-C(13)	1.459(7)
C(13)-C(14)	1.546(7)
C(13)-H(13A)	0.9900
C(13)-H(13B)	0.9900
C(14)-C(19)	1.496(5)
C(14)-C(15)	1.570(6)
C(14)-H(14)	1.0000
C(15)-C(16)	1.531(8)
C(15)-H(15A)	0.9900
C(15)-H(15B)	0.9900
C(16)-C(17)	1.523(7)
C(16)-H(16A)	0.9900
C(16)-H(16B)	0.9900
C(17)-C(18)	1.518(7)
C(17)-H(17A)	0.9900
C(17)-H(17B)	0.9900
C(18)-H(18A)	0.9800
C(18)-H(18B)	0.9800
C(18)-H(18C)	0.9800
C(19)-C(20)	1.530(5)
C(19)-H(19A)	0.9900
C(19)-H(19B)	0.9900
C(20)-H(20A)	0.9800
C(20)-H(20B)	0.9800

C(20)-H(20C)	0.9800
C(13A)-C(14A)	1.533(10)
C(13A)-H(13C)	0.9900
C(13A)-H(13D)	0.9900
C(14A)-C(19A)	1.530(10)
C(14A)-C(15A)	1.609(11)
C(14A)-H(14A)	1.0000
C(15A)-C(16A)	1.482(12)
C(15A)-H(15C)	0.9900
C(15A)-H(15D)	0.9900
C(16A)-C(17A)	1.514(12)
C(16A)-H(16C)	0.9900
C(16A)-H(16D)	0.9900
C(17A)-C(18A)	1.479(13)
C(17A)-H(17C)	0.9900
C(17A)-H(17D)	0.9900
C(18A)-H(18D)	0.9800
C(18A)-H(18E)	0.9800
C(18A)-H(18F)	0.9800
C(19A)-C(20A)	1.533(8)
C(19A)-H(19C)	0.9900
C(19A)-H(19D)	0.9900
C(20A)-H(20D)	0.9800
C(20A)-H(20E)	0.9800
C(20A)-H(20F)	0.9800
C(2)#1-S(2)-S(1)	95.81(5)
C(1)-S(1)-S(2)	95.93(5)
C(2)-C(1)-C(1)#1	120.11(16)
C(2)-C(1)-S(1)	126.44(11)
C(1)#1-C(1)-S(1)	113.43(14)
C(1)-C(2)-C(3)	129.85(14)
C(1)-C(2)-S(2)#1	114.53(11)
C(3)-C(2)-S(2)#1	115.59(11)
C(8)-C(3)-C(4)	117.15(13)
C(8)-C(3)-C(2)	123.30(13)
C(4)-C(3)-C(2)	119.54(14)
C(5)-C(4)-C(3)	122.35(15)
C(5)-C(4)-H(4)	118.8
C(3)-C(4)-H(4)	118.8
C(4)-C(5)-C(6)	120.50(15)
C(4)-C(5)-H(5)	119.7
C(6)-C(5)-H(5)	119.7
C(5)-C(6)-C(7)	117.28(14)
C(5)-C(6)-C(9)	125.56(14)
C(7)-C(6)-C(9)	117.16(14)
C(8)-C(7)-C(6)	122.20(14)
C(8)-C(7)-H(7)	118.9
C(6)-C(7)-H(7)	118.9

C(7)-C(8)-C(3)	120.51(14)
C(7)-C(8)-H(8)	119.7
C(3)-C(8)-H(8)	119.7
C(10)-C(9)-C(6)	131.07(15)
C(10)-C(9)-H(9)	114.5
C(6)-C(9)-H(9)	114.5
N(1)-C(12)-C(10)	178.80(19)
C(9)-C(10)-C(12)	124.04(14)
C(9)-C(10)-C(11)	118.26(14)
C(12)-C(10)-C(11)	117.61(14)
O(2)-C(11)-O(1)	125.64(15)
O(2)-C(11)-C(10)	123.99(14)
O(1)-C(11)-C(10)	110.35(13)
C(11)-O(1)-C(13A)	117.8(4)
C(11)-O(1)-C(13)	116.8(3)
O(1)-C(13)-C(14)	105.8(6)
O(1)-C(13)-H(13A)	110.6
C(14)-C(13)-H(13A)	110.6
O(1)-C(13)-H(13B)	110.6
C(14)-C(13)-H(13B)	110.6
H(13A)-C(13)-H(13B)	108.7
C(19)-C(14)-C(13)	110.8(5)
C(19)-C(14)-C(15)	113.4(5)
C(13)-C(14)-C(15)	108.5(5)
C(19)-C(14)-H(14)	108.0
C(13)-C(14)-H(14)	108.0
C(15)-C(14)-H(14)	108.0
C(16)-C(15)-C(14)	116.8(6)
C(16)-C(15)-H(15A)	108.1
C(14)-C(15)-H(15A)	108.1
C(16)-C(15)-H(15B)	108.1
C(14)-C(15)-H(15B)	108.1
H(15A)-C(15)-H(15B)	107.3
C(17)-C(16)-C(15)	110.4(6)
C(17)-C(16)-H(16A)	109.6
C(15)-C(16)-H(16A)	109.6
C(17)-C(16)-H(16B)	109.6
C(15)-C(16)-H(16B)	109.6
H(16A)-C(16)-H(16B)	108.1
C(18)-C(17)-C(16)	115.8(7)

C(18)-C(17)-H(17A)	108.3
C(16)-C(17)-H(17A)	108.3
C(18)-C(17)-H(17B)	108.3
C(16)-C(17)-H(17B)	108.3
H(17A)-C(17)-H(17B)	107.4
C(17)-C(18)-H(18A)	109.5
C(17)-C(18)-H(18B)	109.5
H(18A)-C(18)-H(18B)	109.5
C(17)-C(18)-H(18C)	109.5
H(18A)-C(18)-H(18C)	109.5
H(18B)-C(18)-H(18C)	109.5
C(14)-C(19)-C(20)	113.8(3)
C(14)-C(19)-H(19A)	108.8
C(20)-C(19)-H(19A)	108.8
C(14)-C(19)-H(19B)	108.8
C(20)-C(19)-H(19B)	108.8
H(19A)-C(19)-H(19B)	107.7
C(19)-C(20)-H(20A)	109.5
C(19)-C(20)-H(20B)	109.5
H(20A)-C(20)-H(20B)	109.5
C(19)-C(20)-H(20C)	109.5
H(20A)-C(20)-H(20C)	109.5
H(20B)-C(20)-H(20C)	109.5
O(1)-C(13A)-C(14A)	107.5(7)
O(1)-C(13A)-H(13C)	110.2
C(14A)-C(13A)-H(13C)	110.2
O(1)-C(13A)-H(13D)	110.2
C(14A)-C(13A)-H(13D)	110.2
H(13C)-C(13A)-H(13D)	108.5

C(19A)-C(14A)-C(13A)	109.3(8)
C(19A)-C(14A)-C(15A)	98.6(8)
C(13A)-C(14A)-C(15A)	104.5(9)
C(19A)-C(14A)-H(14A)	114.3
C(13A)-C(14A)-H(14A)	114.3
C(15A)-C(14A)-H(14A)	114.3
C(16A)-C(15A)-C(14A)	109.1(11)
C(16A)-C(15A)-H(15C)	109.9
C(14A)-C(15A)-H(15C)	109.9
C(16A)-C(15A)-H(15D)	109.9
C(14A)-C(15A)-H(15D)	109.9
H(15C)-C(15A)-H(15D)	108.3
C(15A)-C(16A)-C(17A)	114.9(12)
C(15A)-C(16A)-H(16C)	108.5
C(17A)-C(16A)-H(16C)	108.5
C(15A)-C(16A)-H(16D)	108.5
C(17A)-C(16A)-H(16D)	108.5
H(16C)-C(16A)-H(16D)	107.5
C(18A)-C(17A)-C(16A)	108.7(13)
C(18A)-C(17A)-H(17C)	109.9
C(16A)-C(17A)-H(17C)	109.9
C(18A)-C(17A)-H(17D)	109.9
C(16A)-C(17A)-H(17D)	109.9
H(17C)-C(17A)-H(17D)	108.3
C(17A)-C(18A)-H(18D)	109.5

C(17A)-C(18A)-H(18E)	109.5
H(18D)-C(18A)-H(18E)	109.5
C(17A)-C(18A)-H(18F)	109.5
H(18D)-C(18A)-H(18F)	109.5
H(18E)-C(18A)-H(18F)	109.5
C(14A)-C(19A)-C(20A)	112.7(6)
C(14A)-C(19A)-H(19C)	109.0
C(20A)-C(19A)-H(19C)	109.0
C(14A)-C(19A)-H(19D)	109.0
C(20A)-C(19A)-H(19D)	109.0
H(19C)-C(19A)-H(19D)	107.8
C(19A)-C(20A)-H(20D)	109.5
C(19A)-C(20A)-H(20E)	109.5
H(20D)-C(20A)-H(20E)	109.5
C(19A)-C(20A)-H(20F)	109.5
H(20D)-C(20A)-H(20F)	109.5
H(20E)-C(20A)-H(20F)	109.5

Symmetry transformations used to generate equivalent atoms:

#1 -x,-y+2,-z+1

Table 14. Anisotropic displacement parameters ($Å^2 x\ 10^3$) for compound **12**. The anisotropic displacement factor exponent takes the form: $-2\pi^2[h^2 a^{*2} U^{11} + ... + 2 h k a^* b^* U^{12}]$

	U^{11}	U^{22}	U^{33}	U^{23}	U^{13}	U^{12}
S(2)	20(1)	28(1)	38(1)	18(1)	-10(1)	-11(1)
S(1)	18(1)	25(1)	35(1)	14(1)	-9(1)	-10(1)
O(2)	22(1)	36(1)	34(1)	13(1)	-8(1)	-10(1)
N(1)	34(1)	55(1)	49(1)	28(1)	-17(1)	-22(1)
C(1)	19(1)	17(1)	27(1)	6(1)	-8(1)	-9(1)
C(2)	19(1)	19(1)	28(1)	7(1)	-7(1)	-9(1)
C(3)	20(1)	18(1)	29(1)	6(1)	-9(1)	-8(1)
C(4)	21(1)	32(1)	38(1)	17(1)	-9(1)	-11(1)
C(5)	24(1)	29(1)	36(1)	17(1)	-11(1)	-11(1)
C(6)	21(1)	20(1)	27(1)	5(1)	-9(1)	-7(1)
C(7)	20(1)	23(1)	31(1)	8(1)	-8(1)	-10(1)
C(8)	22(1)	20(1)	31(1)	10(1)	-10(1)	-9(1)
C(9)	22(1)	22(1)	27(1)	5(1)	-8(1)	-8(1)
C(12)	25(1)	32(1)	35(1)	14(1)	-15(1)	-12(1)
C(10)	21(1)	23(1)	28(1)	6(1)	-10(1)	-8(1)
C(11)	24(1)	25(1)	29(1)	7(1)	-10(1)	-9(1)
O(1)	23(1)	37(1)	37(1)	18(1)	-15(1)	-12(1)
C(13)	23(3)	52(4)	43(3)	33(3)	-18(3)	-12(3)
C(14)	27(2)	41(2)	32(2)	13(1)	-17(1)	-16(2)
C(15)	34(2)	53(3)	42(3)	16(2)	-23(2)	-22(2)
C(16)	35(2)	38(2)	39(3)	19(2)	-24(2)	-22(2)
C(17)	30(2)	42(3)	37(2)	13(2)	-17(2)	-17(2)
C(18)	34(2)	32(2)	33(3)	7(2)	-9(2)	-17(2)
C(19)	40(2)	45(2)	37(2)	17(1)	-21(1)	-28(2)
C(20)	56(3)	66(3)	38(2)	19(2)	-14(2)	-35(2)
C(13A)	22(4)	31(4)	39(3)	5(3)	-11(3)	-13(3)
C(14A)	34(3)	79(5)	65(4)	46(3)	-19(2)	-15(3)
C(15A)	47(3)	92(6)	48(5)	35(4)	-11(3)	-34(4)
C(16A)	48(3)	82(6)	55(6)	31(5)	-21(4)	-37(4)
C(17A)	64(4)	57(5)	77(7)	9(5)	-46(4)	-27(4)
C(18A)	71(6)	100(8)	71(8)	7(6)	-26(6)	-30(5)
C(19A)	53(3)	89(4)	38(2)	23(2)	-22(2)	-39(3)
C(20A)	64(5)	120(7)	40(3)	35(4)	-20(3)	-54(5)

Table 15. Hydrogen coordinates ($x\ 10^4$) and isotropic displacement parameters ($Å^2 x\ 10^3$) for compound **12**.

	x	y	z	U(eq)
H(4)	2517	5673	6768	37
H(5)	5427	3743	7087	36
H(7)	7866	6021	5238	29
H(8)	4946	7985	4933	29

H(9)	9844	3679	5944	28
H(13A)	14401	300	7656	49
H(13B)	14718	-1668	7353	49
H(14)	12788	-33	9079	38
H(15A)	16055	-716	8849	48
H(15B)	15545	-1858	9613	48
H(16A)	17086	-4507	8699	40
H(16B)	17484	-3384	7890	40
H(17A)	19465	-2754	8585	43
H(17B)	18966	-3697	9443	43
H(18A)	21998	-5578	8655	48
H(18B)	21114	-5632	7831	48
H(18C)	20666	-6554	8711	48
H(19A)	14028	-3670	8494	43
H(19B)	11889	-2135	8614	43
H(20A)	12271	-3964	9832	75
H(20B)	11760	-1948	10141	75
H(20C)	13894	-3501	10017	75
H(13C)	14090	469	7962	36
H(13D)	14809	-1203	7274	36
H(14A)	14052	-3002	8368	76
H(15C)	15629	-710	8951	75
H(15D)	15366	-2158	9612	75
H(16C)	17664	-2987	7922	70
H(16D)	17285	-4468	8505	70
H(17C)	19397	-2682	8870	73
H(17D)	18801	-3898	9571	73
H(18D)	21808	-5670	8783	123
H(18E)	21046	-5169	7888	123
H(18F)	20397	-6388	8559	123
H(19C)	11083	-158	9051	67
H(19D)	12462	155	9558	67
H(20D)	10944	-1323	10467	104
H(20E)	13152	-2677	10230	104
H(20F)	11711	-2929	9742	104

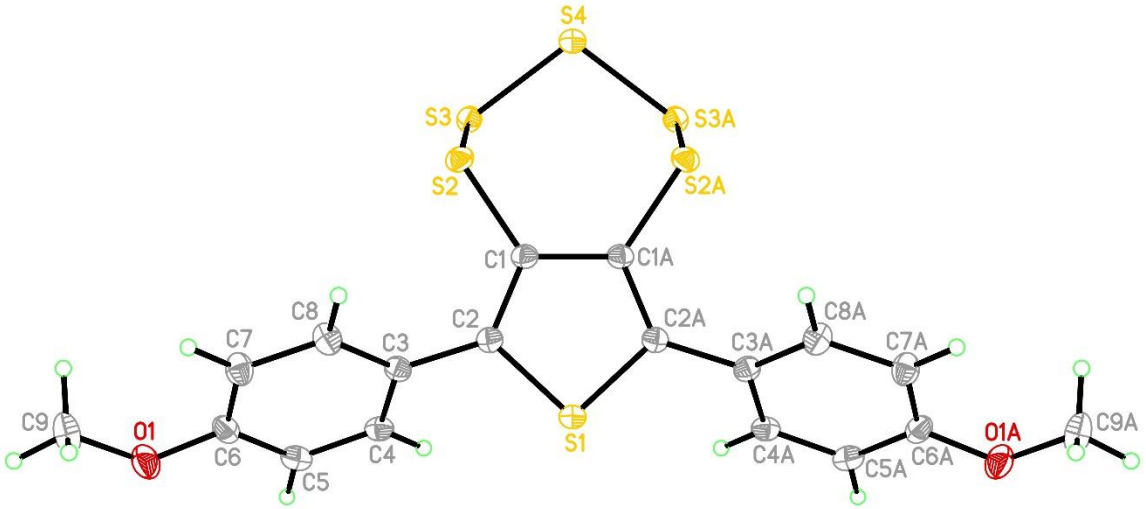

Thermal ellipsoid representation for the crystal structure of compound **17** with atomic labeling scheme. Ellipsoids are drawn at the 50% probability level. The structure contains only half a molecule in the asymmetric unit, the second half of the molecule is generated by a crystallographic mirror plane. The figure shows the full molecule; symmetry related atoms are labeled with the letter A in the atom name and are generated by the symmetry operator x, 1.5-y, z.

Table 16. Crystal data and structure refinement for compound **17**.

Identification code	X8_13046
Empirical formula	$C_{18}\ H_{14}\ O_2\ S_6$
Formula weight	454.65
Temperature	100(2) K
Wavelength	0.71073 Å
Crystal system	Orthorhombic
Space group	*Pnma*
Unit cell dimensions	a = 7.6474(10) Å
	b = 25.491(4) Å
	c = 9.7609(13) Å
Volume	1902.8(4) Å^3
Z	4
Density (calculated)	1.587 Mg/m^3
Absorption coefficient	0.730 mm^{-1}
F(000)	936
Crystal size	0.27 x 0.17 x 0.14 mm^3
Theta range for data collection	1.60 to 31.40°.
Index ranges	-11<=h<=11, -37<=k<=37, -14<=l<=13
Reflections collected	83028
Independent reflections	3200 [R_{int} = 0.0278]

Completeness to theta = 31.40°	99.9 %
Absorption correction	Semi-empirical from equivalents
Max. and min. transmission	0.9047 and 0.8273
Refinement method	Full-matrix least-squares on F^2
Data / restraints / parameters	3200 / 0 / 122
Goodness-of-fit on F^2	1.274
Final R indices [$I>2\sigma(I)$]	$R1$ = 0.0344, $wR2$ = 0.0899
R indices (all data)	$R1$ = 0.0355, $wR2$ = 0.0905
Largest diff. peak and hole	0.518 and -0.403 e.Å^{-3}

Table 17. Atomic coordinates (x 10^4) and equivalent isotropic displacement parameters (Å^{2}x 10^3) for compound **17**. U(eq) is defined as one third of the trace of the orthogonalized U^{ij} tensor.

	x	y	z	U(eq)
S(1)	6804(1)	7500	6008(1)	16(1)
S(2)	1742(1)	6833(1)	5390(1)	17(1)
S(3)	1472(1)	6855(1)	3285(1)	17(1)
S(4)	-80(1)	7500	2881(1)	18(1)
C(1)	3633(2)	7216(1)	5646(2)	15(1)
C(2)	5280(2)	7007(1)	5819(2)	15(1)
C(3)	5870(2)	6457(1)	5848(2)	16(1)
C(4)	7420(2)	6315(1)	5167(2)	17(1)
C(5)	8032(2)	5804(1)	5211(2)	19(1)
C(6)	7100(2)	5421(1)	5925(2)	19(1)
C(7)	5570(2)	5555(1)	6617(2)	21(1)
C(8)	4973(2)	6072(1)	6577(2)	20(1)
O(1)	7797(2)	4928(1)	5898(2)	26(1)
C(9)	6884(3)	4528(1)	6626(2)	33(1)

Table 18. Bond lengths [Å] and angles [°] for compound **17**.

S(1)-C(2)#1	1.7239(16)
S(1)-C(2)	1.7240(16)
S(2)-C(1)	1.7631(16)
S(2)-S(3)	2.0660(6)
S(3)-S(4)	2.0648(6)
S(4)-S(3)#1	2.0647(6)
C(1)-C(2)	1.378(2)
C(1)-C(1)#1	1.447(3)
C(2)-C(3)	1.472(2)
C(3)-C(8)	1.394(2)
C(3)-C(4)	1.406(2)
C(4)-C(5)	1.386(2)
C(4)-H(4)	0.9500
C(5)-C(6)	1.395(2)
C(5)-H(5)	0.9500

C(6)-O(1)	1.366(2)
C(6)-C(7)	1.394(2)
C(7)-C(8)	1.396(2)
C(7)-H(7)	0.9500
C(8)-H(8)	0.9500
O(1)-C(9)	1.425(3)
C(9)-H(9A)	0.9800
C(9)-H(9B)	0.9800
C(9)-H(9C)	0.9800
C(2)#1-S(1)-C(2)	93.59(11)
C(1)-S(2)-S(3)	101.97(5)
S(4)-S(3)-S(2)	105.63(3)
S(3)#1-S(4)-S(3)	105.45(3)
C(2)-C(1)-C(1)#1	112.77(9)
C(2)-C(1)-S(2)	123.56(12)
C(1)#1-C(1)-S(2)	123.64(5)
C(1)-C(2)-C(3)	130.61(14)
C(1)-C(2)-S(1)	110.43(12)
C(3)-C(2)-S(1)	118.96(12)
C(8)-C(3)-C(4)	118.35(15)
C(8)-C(3)-C(2)	121.93(14)
C(4)-C(3)-C(2)	119.68(14)
C(5)-C(4)-C(3)	120.86(15)
C(5)-C(4)-H(4)	119.6
C(3)-C(4)-H(4)	119.6
C(4)-C(5)-C(6)	120.06(15)
C(4)-C(5)-H(5)	120.0
C(6)-C(5)-H(5)	120.0
O(1)-C(6)-C(7)	124.25(16)
O(1)-C(6)-C(5)	115.78(16)
C(7)-C(6)-C(5)	119.97(15)
C(6)-C(7)-C(8)	119.53(16)
C(6)-C(7)-H(7)	120.2
C(8)-C(7)-H(7)	120.2
C(3)-C(8)-C(7)	121.23(16)
C(3)-C(8)-H(8)	119.4
C(7)-C(8)-H(8)	119.4
C(6)-O(1)-C(9)	117.23(15)
O(1)-C(9)-H(9A)	109.5
O(1)-C(9)-H(9B)	109.5
H(9A)-C(9)-H(9B)	109.5
O(1)-C(9)-H(9C)	109.5
H(9A)-C(9)-H(9C)	109.5
H(9B)-C(9)-H(9C)	109.5

Symmetry transformations used to generate equivalent atoms:

#1 x,-y+3/2,z

Table 19. Anisotropic displacement parameters ($Å^2 x\ 10^3$) for compound **17**. The anisotropic displacement factor exponent takes the form: $-2\pi^2[h^2 a^{*2} U^{11} + ... + 2 h k a^* b^* U^{12}]$

	U^{11}	U^{22}	U^{33}	U^{23}	U^{13}	U^{12}
S(1)	14(1)	17(1)	18(1)	0	-2(1)	0
S(2)	15(1)	18(1)	18(1)	3(1)	0(1)	-3(1)
S(3)	17(1)	16(1)	18(1)	-1(1)	0(1)	-1(1)
S(4)	15(1)	19(1)	18(1)	0	-2(1)	0
C(1)	13(1)	17(1)	15(1)	1(1)	0(1)	0(1)
C(2)	16(1)	17(1)	14(1)	0(1)	0(1)	0(1)
C(3)	16(1)	18(1)	13(1)	1(1)	-1(1)	1(1)
C(4)	15(1)	22(1)	15(1)	2(1)	-1(1)	-1(1)
C(5)	16(1)	24(1)	17(1)	-2(1)	-1(1)	3(1)
C(6)	21(1)	18(1)	18(1)	-1(1)	-4(1)	4(1)
C(7)	24(1)	19(1)	19(1)	4(1)	3(1)	1(1)
C(8)	21(1)	20(1)	18(1)	3(1)	5(1)	3(1)
O(1)	28(1)	18(1)	31(1)	-1(1)	-1(1)	6(1)
C(9)	42(1)	18(1)	37(1)	5(1)	0(1)	6(1)

Table 20. Hydrogen coordinates ($x\ 10^4$) and isotropic displacement parameters ($Å^2 x\ 10^3$) for compound **17**.

	x	y	z	U(eq)
H(4)	8055	6573	4670	21
H(5)	9088	5714	4755	23
H(7)	4937	5296	7112	25
H(8)	3936	6164	7057	24
H(9A)	6833	4619	7600	49
H(9B)	7497	4193	6515	49
H(9C)	5694	4496	6263	49

2.5.7. References

(110) Nie, X.; Wang, G. Synthesis and Self-Assembling Properties of Diacetylene Containing. 1–38.

(111) Neubert, M. E.; Fisch, M. R.; Keast, S. S.; Kim, J. M.; Lohman, M. C.; Murray, R. S.; Miller, K. J.; Shenoy, R. A.; Smith, M. J.; Stayshich, R. M.; et al. The Effect of Terminal Chain Modifications on the Mesomorphic Properties of 4,4′-Disubstituted Diphenyldiacetylenes. *Liq. Cryst.* **2004**, *31* (7), 941–963.

(112) Osowska, K.; Lis, T.; Szafert, S. Protection/Deprotection-Free Syntheses and Structural Analysis of (Keto-Aryl)diynes. *European J. Org. Chem.* **2008**, *2008* (27), 4598–4606.

(113) Cox, J. R.; Ferris, L. A.; Thalladi, V. R. Selective Growth of a Stable Drug Polymorph by Suppressing the Nucleation of Corresponding Metastable Polymorphs. *Angew. Chemie Int. Ed.* **2007**, *46* (23), 4333–4336.

(114) Zhang, S.; Liu, X.; Wang, T. An Efficient Copper-Catalyzed Homocoupling of Terminal Alkynes to Give Symmetrical 1,4-Disubstituted 1,3-Diynes. *Adv. Synth. Catal.* **2011**, *353* (9), 1463–1466.

(115) Yin, W.; He, C.; Chen, M.; Zhang, H.; Lei, A. Nickel-Catalyzed Oxidative Coupling Reactions of Two Different Terminal Alkynes Using O2 as the Oxidant at Room Temperature: Facile Syntheses of Unsymmetric 1,3-Diynes. *Org. Lett.* **2009**, *11* (3), 709–712.

(116) Arakawa, Y.; Nakajima, S.; Ishige, R.; Uchimura, M.; Kang, S.; Konishi, G.; Watanabe, J. Synthesis of Diphenyl-Diacetylene-Based Nematic Liquid Crystals and Their High Birefringence Properties. *J. Mater. Chem.* **2012**, *22* (17), 8394.

(117) Spitler, E. L.; Koo, B. T.; Novotney, J. L.; Colson, J. W.; Uribe-Romo, F. J.; Gutierrez, G. D.; Clancy, P.; Dichtel, W. R. A 2D Covalent Organic Framework with 4.7-Nm Pores and

Insight into Its Interlayer Stacking. *J. Am. Chem. Soc.* **2011**, *133* (48), 19416–19421.

(118) Sheldrick, G. M. Phase Annealing in SHELX-90: Direct Methods for Larger Structures. *Acta Crystallogr. Sect. A Found. Crystallogr.* **1990**, *46* (6), 467–473.

(119) Sheldrick, G. M. A Short History of SHELX. *Acta Crystallogr. Sect. A Found. Crystallogr.* **2008**, *64* (1), 112–122.

(120) Müller, P. Practical Suggestions for Better Crystal Structures. *Crystallogr. Rev.* **2009**, *15* (1), 57–83.